NASA CONTRACTOR REPORT

NASA CR-2705

NASA CR-2705

CALCULATION OF THE LONGITUDINAL AERODYNAMIC CHARACTERISTICS OF WING-FLAP CONFIGURATIONS WITH EXTERNALLY BLOWN FLAPS
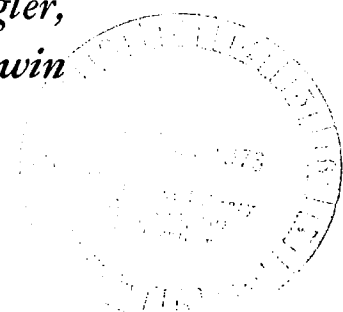
*Michael R. Mendenhall, Selden B. Spangler,
Jack N. Nielsen, and Frederick K. Goodwin*

Prepared by
NIELSEN ENGINEERING & RESEARCH, INC.
Mountain View, Calif. 94043
for Langley Research Center

NATIONAL AERONAUTICS AND SPACE ADMINISTRATION • WASHINGTON, D. C.   SEPTEMBER 1976

0061432

1. Report No. NASA CR-2705	2. Government Accession No.	3. Recipient's Catalog No.
4. Title and Subtitle Calculation of the Longitudinal Aerodynamic Characteristics of Wing-Flap Configurations with Externally Blown Flaps		5. Report Date September 1976
		6. Performing Organization Code
7. Author(s) Michael R. Mendenhall, Seldon B. Spangler, Jack N. Nielsen, and Frederick K. Goodwin		8. Performing Organization Report No.
		10. Work Unit No.
9. Performing Organization Name and Address Nielsen Engineering and Research, Inc 510 Clyde Avenue Mountain View, CA 94943		11. Contract or Grant No. NAS1-13158
		13. Type of Report and Period Covered Contractor Report
12. Sponsoring Agency Name and Address National Aeronautics and Space Administration Washington, DC 20546		14. Sponsoring Agency Code

15. Supplementary Notes Langley Technical Monitor Robert C. Goetz Final Report

16. Abstract A theoretical investigation has been carried out to extend and improve an existing method for predicting the longitudinal aerodynamic characteristics of wing-flap configurations with externally blown flaps (EBF). Two potential flow models were incorporated into the prediction method: a wing and flap lifting-surface model and a turbofan engine wake model. The wing-flap model uses a vortex-lattice approach to represent the wing and flaps. The wing may have an arbitrary planform and camber and twist. The flap system may be made of multiple elements of arbitrary size which can have large deflection angles. The jet wake model consists of a series of closely spaced vortex rings normal to a centerline which may have vertical and lateral curvature to conform to the local flow field beneath the wing and flaps. The vortex ring wake model may be circular or elliptic in cross section and the wake can be specified such that the mass, momentum, and spreading rates are similar to the actual turbulent wake. Measured turbulent jet spreading rates may be used to specify the jet if analytical spreading rates are not available. An iteration procedure is provided to locate the engine wake centerline(s).

Comparisons of measured and predicted pressure distributions, span-load distributions on each lifting surface, and total lift and pitching moment coefficients on swept and unswept EBF configurations are included in this report. A wide range of thrust coefficients and flap deflection angles is considered at angles of attack up to the onset of stall. Results indicate that overall lift and pitching-moment coefficients are predicted reasonably well over the entire range. The predicted detailed load distributions are qualitatively correct and show the peaked loads at the jet impingement points, but the widths and heights of the load peaks are not consistently predicted.

17. Key Words (Suggested by Author(s)) Externally Blown Flaps STOL	18. Distribution Statement UNCLASSIFIED - UNLIMITED Subject Category 02	
19. Security Classif. (of this report) UNCLASSIFIED	20. Security Classif. (of this page) UNCLASSIFIED	21. No. of Pages 141	22. Price* $5.75

*For sale by the National Technical Information Service, Springfield, Virginia 22161

TABLE OF CONTENTS

TABLE OF CONTENTS

CALCULATION OF THE LONGITUDINAL AERODYNAMIC

CHARACTERISTICS OF WING-FLAP CONFIGURATIONS

WITH EXTERNALLY BLOWN FLAPS

by Michael R. Mendenhall, Selden B. Spangler,
Jack N. Nielsen, and Frederick K. Goodwin
Nielsen Engineering & Research, Inc.

SUMMARY

A theoretical investigation has been carried out to extend and improve an existing method for predicting the longitudinal aerodynamic characteristics of wing-flap configurations with externally blown flaps (EBF). Two potential flow models were incorporated into the prediction method: a wing and flap lifting-surface model and a turbofan engine wake model. The wing-flap model uses a vortex-lattice approach to represent the wing and flaps. The wing may have an arbitrary planform and camber and twist. The flap system may be made up of multiple elements of arbitrary size which can have large deflection angles. The jet wake model consists of a series of closely spaced vortex rings normal to a centerline which may have vertical and lateral curvature to conform to the local flow field beneath the wing and flaps. The vortex ring wake model may be circular or elliptic in cross section and the wake can be specified such that the mass, momentum, and spreading rates are similar to the actual turbulent wake. Measured turbulent jet spreading rates may be used to specify the jet if analytical spreading rates are not available. An iteration procedure is provided to locate the engine wake centerline(s).

Comparisons of measured and predicted pressure distributions, span-load distributions on each lifting surface, and total lift and pitching-moment coefficients on swept and unswept EBF configurations are included in this report. A wide range of thrust coefficients and flap deflection angles is considered at angles of attack up to the onset of stall. Results indicate that overall lift and pitching-moment coefficients are predicted reasonably well over the entire range. The predicted detailed load distributions are qualitatively correct and show the peaked loads at the jet impingement points, but the widths and heights of the load peaks are not consistently predicted.

INTRODUCTION

The short take-off and landing requirement for STOL aircraft necessitates a means of achieving very high lift coefficients on aircraft in take-off or landing configuration with little sacrifice in cruise performance. The externally blown jet-augmented flap provides such a means. The jet efflux from engines mounted beneath the wing is allowed to impinge directly on the slotted flap system, thus producing a large amount of additional lift through engine wake deflection and mutual interference effects.

Several analytical methods for predicting the longitudinal aerodynamic characteristics of EBF configurations have been developed. Some of these methods require extensive use of empirically determined information (ref. 1), and others require little empirical data as input (refs. 2 and 3). Reference 3 involves the use of two potential flow models: a wing-flap, lifting-surface model and a jet wake model. The wing-flap, lifting-surface model is a nonplanar, nonlinear, vortex-lattice scheme. The jet wake model consists of a series of vortex ring singularities representing a turbulent jet, the boundary of which may be specified analytically or with the use of empirical data. These two flow models are combined in such a fashion that the tangency boundary condition is satisfied on the wing and flap surfaces. Jet wake deflection is accommodated through calculation of the flow field beneath the wing and estimates of the resulting wake deflection by the user of the method.

The purpose of the work described herein is to make certain improvements and extensions to the original prediction method. These fall into three categories. In the first, the vortex-lattice model of the wing-flap is made more versatile and accurate for modeling multiple flap arrangements. In the second, the model of the jet wake is extended to include elliptical as well as circular cross sections in order to more accurately represent the wake characteristics near the impingement area on the flaps. In the third, the method of determining the wake centerline position is refined and automated within the computer program.

This report presents the technical approach to the problem, the development of the flow models, and comparisons with data. The discussion assumes some familiarity with the earlier work of reference 3. A user's manual for the resulting computer program is contained in reference 4.

SYMBOLS

a	semi-major axis of ellipse
a_1, b_1	imaginary and real parts, respectively, of complex roots of quadratic equation, Appendix B
A_j	initial area of jet wake
b	semi-minor axis of ellipse
c	chord of area element on wing or flap; wing chord; or distance from origin of ellipse and focus, figure 6(b)
cd u, cn u, dn u, sn u, tn u	Jacobian elliptic functions, Appendix B
c_n	section normal-force coefficient
c_A	axial-force coefficient on an area element on wing, axial force/qS; positive as shown in figure 4(a)
c_{A_f}	axial-force coefficient on an area element on a flap, axial force/qS; positive as shown in figure 4(b)
c_D	drag coefficient, drag/qS; positive aft
c_L	lift coefficient, lift/qS
c_m	pitching-moment coefficient, moment/qS; positive in direction of angle of attack
c_N	normal-force coefficient on an area element on wing, normal force/qS; positive as shown in figure 4(a)
c_{N_f}	normal-force coefficient on an area element on a flap, normal force/qS; positive as shown in figure 4(b)
c_T	thrust coefficient of a single jet, thrust/qS; positive in forward direction
c_{Y_f}	side-force coefficient on an area element on a flap, side force/qS; positive as shown in figure 4(b)
c_μ	total thrust coefficient for a configuration with multiple jets, thrust/qS
d	diameter of circular cross-section jet wake
$E(k)$	elliptic integral of the first kind with argument k
f_u, f_v, f_w	influence coefficients for a vortex filament, equations (16) and (20); positive as shown in figure 3

$F(k)$	elliptic integral of the second kind with argument k
F_N	influence function for velocity normal to camber surface, equation (3)
F_u, F_v, F_w	influence coefficients for a wing horseshoe vortex, positive as shown in figure 2(a)
$F_{u_f}, F_{v_f}, F_{w_f}$	influence coefficients for a flap horseshoe vortex, positive as shown in figure 2(b)
$\vec{i}, \vec{j}, \vec{k}$	unit vectors in x, y, z directions, respectively, see figure 6
J_n	integrals defined by equations (A-24) and (B-1)
k	argument of elliptic integrals, see equations (32) and (B-10)
k'	$1 - k^2$
M	total number of vortex area elements on wing surface
$NF(j)$	number of vortex area elements on flap j
$NFLAPS$	total number of flap surfaces
P	perimeter of a vortex ring, equation (31)
q	free-stream dynamic pressure
r	radial distance from a circular jet centerline to a field point
R	radial distance from a point on a vortex ring to a field point, equation (A-15); or local radius of a circular jet
s	semispan of a horseshoe vortex measured in wing or flap chordal plane; or distance measured along jet centerline, figure 7
S	wing area
t	transformed coordinate η, equation (A-16)
u, v, w	velocities induced at the midpoint of the bound leg of a wing horseshoe vortex in the X, Y, Z directions
u_f, v_f, w_f	velocities induced at the midpoint of the bound leg of a flap horseshoe vortex in the X_f, Y_f, Z_f directions
u_i, v_i, w_i	velocities in the X, Y, Z directions induced by the jet wake
u_n, v_n, w_n	total induced velocity field at a point on the jet wake centerline, equation (34)

4

v_1	y-direction velocity induced at the three-fourth chord location of the side edge of a wing area element, see equation (24)
v_{f_1}, w_{f_1}	velocities induced at the three-fourth chord location of the side edge of a flap area element in the Y_f and Z_f directions, respectively
v_x, v_y, v_z	vortex ring induced velocities, equations (A-25), (A-26), and (A-27)
V	free-stream velocity
V_j	initial jet wake velocity, equation (29)
x, y, z	coordinate system fixed at center of ellipse, figure 6; or coordinate system associated with a lifting surface containing a horseshoe vortex
x_j, y_j, z_j	jet coordinate system fixed at the center of the jet inlet, figure 7
X, Y, Z	wing coordinate system, see figure 2(a), with origin at wing root-chord leading edge
X_f, Y_f, Z_f	flap coordinate system, see figure 2(b), with origin at inboard side-edge leading edge of flap
α	wing root chord angle of attack relative to free-stream direction
α_ℓ	angle between tangent to mean camber surface of the wing and the X direction
γ	jet wake vortex cylinder strength
Γ	vortex ring strength, or horseshoe vortex strength
δ_ℓ	angle between tangent to mean camber surface of a flap and the X_f direction
δ_{xz}	streamwise flap deflection angle measured in a plane parallel to the X-Z plane, positive downwards
ΔC_p	pressure difference across a lifting surface
θ	flow angle of jet centerline measured in x_j, z_j plane, equation (35)
$\overline{\theta}$	average flow angle of jet centerline, equation (37)
ξ, η	elliptic coordinate, Appendix A
ρ	density
σ	flow angle of jet centerline measured in x_j, y_j plane, equation (36)

$\bar{\sigma}$ average lateral flow angle of centerline, equation (40)

τ constant defined in equation (B-39)

ϕ wing dihedral angle, positive as shown in figure 2(a)

ϕ_f flap dihedral angle, positive as shown in figure 2(b)

ψ sweep angle of the bound leg of a wing horseshoe vortex measured in the wing chordal plane, positive swept back

ψ_f sweep angle of the bound leg of a flap horseshoe vortex measured in the flow chordal plane, positive swept back

Subscripts

f   flap

j   jet wake

left   left leg of horseshoe vortex

o   initial conditions

right   right leg of horseshoe vortex

S   slat

W or WF   wing-flap

α free stream

I,II,III,IV   denote four quadrants of elliptic vortex ring, figure 6(a)

1/2   denotes position at which jet axial velocity is half the maximum velocity on the centerline

Superscripts

$\rightarrow$ vector

'   primes indicate local coordinate system

6

ANALYSIS

The work described in this report is basically an extension of that reported in reference 3. Certain improvements were made in both the lifting-surface model and the jet model, and both models were then combined to form an iterative approach to the calculation of the aerodynamic characteristics of EBF configurations. In this section, each flow model and its modifications are discussed individually, and then the total EBF interference procedure is described.

Wing-Flap Vortex-Lattice Model

General description.- The vortex-lattice lifting-surface model used in the present investigation is an extension of that used in references 3 and 5. In reference 3, the configuration treated consisted of a wing with a single trailing-edge flap with a uniform deflection angle. Multiple flaps were handled by specifying a camber distribution over some mean flap surface. In reference 5, multiple spanwise flap segments were considered, but separate loading distributions on individual flap elements were not available. The vortex-lattice model in both references 3 and 5 allowed the trailing vortex legs to extend aft to infinity in the plane of the originating surface; that is, the wing chordal plane or the flap chordal plane.

Typical externally blown flap (EBF) and upper-surface-blowing (USB) configurations have multiple spanwise flap segments, each of which may be made up of multiple flap elements. In the present investigation, the method and associated computer program have been modified so that each flap segment is defined as a separate lifting surface for the purpose of computing forces and moments. The trailing vorticity is deflected so that it lies on each surface aft of its originating surface and then extends to infinity in the plane of the last surface as illustrated in figure 1.

The wing and flap configuration parameters included in the method are listed below.

Wing Panels

Leading-edge shape: May have up to 30 breaks in sweep.

Trailing-edge shape: Same as for leading edge.

Taper: Determined from leading-edge and trailing-edge shapes.

Tip chord: Parallel to root chord.

Dihedral: Arbitrary but constant over the semispan.

Mean camber surface: May have both twist and camber.

Thickness: Neglected.

Flap Panels

Number: Up to 10 individual flap segments; maximum of 3 at any spanwise region.

Location: First flap in any spanwise region is at or near wing trailing edge; gaps are permitted between wing and first flap and succeeding flaps.

Leading-edge shape: Straight line which may be swept.

Trailing-edge shape: Same as for leading edge.

Taper: Linear.

Root chord: In plane parallel to vertical plane containing wing root chord.

Tip chord: Parallel to root chord.

Span: Full or partial span.

Deflection: Each flap may have a different deflection angle.

Mean camber surface: Each flap may have both twist and camber.

Thickness: Neglected.

The method is restricted to angle of attack; that is, yaw effects are not included. Compressibility effects are not included since large flap deflections are only used at low speeds. Angle of attack, flap deflection angle, dihedral angle, and twist and camber angle are accounted for in the boundary condition by trigonometric functions since some of these angles may be large.

The vortex-lattice arrangement and the coordinate system for a swept wing with trailing-edge flaps deflected are shown in figure 1. The wing and flaps are divided into trapezoidal area elements. The flap side edges must lie along chordwise edges of the area elements, and the span-wise distribution of area elements on the flaps must be the same as on the wing section ahead of the flap.

8

A horseshoe vortex is placed in each area element such that the bound leg lies along the quarter chord of the area element and the trailing legs lie along the side edges of the element in the plane of the element. The trailing legs trail back in the plane of the area element until the leading edge of the next surface is encountered. They are then deflected so that they lie in the plane of that surface. This deflection is continued through the last surface. The trailing legs are then extended aft to infinity in the plane of the last surface.

The flow tangency boundary condition is applied at the midspan of the three-quarter chord line of each area element. The wing and flap boundary conditions will now be determined.

Wing boundary condition.- The wing boundary condition is that the velocity normal to the mean camber surface at a wing control point be zero. This can be written

$$\frac{1}{V}\left(\sum_{n=1}^{M} V_{\Gamma_w,\nu,n} + \sum_{j=1}^{NFLAPS} \sum_{n=1}^{NF(j)} V_{\Gamma_f,\nu,n} + V_{N,\nu} + V_{i,\nu}\right) = 0 \qquad (1)$$

$$\nu = 1, 2, \ldots M$$

The first term is the sum of the normal velocities induced at the νth control point by the M wing vortices. The second term is the sum of the normal velocities induced by all of the flap vortices. There are NFLAPS flaps and NF(j) vortices on the jth flap. The component of the free-stream velocity normal to the camber surface is the third term, $V_{N,\nu}$. The last term contains externally induced velocities such as those due to an engine wake. The derivation of the four terms will now be presented.

Figure 2(a) shows coordinate systems associated with a wing inclined at dihedral angle, ϕ. The X,Y,Z system is the basic wing system shown in figure 1. The quantities F_u, F_v, F_w are influence functions, dimensionless velocities per unit vortex strength, with positive directions as shown. The X',Y',Z' system is obtained by rotating the X,Y,Z system through the wing dihedral angle, ϕ. The quantities F'_u, F'_v, F'_w are influence functions in the primed coordinate system and are

$$F_u' = F_u$$

$$F_v' = F_v \cos \phi + F_w \sin \phi \qquad\qquad (2)$$

$$F_w' = -F_v \sin \phi + F_w \cos \phi$$

Consider the following sketch which is drawn in the $Y' = 0$ plane. The angle α_ℓ is the local "angle of attack" due to twist and camber.
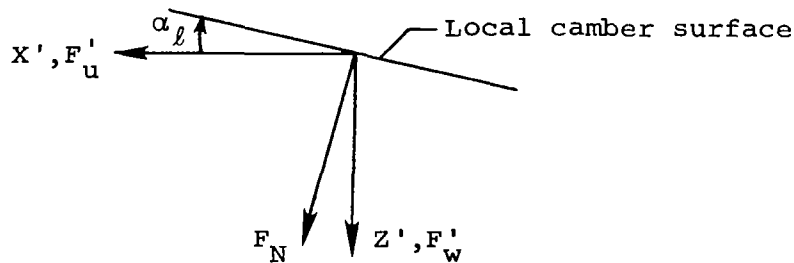
The influence function normal to the surface is

$$F_N = F_w' \cos \alpha_\ell + F_u' \sin \alpha_\ell \qquad\qquad (3)$$

If $V_{\Gamma_w, \nu, n}$ is the normal velocity induced by the nth wing vortex at the νth control point

$$\frac{V_{\Gamma_w, \nu, n}}{V} = \frac{\Gamma_n}{4\pi V} F_{N_{\nu, n}} \qquad\qquad (4)$$

Then, using equations (2) and (3), the first term in equation (1) is

$$\frac{1}{V} \sum_{n=1}^{M} V_{\Gamma_w, \nu, n} = \sum_{n=1}^{M} \frac{\Gamma_n}{4\pi V} \left(F_{w_{\nu, n}} \cos \phi_\nu \cos \alpha_{\ell_\nu} - F_{v_{\nu, n}} \sin \phi_\nu \cos \alpha_{\ell_\nu} \right.$$

$$\left. + F_{u_{\nu, n}} \sin \alpha_{\ell_\nu} \right) \qquad\qquad (5)$$

In order to evaluate the second term in equation (1), the wing boundary condition, the flap coordinate system must be defined. The wing and flap coordinate systems are shown in figure 2(b). The angle δ_{xz} is

the flap deflection angle and is measured in a streamwise plane parallel to the X,Z plane. The flap coordinate system is obtained by rotating the wing system about the Y axis by the angle δ_{xz} and then translating to the flap inboard-side leading edge. The influence functions F_{u_f}, F_{v_f} and F_{w_f} are known in the flap coordinate system. They can be resolved into the wing coordinate system by

$$\left. \begin{array}{l} F_u = F_{u_f} \cos \delta_{xz} + F_{w_f} \sin \delta_{xz} \\[2mm] F_v = F_{v_f} \\[2mm] F_w = -F_{u_f} \sin \delta_{xz} + F_{w_f} \cos \delta_{xz} \end{array} \right\} \tag{6}$$

Using the above expressions and equations (2) and (3), the influence function normal to the local camber surface is

$$F_{N_f} = F_{w_f}(\cos \phi \cos \alpha_\ell \cos \delta_{xz} + \sin \alpha_\ell \sin \delta_{xz}) - F_{v_f} \sin \phi \cos \alpha_\ell$$

$$+ F_{u_f}(\sin \alpha_\ell \cos \delta_{xz} - \cos \phi \cos \alpha_\ell \sin \delta_{xz}) \tag{7}$$

The normal velocity induced by the nth flap vortex at the νth wing control point is

$$\frac{V_{\Gamma_f, \nu, n}}{V} = \frac{\Gamma_n}{4\pi V} F_{N_f, \nu, n} \tag{8}$$

The second term in equation (1) is evaluated by summing over all flap vortices

$$\frac{1}{V} \sum_{n=1}^{NFLAPS} \sum_{n=1}^{NF(j)} V_{\Gamma_f, \nu, n} = \sum_{j=1}^{NFLAPS} \sum_{n=1}^{NF(j)} \left[\frac{\Gamma_{n,j}}{4\pi V} F_{w_f, \nu, n} \left(\cos \phi_\nu \cos \alpha_{\ell_\nu} \cos \delta_{xz_j} \right. \right.$$

$$\left. + \sin \alpha_{\ell_\nu} \sin \delta_{xz_j} \right) - F_{v_f, \nu, n} \sin \phi_\nu \cos \alpha_{\ell_\nu}$$

$$+ F_{u_f, \nu, n} \left(\sin \alpha_{\ell_\nu} \cos \delta_{xz_j} - \cos \phi \cos \alpha_{\ell_\nu} \sin \delta_{xz_j} \right) \right]$$

$$\tag{9}$$

11

The third term in equation (1) is the component of the free-stream velocity normal to the wing camber surface at the νth control point.
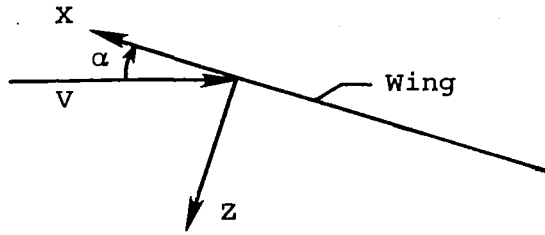
From the above sketch it is seen that

$$
\left.
\begin{aligned}
F_u &= -V \cos \alpha \\[2mm]
F_v &= 0 \\[2mm]
F_w &= -V \sin \alpha
\end{aligned}
\right\}
\tag{10}
$$

Equations (2), (3), and (10) give

$$
\frac{V_{N,\nu}}{V} = -\sin \alpha \cos \phi_\nu \cos \alpha_{\ell_\nu} - \cos \alpha \sin \alpha_{\ell_\nu}
\tag{11}
$$

The fourth term in equation (4) is the velocity normal to the wing surface produced by other sources. In the present application, these sources are the engine wakes. Assume these velocities are known in the wing coordinate system and are positive in the positive X,Y,Z directions. Then

$$
\left.
\begin{aligned}
F_u &= u_{i,\nu} \\[2mm]
F_v &= v_{i,\nu} \\[2mm]
F_w &= w_{i,\nu}
\end{aligned}
\right\}
\tag{12}
$$

at the νth control point, and with equations (2) and (3),

$$
\frac{V_{i,\nu}}{V} = \frac{w_{i,\nu}}{V} \cos \phi_\nu \cos \alpha_{\ell_\nu} - \frac{v_{i,\nu}}{V} \sin \phi_\nu \cos \alpha_{\ell_\nu} + \frac{u_{i,\nu}}{V} \sin \alpha_{\ell_\nu}
\tag{13}
$$

12

Substituting equations (5), (9), (11), and (13) into equation (1) and putting the known quantities on the right-hand side of the equal sign, the final form of the wing boundary condition at the νth control point on the wing is

$$\sum_{n=1}^{M} \frac{\Gamma_n}{4\pi V} \left(F_{w_{\nu,n}} \cos\phi_\nu \cos\alpha_{\ell_\nu} - F_{v_{\nu,n}} \sin\phi_\nu \cos\alpha_{\ell_\nu} + F_{u_{\nu,n}} \sin\alpha_{\ell_\nu} \right)$$

$$+ \sum_{j=1}^{NFLAPS} \sum_{n=1}^{NF(j)} \frac{\Gamma_n}{4\pi V} \left[F_{w_f,\nu,n}\left(\cos\phi_\nu \cos\alpha_{\ell_\nu} \cos\delta_{xz_j} + \sin\alpha_{\ell_\nu} \sin\delta_{xz_j}\right) \right.$$

$$\left. - F_{v_f,\nu,n}\sin\phi_\nu \cos\alpha_{\ell_\nu} + F_{u_f,\nu,n}\left(\sin\alpha_{\ell_\nu} \cos\delta_{xz_j} - \cos\phi_\nu \cos\alpha_{\ell_\nu} \sin\delta_{xz_j}\right) \right]$$

$$= \left(\sin\alpha - \frac{w_{i,\nu}}{V}\right) \cos\phi_\nu \cos\alpha_{\ell_\nu} + \frac{v_{i,\nu}}{V} \sin\phi_\nu \cos\alpha_{\ell_\nu} + \left(\cos\alpha - \frac{u_{i,\nu}}{V}\right) \sin\alpha_{\ell_\nu}$$

$$(14)$$

Flap boundary conditions.- The flap boundary condition can be derived in the same manner as the wing boundary condition. The resulting boundary condition at the νth control point on the ith flap is

$$\sum_{n=1}^{M} \frac{\Gamma_n}{4\pi V} \left[F_{w_{\nu,n}}\left(\cos\phi_{f_\nu} \cos\delta_{\ell_\nu} \cos\delta_{xz_i} - \sin\delta_{\ell_\nu} \sin\delta_{xz_i}\right) \right.$$

$$\left. - F_{v_{\nu,n}}\sin\phi_{f_\nu} \cos\delta_{\ell_\nu} + F_{u_{\nu,n}}\left(\sin\delta_{\ell_\nu} \cos\delta_{xz_i} + \cos\phi_{f_\nu} \cos\delta_{\ell_\nu} \sin\delta_{xz_i}\right) \right]$$

$$+ \sum_{j=1}^{NFLAPS} \sum_{n=1}^{NF(j)} \frac{\Gamma_n}{4\pi V} \left\{ F_{w_f,\nu,n}\left[\cos\phi_{f_\nu} \cos\delta_{\ell_\nu} \cos\left(\delta_{xz_i} - \delta_{xz_j}\right) \right.\right.$$

$$\left. - \sin\delta_{\ell_\nu} \sin\left(\delta_{xz_i} - \delta_{xz_j}\right)\right] - F_{v_f,\nu,n}\sin\phi_{f_\nu} \cos\delta_{\ell_\nu}$$

$$\left. + F_{u_f,\nu,n}\left[\sin\delta_{\ell_\nu} \cos\left(\delta_{xz_i} - \delta_{xz_j}\right) + \cos\phi_{f_\nu} \cos\delta_{\ell_\nu} \sin\left(\delta_{xz_i} - \delta_{xz_j}\right)\right]\right\}$$

13

$$= \sin\left(\alpha + \delta_{xz_i}\right)\cos\phi_{f_\nu}\cos\delta_{\ell_\nu} + \cos\left(\alpha + \delta_{xz_i}\right)\sin\delta_{\ell_\nu}$$

$$- \frac{w_{i,\nu}}{V}\left(\cos\phi_{f_\nu}\cos\delta_{\ell_\nu}\cos\delta_{xz_i} - \sin\delta_{\ell_\nu}\sin\delta_{xz_i}\right) + \frac{v_{i,\nu}}{V}\sin\phi_{f_\nu}\cos\delta_{\ell_\nu}$$

$$- \frac{u_{i,\nu}}{V}\left(\sin\delta_{\ell_\nu}\cos\delta_{xz_i} + \cos\phi_{f_\nu}\cos\delta_{\ell_\nu}\sin\delta_{xz_i}\right) \tag{15}$$

In this equation, ϕ_{f_ν} is the dihedral angle of the flap containing the νth control point and δ_{ℓ_ν} is the local "angle of attack" due to twist and camber at this point. The angle δ_{xz_i} is the deflection angle of the flap containing the control point and δ_{xz_j} is the deflection angle of the flap in which the influencing vortex originates.

Influence functions.- The functions F_u, F_v, F_w and $F_{u_f}, F_{v_f}, F_{w_f}$ are influence functions relating the velocity components induced at some point by a horseshoe vortex to the circulation strength. In reference 3 a horseshoe vortex was considered to have three parts: a bound leg and two trailing legs extending to infinity in the plane of the surface containing the bound leg. Figure 1 shows the horseshoe vortex arrangement used in the present method. Except for a vortex originating in the last surface at a spanwise location, the trailing legs are composed of a series of finite length segments followed by two semi-infinite length segments. Thus, the equations given in reference 3 for the influence functions are not applicable, in general, to the present method.

General expressions are required for the influence functions for a finite length vortex filament and a semi-infinite filament. Such expressions are available in reference 6. For completeness, they will be repeated here.

The coordinate system for a finite length vortex segment is shown in figure 3(a). The x,y,z coordinate system is that associated with the surface in which the horseshoe vortex containing this segment originated. In that system there is a vortex filament extending from x_1, y_1, z_1 to x_2, y_2, z_2 with vorticity directed as shown. The influence functions at point x,y,z are, from the Biot-Savart law,

$$f_u = \frac{a}{\sqrt{a^2 + b^2 + c^2}} \left(\frac{1}{r}\right) (\cos \theta_1 - \cos \theta_2)$$

$$f_v = \frac{b}{\sqrt{a^2 + b^2 + c^2}} \left(\frac{1}{r}\right) (\cos \theta_1 - \cos \theta_2) \tag{16}$$

$$f_w = \frac{c}{\sqrt{a^2 + b^2 + c^2}} \left(\frac{1}{r}\right) (\cos \theta_1 - \cos \theta_2)$$

In these equations

$$a = (y_2 - y_1)(z - z_1) - (y - y_1)(z_2 - z_1)$$

$$b = (z_2 - z_1)(x - x_1) - (z - z_1)(x_2 - x_1) \tag{17}$$

$$c = (x_2 - x_1)(y - y_1) - (x - x_1)(y_2 - y_1)$$

and

$$\cos \theta_2 = \frac{R_1^2 - R_2^2 - L^2}{2LR_2}$$

$$\cos \theta_1 = \frac{R_1^2 - R_2^2 + L^2}{2LR_1} \tag{18}$$

$$r = R_2 \sqrt{1 - \cos^2 \theta_2}$$

where

$$L = \sqrt{(x_2 - x_1)^2 + (y_2 - y_1)^2 + (z_2 - z_1)^2}$$

$$R_1 = \sqrt{(x - x_1)^2 + (y - y_1)^2 + (z - z_1)^2} \tag{19}$$

$$R_2 = \sqrt{(x - x_2)^2 + (y - y_2)^2 + (z - z_2)^2}$$

15

Similarly, for the semi-infinite length vortex filament shown in figure 3(b),

$$
\left.
\begin{aligned}
f_u &= \frac{-d}{\sqrt{d^2 + e^2 + f^2}} \left(\frac{1}{r'}\right)(1 - \cos \theta') \\[2ex]
f_v &= \frac{-e}{\sqrt{d^2 + e^2 + f^2}} \left(\frac{1}{r'}\right)(1 - \cos \theta') \\[2ex]
f_w &= \frac{-f}{\sqrt{d^2 + e^2 + f^2}} \left(\frac{1}{r'}\right)(1 - \cos \theta')
\end{aligned}
\right\} \quad (20)
$$

where

$$
\left.
\begin{aligned}
d &= A_y(z - z_1) - A_z(y - y_1) \\[1.5ex]
e &= A_z(x - x_1) - A_x(z - z_1) \\[1.5ex]
f &= A_x(y - y_1) - A_y(x - x_1)
\end{aligned}
\right\} \quad (21)
$$

The positive sense of vorticity is shown in figure 3(b). The quantities A_x, A_y, A_z in equations (21) are the direction cosines of the vortex filament in a direction from x_1, y_1, z_1 to infinity. Also,

$$
\left.
\begin{aligned}
\cos \theta' &= -\left[\frac{A_x(x - x_1) + A_y(y - y_1) + A_z(z - z_1)}{\sqrt{(x - x_1)^2 + (y - y_1)^2 + (z - z_1)^2}}\right] \\[2ex]
r' &= R'\sqrt{1 - \cos^2\theta'} \\[2ex]
R' &= \sqrt{(x - x_1)^2 + (y - y_1)^2 + (z - z_1)^2}
\end{aligned}
\right\} \quad (22)
$$

In order to evaluate the influence functions appearing in equations (14) and (15), equations (16) through (19) are used to evaluate the influence of the bound leg and all finite length trailing leg segments of both the right and left trailing legs. Equations (20) through (22) are used to evaluate the influence of the two semi-infinite trailing legs. The influence functions in equations (14) and (15) include the influence of the vortex on the left wing panel or left-side

16

flap and that due to the corresponding vortex on the right wing panel or right flap at the left-side control point.

Aerodynamic forces and moments.- Once the strengths of the vortices have been determined by solving the set of simultaneous equations given by equations (14) and (15), the aerodynamic forces acting on each area element on the wing or flap can be calculated. The Kutta-Joukowski law for aerodynamic forces on a vortex filament is used. The method of calculating the forces is the same as that described in reference 3 except that certain terms omitted there are now included. Following the procedure of reference 3 the axial-force coefficient produced by one of the area elements on the left wing panel is

$$C_A = - \frac{2\Gamma}{SV} (2s) \left(\cos \phi \sin \alpha - \frac{w}{V} \cos \phi + \frac{v}{V} \sin \phi \right) \qquad (23)$$

Similarly, the normal-force coefficient is

$$C_N = \frac{2\Gamma}{SV} (2s) \left(\frac{v}{V} \tan \psi + \cos \alpha \cos \phi - \frac{u}{V} \cos \phi \right)$$

$$+ \frac{\Sigma\Gamma}{SV} \left[\left(\frac{cv_1}{V} \right)_{left} - \left(\frac{cv_1}{V} \right)_{right} \right] \qquad (24)$$

Positive directions of the forces are shown in figure 4(a). In the above equations, 2s is the width of the panel in the wing chordal plane. The velocities u, v, and w, positive in the positive X,Y,Z directions, are those induced at the bound-leg midpoint by the entire wing-flap vortex lattice plus velocities due to the engine wake, if present. The angle ψ is the sweep angle of the bound leg, positive if swept back.

The second term in equation (24) is the net force on all of the vortex trailing legs lying on the two side edges of the panel. The vortices are only those lying in the chordwise strip containing the panel. In equation (24), $\Sigma\Gamma$ is the sum of the strengths of these vortices, c is the length of the panel side edge, and v_1 is the vortex lattice and engine wake induced velocity at the three-quarter chord location of the side edge. The subscripts left and right refer to the left side edge and right side edge.

Similar expressions can be written for the forces acting on a panel on a flap. Positive directions of the forces are shown in figure 4(b). The axial-force coefficient is,

$$C_{A_f} = -\frac{2\Gamma}{SV}(2s)\left[\cos\phi_f\cos(\alpha+\delta_{xz}) - \frac{w_f}{V}\cos\phi_f + \frac{u_f}{V}\sin\phi_f\right] \tag{25}$$

the side-force coefficient is,

$$C_{Y_f} = \frac{2\Gamma}{SV}(2s)\left[\cos(\alpha+\delta_{xz})\sin\phi_f - \frac{u_f}{V}\sin\phi_f - \sin(\alpha+\delta_{xz})\tan\psi_f\right.$$
$$\left. + \frac{w_f}{V}\tan\psi_f\right] + \frac{\Sigma\Gamma}{SV}\left[\left(c\,\frac{w_{f_1}}{V}\right)_{left} - \left(c\,\frac{w_{f_1}}{V}\right)_{right}\right] \tag{26}$$

and the normal-force coefficient is,

$$C_{N_f} = \frac{2\Gamma}{SV}(2s)\left[\frac{v_f}{V}\tan\psi_f + \cos(\alpha+\delta_{xz})\cos\phi_f - \frac{u_f}{V}\cos\phi_f\right]$$
$$+ \frac{\Sigma\Gamma}{SV}\left[\left(c\,\frac{v_{f_1}}{V}\right)_{left} - \left(c\,\frac{v_{f_1}}{V}\right)_{right}\right] \tag{27}$$

The velocities u_f, v_f, w_f are positive in the positive X_f, Y_f, Z_f directions.

The elemental panel forces given by equations (23) through (27) can be used to calculate spanwise load distributions by summing over the area elements in a spanwise row and total forces and moments can be determined by then summing spanwise. Moments can be determined by using the panel forces with the appropriate moment arm.

Vortex Ring Jet Wake Model

A potential flow model of the wake from a turbofan engine is presented in reference 3. This model has a vorticity distribution placed on the specified boundary of an expanding, circular cross-section jet. This is modeled by a series of vortex rings coaxial with the prescribed centerline of the jet. Each ring represents a finite increment of length of the cylinder, and the vortex strength of each individual ring is equal to the net vorticity on the incremental length of cylinder which it replaces. A sketch of this circular ring model reproduced from reference 3, is shown in figure 5 along with some typical velocity profiles at various distances downstream of the beginning of the jet. This

18

model represents the mass, momentum, and entrainment characteristics of a turbulent, coflowing jet. While the velocity profile within the jet is approximated by a uniform profile, the induced velocities outside the jet are probably accurate, because they are related to the entrainment induced flow.

Flow surveys taken just aft of the trailing edge of an EBF model (ref. 7) indicate that an initially circular jet becomes distorted after interaction with the flap system. The distortion is such that the wake tends to flatten and become more elliptical than circular in cross section. Observations of free, nonaxisymmetric cross-section jets (refs. 8 and 9) show that these jets tend to become axisymmetric as they progress downstream. Thus, the most probable picture of an engine wake is one which has the wake leave the engine as a circular jet, become more elliptical as it approaches the flap, flatten as it passes under the flap system, and return gradually towards a circular section in the far field. In the case of large flap deflection angles, it is possible that the wake aft of the flap may roll up into a pair of vortices, as has been observed with circular jets issuing normal to a crossflow, but there are few observations on which to base any conclusion for EBF configurations.

On the basis of the EBF jet observations noted above, it was felt that the method of reference 3 should be augmented with an elliptical jet model which can be combined with the circular jet to produce a wake which can change continuously from circular to elliptical, with axis ratio variation to be arbitrary and selected on the best available information. This section, together with Appendices A and B, describe the development and use of such a model.

Velocity induced by an elliptic vortex ring.- Analogous to the circular ring, the first requirement of the elliptic jet model is a solution for the velocity components induced at an arbitrary field point by an elliptic vortex ring. The coordinate system and notation are shown in figure 6.

Unlike the circular ring, no solution was available for the induced velocity of the elliptical ring. Consequently, the solution was developed and is discussed in detail in Appendix A. Through the use of confocal elliptical coordinates, an analytical solution can be obtained. The basic solution for the velocity components, for one quadrant in a ring

coordinate system, are given as equations (A-23) through (A-25). These equations are used, with appropriate sign changes, to sum the contributions of all four quadrants of the ring. These velocity components can then be related to components in the jet and wing coordinate system through the nomenclature of figure 7 and equations (A-31) and (A-32). The solution is obtained in terms of certain integrals, J_n, which are developed in Appendix B.

Elliptic jet model.- The development of the elliptic cross-section potential flow jet model proceeds in similar fashion to the development of the circular jet model in reference 3. The assumption is made here that the jet begins with a circular cross section and becomes elliptical at any rate desired.

Consider for the moment that the jet vortex model is a constant radius, semi-infinite circular vortex cylinder with strength γ/V. The strength of this vortex cylinder is specified by the relation

$$\frac{\gamma}{V} = \frac{V_j}{V} - 1 \qquad (28)$$

where V_j is a uniform velocity across the engine exhaust exit. This jet velocity is given approximately as

$$\frac{V_j}{V} = \frac{1}{2}\left[1 + \sqrt{1 + 2C_T \frac{S\rho}{A_j \rho_j}} \right] \qquad (29)$$

where C_T is the thrust coefficient for a single jet and A_j is the exhaust exit area for a single jet.

Starting with a vortex cylinder with constant radius R_o and strength γ/V, the actual jet wake is modeled by distorting the cylinder to fit a prescribed centerline path and outer boundary. The continuous vorticity distribution on the new distorted cylinder is replaced by a closely spaced series of vortex rings coaxial with the jet centerline. Each ring represents a small increment of length of the jet, and each ring has a shape which corresponds to the specified jet boundary. The strength of the ring vorticity is equal to the net vorticity on the incremental length of the original cylinder. Thus, the semi-infinite length of the original cylinder is replaced with a finite length of vortex rings. As described in reference 3, the semi-infinite length cylinder can be approximated to any required accuracy in this manner.

20

The strength of any vortex ring along the jet is

$$\frac{\Gamma}{V} = \frac{\gamma}{V} \frac{P_o}{P} \Delta s \tag{30}$$

where P is the perimeter of the ring in question and Δs is the length of the wake represented by the ring. For an ellipse, the perimeter is

$$P = 4a \ E(k) \tag{31}$$

where $E(k)$ is a complete elliptic integral of the first kind, and

$$k^2 = 1 - \left(\frac{b}{a}\right)^2 \tag{32}$$

The quantities a and b are the semi-major and semi-minor axes of the ellipse. An approximate relation for the perimeter is

$$P \simeq 2\pi \sqrt{\frac{a^2 + b^2}{2}} \tag{33}$$

which is within 5 percent of equation (31) for $a/b \leq 3$.

From equation (30), the strength of the vortex ring decreases as its perimeter increases such that the product of Γ and the ring perimeter is constant for equally spaced rings (Δs = constant). This is equivalent to keeping the total vorticity on the cylinder constant. The induced velocity at any point in the field is calculated by summing the contributions from all the rings making up the model. Typical velocity profiles inside various elliptic jets are discussed in the results portion of this report.

Jet description.- As is the case in reference 3 for circular jets, the current model for elliptic cross-sectional jets requires three items to completely determine the analytical description of the jet. The first is the initial vortex ring strength from equation (28), which is related to the thrust and momentum in the jet. The remaining two items to be specified are the position and path of the centerline of the jet and the boundary of the jet.

The computer program described in reference 4 allows the centerline of the jet to move under the influences of the free-stream velocity, the wing and flap loading induced flow field, and the jet induced flow field. The objective in permitting the centerline to move is to be able to

locate the centerline along the streamline of the wing-flap-jet flow which leaves the center of the engine exhaust. This is an approximation to placing the singularities representing the jet along streamlines, which cannot be handled because of the limitations on cross-section shape (circle and ellipse). Thus, the jet centerline is free to move so that an iteration can be performed until convergence is attained between the centerline and streamline positions. Since each jet is free to move according to the local flow field induced along its centerline, the user need not specify the jet centerline in great detail prior to a calculation. In practical usage, the initial centerline may be assumed to be straight. The motion of the centerline is calculated in the following manner.

The path of the jet centerline is specified by a number of points on the centerline. At a point n, the induced flow field has the three components

$$\left.\begin{array}{l} \dfrac{u_n}{V} = \dfrac{u_j}{V} + \dfrac{u_w}{V} + \dfrac{u_\alpha}{V} \\[2em] \dfrac{w_n}{V} = \dfrac{w_j}{V} + \dfrac{w_w}{V} + \dfrac{w_\alpha}{V} \\[2em] \dfrac{v_n}{V} = \dfrac{v_j}{V} + \dfrac{v_w}{V} \end{array}\right\} \tag{34}$$

where

u_j, w_j, v_j are jet induced velocities

u_w, w_w, v_w are wing-flap induced velocities

u_α, w_α are free-stream components

The resultant flow angle in the X-Z plane is

$$\theta_n = \tan^{-1}\left(\dfrac{w_n}{u_n}\right) \tag{35}$$

and in the X-Y plane is

$$\sigma_n = \tan^{-1}\left(\dfrac{v_n}{u_n}\right) \tag{36}$$

22

Thus, the vertical flow angles at two consecutive points along the centerline appear as in the sketch below.
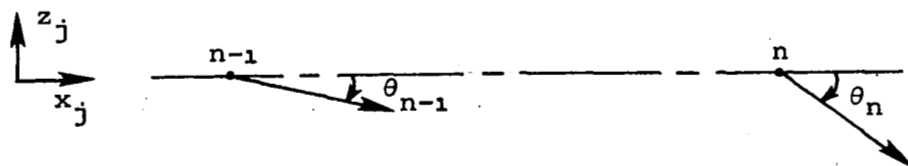
Assuming that the average flow angle between points $n-1$ and n is given by

$$\bar{\theta}_n = \frac{1}{2}(\theta_{n-1} + \theta_n) \tag{37}$$

a new vertical coordinate at point n based on the average flow angle is given by

$$z_n = z_{n-1} + (x_n - x_{n-1})\tan\bar{\theta}_n \tag{38}$$

Similarly, a new lateral coordinate at point n is given by

$$y_n = y_{n-1} + (x_n - x_{n-1})\tan\bar{\sigma}_n \tag{39}$$

where

$$\bar{\sigma}_n = \frac{1}{2}(\sigma_{n-1} + \sigma_n) \tag{40}$$

Starting at the engine exit with fixed coordinates and slope, the entire jet centerline is repositioned according to equations (38) and (39).

A limit is placed on the vertical deflection angle θ_n in accordance with the following considerations. It is well known experimentally that the flaps of an EBF configuration do not achieve 100-percent jet turning efficiency but a somewhat lower value which decreases with increasing flap angle. It was found in the calculations that with large flap deflections ($\delta_{xz} > 40°$), the predicted jet centerline slope would some-times equal or exceed the aft flap deflection angle, with the result that the predicted interference effects would be low because the jet was passing too far below the flap. Under those circumstances, if a limit on θ_n of the product of the measured jet turning efficiency and the flap deflection angle were imposed, the jet would pass closer to the flap, the interference effects would be larger, and the predicted and

measured force results were in good agreement. This was felt to be a reasonable limitation in view of the experimental turning efficiency results, and was incorporated in the computer program. If the computed value of θ_n from equation (37) exceeds a specified limit, θ_n is set equal to the limiting value. The remainder of the centerline calculation and iteration procedure is carried out as before.

To complete the description of the jet wake, the boundary of the jet must be specified at all points along the jet. In reference 3, an axisymmetric turbulent jet in a coflowing stream was defined using an analytical method presented in reference 10. The radius distribution of an axisymmetric jet is shown in figure 8 for various jet velocity ratios. Unfortunately, a similar series of curves is not available for noncircular cross-section jets; therefore, empirical evidence must be used where possible.

Elliptic and rectangular shaped jets exhausting into still air are described in references 8 and 9, and measured half-width boundaries are shown in figure 9. These data are not sufficient to describe the expansion of typical elliptic cross-section wakes occurring on EBF configurations, but they are shown here to illustrate several general points. The first is that elliptic and rectangular jets with similar axis ratios exhibit the same kind of expansion characteristics. It also appears that the minor axis expands at nearly the same rate as a circular jet. Figure 9 also illustrates that nonaxisymmetric jets exhausting into still air tend to become axisymmetric at large distances downstream.

Measured jet wake velocity profiles at a number of spanwise stations approximately one flap chord aft of the trailing edge of the last flap of a four-engine EBF configuration are presented in reference 7. The boundaries of three jets corresponding to total thrust coefficients of 1, 2, and 4 were deduced from these data. The thickness distributions of the jet are shown in figure 10 as solid lines. The spanwise extent of the jets is not well defined by the measurements; therefore, the extrapolated inboard and outboard portions of each jet are shown dashed. To illustrate the growth and spanwise spreading of each jet, the original jet cross-sectional areas are shown at their appropriate semispan stations as dashed lines. The relative vertical positions of the original jets and the measured profiles are not comparable as the jets aft of the flaps have been deflected downward.

The results of figure 10 show that the boundary of the jets tends to form an elliptical shape after interaction with the flap system. The jets also seem to move inboard toward the fuselage instead of outboard toward the wing tip. This motion seems to become more pronounced as the thrust coefficient increases.

The data of reference 7 can also be used to examine the expansion ratio of the jets. For this purpose, areas of the jets were obtained by graphical integration from data like that of figure 10 and divided by the initial areas of the two jets. The results for the station just downstream of the flap trailing edge (about 9 initial jet radii downstream of the jet exit plane) are shown in figure 11(a) as a function of C_μ and jet velocity ratio (from eq. (29)). The shaded area represents the scatter and the solid line is the least-squares fit to the data.

If we assume the jet area shown in figure 10 is redistributed into a circular cross section for each individual jet, an equivalent radius ratio, R/R_0, can be calculated for each thrust coefficient as simply $\sqrt{A/A_0}$. This result is shown in figure 11(b) where it is compared with the radius ratio of an axisymmetric jet from figure 8. Figure 11(b) indicates that an axisymmetric jet alone expands at a faster rate than an initially axisymmetric jet under the influence of a wing and flap. This kind of information is important in selecting a spreading rate for a typical EBF jet.

EBF Interference Calculation Procedure

Calculation of the aerodynamic loading of a wing-flap configuration under the influence of the jet wake of a turbofan engine is done with the combination of the two potential flow models described in the preceding sections. The two flow models are combined by superposition. The jet model induces a velocity field on the wing and flap which produces an interference loading on the lifting surfaces. The wing and flap loadings induce a velocity field in the vicinity of the jet and tend to deflect the jet away from these surfaces. It is assumed that the engine thrust is unaffected by the presence of the wing-flap. Because of the mutual interaction between the jet and lifting surfaces, either a simultaneous solution involving both flow models or an iterative solution is required. The iterative approach was chosen in reference 3 and that approach is continued, with some refinements, in this report. The solution is carried out in the following manner.

Before any calculations are made, the jet centerline is positioned with respect to the wing and flap. The initial location of the centerline can be based on some a priori knowledge of the flow field beneath the wing and flap system or it can be located in a strictly arbitary fashion. For example, it is quite acceptable to choose the initial jet centerline to be a straight line aft from the engine exhaust.

The (expanding) jet boundary and cross-section shape distribution should be chosen according to whatever procedure seems most appropriate, and this distribution, which will be unchanged from this point on, is placed on the centerline to define an initial jet wake. The jet induced velocity field is computed at selected control points on the lifting surfaces and the circulation distribution on the wing and flaps is obtained such that the tangency boundary condition is satisfied at each control point.

At this point in the solution, the boundary condition on the wing and flap surfaces is satisfied but the jet position has not been influenced by the presence of the wing and flap. The wing-flap influence consists of modifying the jet location to cause the jet centerline to lie along a streamline of the combined jet-wing-flap flow. The initial jet centerline is then adjusted by computing the total flow field at a number of points on the centerline and moving the centerline to a new position such that it lies along the computed flow direction at the specified points. This completes the first iteration of the solution. In this situation, the wing and flap loading is not compatible with the jet flow field corresponding to the new position of the jet. Thus, a second iteration is needed.

The flow field corresponding to the adjusted jet position is computed, and a new wing-flap loading distribution is obtained. The jet centerline is again moved to lie along the new flow directions. This procedure is continued until either the centerline position or the total wing and flap loading converges to within a desired tolerance. With a converged solution, the total flow is tangent to the wing and flap surfaces and the jet centerline lies along a streamline of the flow.

The methods of analysis described in the previous section have been evaluated in the following manner. Each flow model (the lifting surface and the jet wake) is examined separately to determine its individual characteristics. Where possible, comparisons with data are made to assist in the evaluation. After the individual flow models are examined, they are combined to perform several calculations on EBF configurations. Convergence characteristics of the jet wake centerline iteration procedure are first examined. Comparisons with experimental data are then made and used to evaluate the total EBF prediction method. The data comparisons and results are discussed below.

Wing-Flap Model

The first configuration used to check out the deflected wake vortex-lattice method is an aspect ratio 6 rectangular wing with a single slotted flap (ref. 11). The Fowler-type flap has a chord that is 30 percent of the wing-alone chord and is deflected 40°. The vortex-lattice arrangement used for this configuration is 8 chordwise by 13 spanwise on the wing semispan and 4 by 13 on the flap.

The predicted results for this wing (and following configurations) can be compared with similar results from reference 3 to illustrate two features of the present method: the deflected horseshoe vortex trailing legs and the gap between the wing and flap. The lattice arrangement is somewhat different between the two calculations, but the work of Appendix A of reference 3 indicates that the lift and moment should be converged with both lattice arrangements.

Comparisons of measured and predicted lift and pitching-moment coefficients are shown in figure 12(a). With zero flap deflection, the deflected wake method reduces to the undeflected wake method and the results are identical; therefore, only one predicted curve is shown. The agreement between measured and predicted lift curves is excellent up to the point where the lift curve starts to bend due to separation or stall. The predicted pitching-moment curve for this configuration is also in reasonably good agreement with the experimental results. The effect of the lift on the fuselage is not considered in these comparisons. An estimate of the fuselage lift and pitching-moment coefficients given by slender-body theory results in values of 0.01 and

0.02, respectively, at 10° angle of attack. Inclusion of the fuselage pitching moment would tend to improve the agreement on moment curve slope.

The effect of deflecting the trailing legs of the horseshoe vortices is illustrated in the upper portion of figure 12(a). In general, it is observed that when the trailing vorticity is allowed to move aft in the plane of the surface from which it originates, the predicted lift coefficient is larger than when the trailing vorticity is allowed to bend around the flap surfaces and finally move aft in the plane of the last flap. Numerically, the lift coefficients corresponding to the undeflected wake are approximately 10 percent higher than those from the deflected wake calculations and the lift curve slope is slightly higher. The pitching-moment coefficients corresponding to the deflected wake are in much better agreement with experiment, both in magnitude and slope, than the results obtained considering the wake to be undeflected.

The model used in reference 11 has a slotted flap, but the size of the gap is not specified. The effect of gap size is shown in figure 12(a), where predicted results for gaps of 0.02 c and 0.03 c are shown for both deflected and undeflected wakes. The results show that increasing the gap size decreases the total lift and increases the nose-down pitching moment. A closed gap was considered for the previous undeflected wake calculations and these results are consistent with those just discussed. The effect of the gap size is not insignificant; and when using the wing-flap vortex-lattice method described herein, one should take care in modeling the gaps between lifting surfaces correctly.

Measured and predicted chordwise pressure distributions on the wing and flap at two angles of attack, 0.47° and 5.65°, are shown in figure 12(b). The predicted pressure distributions from both the deflected and undeflected wake methods presume the gap between the wing and flap to be 0.02 c. The undeflected wake model predicts a slightly higher pressure difference on both wing and flap, confirming the previous results for lift coefficients, although the general shapes of the curves are very similar.

A second set of results used for comparison purposes consists of a chordwise pressure distribution on a swept wing with a partial span flap (ref. 12). This configuration, shown in the sketch in figure 13, has a 35° leading-edge sweep angle, a flap span approximately one half the

semispan, and a flap chord equal to 20 percent of the wing chord. Calculations were made at zero degrees angle of attack and 10° flap deflection angle. The lattice arrangement has 12 spanwise vortices by 8 chordwise on the wing and 4 chordwise on the flap. There is no gap between the wing and the flap. The data were taken at a Mach number of 0.6; but since the wing-flap program is incompressible, no correction was made for compressibility effects. The predicted pressure distribution from both vortex-lattice methods are in good agreement with each other as are the total lift and pitching-moment coefficients on the wing-flap configuration. The predicted pressure distribution has the same shape as the measurements, including the loading peak near the wing and flap junction.

Finally, the effect of allowing the trailing legs of the horseshoe vortices to remain attached to the flaps is examined on a typical EBF transport model having a triple-slotted, full-span flap system (ref. 13). The lattice arrangement used on this configuration consists of 15 spanwise vortices on the semispan and 4 chordwise vortices on the wing, 1 chordwise on the first flap, and 2 chordwise vortices on each of the two aft flaps. The lattice elements are not evenly distributed in the spanwise direction, as this same lattice arrangement is used later for power-on calculations (fig. 26). The model used in reference 13 has a large fuselage, four nacelles beneath the wings, and a leading-edge slat deflected 55°. None of these items have been accounted for in the predictions shown in figure 14.

The measured and predicted lift and pitching-moment coefficients are shown in figure 14. As illustrated in figure 12(a), the effects of deflecting the trailing vorticity are to: (1) decrease the predicted lift coefficients over the entire range of angles of attack, (2) decrease the predicted lift curve slope a small amount, and (3) increase the nose-up pitching-moment coefficients. The net result of allowing the trailing vorticity to follow the flaps is to improve agreement with experimental results for both lift and pitching moments.

The above comparisons between measured and predicted longitudinal aerodynamic characteristics of wings with flaps indicate that better accuracy is to be obtained by allowing the trailing vorticity to deflect with the flap system. In particular, the predicted pitching-moment coefficients and moment curve slope tend to be in better agreement with experiment when the deflected wake model is used. Unless otherwise

specified, all further results presented in this report will correspond to the deflected wake prediction method.

Jet Wake Model

Single ring characteristics.- Since the complete jet is made up of a series of vortex rings, it is appropriate that the characteristics of a single, elliptic vortex ring be examined. The induced velocity field due to a circular vortex ring is well documented in reference 14; however, similar results for an elliptic vortex ring are not available so far as the authors can determine. In figure 15, the induced axial velocity in the plane of the ring is shown for a series of elliptic rings with varying axis ratios. The axial velocity distribution along both the minor (fig. 15(a)) and major (fig. 15(b)) axes are very similar and illustrate the singular behavior associated with induced velocities close to a vortex filament. The velocity distributions are similar for a wide range of axis ratios and there is effectively little change beyond an axis ratio of 10. The axial velocity outside the ring on the major axis tends to become very small as the axis ratio increases, because the ring configuration approaches two parallel vortex filaments with little periphery to induce a velocity outside the end of the ring.

The induced axial and vertical velocities outside the plane of the vortex rings are easily calculated using the analysis presented in the appendices. Some induced velocities at various points on the vertical plane of symmetry are shown in Tables I and II for elliptic vortex rings of different axis ratios. The limits of a circular ring and two infinite vortex filaments are also shown in the tables. There appear to be some numerical problems in calculating induced velocities in the plane of high-aspect-ratio elliptic vortex rings ($a/b \geq 5$) near the edge of the ring. There is a singularity on the ring itself, and calculated velocities near the ring show some inconsistency. This is not significant, since this region of a vortex ring is never used in computing jet induced velocities. As described in reference 3, field points which fall between two adjacent rings but very close to one are treated as if they lie off the plane of the vortex ring exactly half way between two adjacent rings. This correction is carried out to achieve smooth induced velocity profiles which are in agreement with the profiles which would be obtained from a uniform distribution of vorticity on a semi-infinite cylinder.

30

Jet characteristics.- The jet model is made up of a series of coaxial vortex rings of elliptic shape, and the induced flow field at any point is determined by adding the contribution of each ring in the jet model. Even though the induced velocity from a single ring is highly nonuniform as shown in figure 15 and Tables I and II, the total induced velocity field associated with the complete jet is remarkably smooth and predictable. The jet induced axial velocity profiles at various points inside a circular jet are discussed in reference 3 and illustrated in figure 5. It is seen that the axial velocity profile inside a circular jet is uniform inside the boundary of the jet and nearly zero outside the boundary. Several elliptic cross-section jets with various axis ratios are described as follows. In each of the jets to be described, the jet length and spacing between rings is the same, and the jet is allowed to expand to four times its initial area.

A sketch of a typical jet model used in the following discussion is shown at the top of figure 16(a). The cross-section shape of each jet is similar over its entire length as the axis ratio is kept constant. In figure 16(a), predicted axial velocity profiles in the vertical plane of symmetry for three jets are shown. The jet cross sections vary from circular (a:b = 1:1) to moderately elliptical (a:b = 3:1), and the axis lengths are chosen such that the cross-sectional areas of the three jets are the same at all axial stations along the centerline. The profiles shown in figure 16(a) are computed at the end of a straight section of jet (x_j = 5 in the sketch) before any expansion has occurred. As was the case in reference 3, the profiles are nearly uniform across the jet, and the only difference between the circular jet and the two elliptic jets occurs near the edges of the jets.

Predicted axial velocity profiles across a series of elliptic jets at a point where the local perimeter (P) is 1.25 times greater than the initial perimeter (P_o) are shown in figure 16(b). These profiles are also shown in the vertical plane of symmetry. The magnitude of the maximum velocity in the jet is nearly the same for each of the various shape jets, but since some expansion has taken place, the magnitude is less than that shown in figure 16(a). Two very high-aspect-ratio elliptic jets, 5:1 and 10:1, are considered in figure 16(b). Their velocity profiles are similar to the other jets with the exception that the nonuniformity near the edges of the jets appears to increase as the cross sections become more elliptical. For all practical purposes, the

axial velocity profiles may be considered uniform inside the boundaries of the elliptic jets considered thus far.

Predicted axial velocity profiles in the horizontal plane of symmetry of two elliptic jets are shown in figure 16(c). These profiles are similar to those just described except that they are more uniform across the width of the jet than across the height. The induced axial velocity tends to increase slightly from the centerline to the jet boundary and there is less difference between profiles as the jet aspect ratio increases.

Finally, a series of profiles at various lateral stations across a 3:1 elliptic jet are shown in figure 16(d). As would be expected, these profiles are all similar.

The axial velocity profiles presented in figure 16 are typical of the results obtained from the vortex ring jet model. Varying the expansion rates does not change the shape of the profiles, nor does changing the cross-sectional shape of the jet. For example, a jet may begin circular and gradually change to elliptical with distance downstream and the local profiles will still appear as those just discussed.

As the jet expands with distance along the centerline, the induced axial velocity on the centerline decreases. The axial velocity is inversely proportional to the local perimeter of the jet, as illustrated in figure 17, where the axial velocity, normalized by the initial vortex cylinder strength, is shown as a function of the perimeter, normalized by the initial perimeter of the jet. A number of jets, ranging from circular to a 10:1 elliptical jet, are shown on this correlation curve. Various expansion rates are represented by the points in this figure, from nonexpanding to very large expansion rates. There is some small deviation from the correlation curve as the jet expands to a perimeter approximately double its original perimeter.

Using the information in figure 17, it can be shown that the mass inside the boundaries of an expanding circular vortex ring jet model is not constant but is increasing with distance along the jet as long as the perimeter of the jet is increasing. This is illustrated in figure 18 where the predicted ratio of the local mass flow to the initial mass flow in the jet is shown versus the perimeter ratio. This curve was obtained from the same series of jets illustrated in figure 17. Figure 18 indicates that at any point along an expanding jet, the mass ratio is determined by the local perimeter of the vortex rings; or conversely, if a

32

specific mass ratio at a point in a jet is desired, it can be obtained by choosing the correct expansion of the vortex rings.

Measured axial velocity profiles in the wake of a JT15D-1 jet engine mounted beneath a wing are available in reference 13 for a range of thrust levels. Two profiles corresponding to thrusts of 5338 newtons (1200 lbs) and 3114 newtons (700 lbs) are shown in figures 19(a) and (b), respectively. The profiles were measured on both the upper (wing) side and the lower (free) side of the engine centerline (assumed straight) at a point approximately two wake diameters downstream of the engine exit. The data indicate that the wake is nearly symmetric about the centerline; therefore, one half of the profiles is illustrated with a faired curve. Since the velocity profile was measured in a single vertical plane through the centerline, we must assume the jet to be axisymmetric.

A circular jet model was designed to expand at a rate that would produce the same mass flow at the measured profile station, and the resulting predicted velocity profile is shown dashed in figures 19(a) and (b). A comparison of the momentum in the measured and predicted jets indicates that the real jet has approximately 5 percent more momentum than the predicted jet. Therefore, it is possible to match satisfactorily both the mass and momentum of the real jet with a vortex ring model. Any interference calculations taking place inside the jet boundaries will be reasonably accurate when averaged over the area of the complete wake, but there may be certain inaccuracies locally inside the wake due to differences in the shape of the velocity profile. This result will be illustrated in more detail when the predicted span loadings on an EBF configuration are compared with data.

Centerline calculation.- An important feature of the EBF prediction method is the calculation of the deflection of a jet due to the influence of the flow field induced by the loading on the wing and flap surfaces. Ideally, the centerline calculation procedure described previously should be checked out by comparing the predicted path of a jet in a nonuniform velocity field with the actual path, but data of this type are not available.

A large amount of jet path data are available in reference 15 for different strength jets directed into a uniform crossflow at various angles. These data are summarized in the following empirically determined equation:

$$\frac{x_j}{d} = \frac{(V/V_j)^2}{4 \sin^2 \theta_o} \left(\frac{z_j}{d}\right)^3 - \left(\frac{z_j}{d}\right) \cot \theta_o \qquad (41)$$

which is equation (4) of reference 15.

The centerline calculation method was applied to this jet flow case to evaluate the iteration procedure. The vortex ring model of the jet was based on a typical axisymmetric jet expansion rate and the jet centerline was assumed to be straight initially. Predicted centerlines for two jets directed at a 30° angle to the free stream are shown in figures 20(a) and (b) for jet velocity ratios 8.85 and 2.81, respectively. In both cases, the predicted centerlines agree very well with the center-lines given by equation (41).

The agreement starts to deteriorate beyond ten jet diameters down-stream of the origin. This is approximately the end of the initial region of a jet where the potential core disappears. The jet expansion rate changes at this point, which changes the jet velocity on the center-line. The lack of agreement downstream of this point is probably related to some inaccuracy in specifying the expansion rate of the vortex ring jet model.

Convergence Characteristics

The previous sections have been concerned with the individual nature and accuracy of the wing-flap and jet wake methods. Since the EBF pre-diction method is a combination of these two methods with iteration to obtain the mutual interference, it is of interest to examine the convergence characteristics for an EBF configuration. For this purpose, calculations were made on the four-engine configuration of references 13 and 16, which has a swept wing with a triple-slotted full-span flap system. The calculations were made with the computer program of refer-ence 4 using a given lattice arrangement and a circular cross section expanding jet (described in the following section). The initial assump-tion for the jet centerline in all cases is a straight line coincident with the engine centerline. Convergence characteristics were examined for total normal force, individual flap normal force, span-load distribution, and centerline position.

Convergence of the procedure for wing-flap normal-force coefficient is illustrated in figure 21. The normal-force coefficient from the first

iteration is approximately 50 percent larger than the results from the second iteration. After four full iterations, both curves, representing thrust coefficients of 2.3 and 4.0, have converged to within 7 percent. Additional iterations would produce more nearly converged results, but 7 percent was judged low enough to demonstrate convergence. The convergence pattern for normal-force coefficient is the same for this configuration at other angles of attack and for other similar configurations.

The convergence of the normal-force coefficient on each lifting surface of the wing-flap configuration is shown in figure 22. In this case, the normal force is defined to be normal to each individual component. Each component tends to converge according to its own pattern, but all components reach convergence at about the same rate. Flaps 2 and 3 have nearly identical convergence patterns because they have similar orientation to the jet wakes. The wing and flap 1, both with zero incidence, show a small effect of wake centerline deflection on their normal force because they are aligned parallel to the initial centerlines and small vertical motions of the centerlines have little effect on the induced velocity fields on these surfaces.

The convergence pattern of the spanwise distribution of normal force on each lifting surface is shown in figure 23. The wing normal-force distributions through four iterations are presented in figure 23(a). The peaks in the loading near $\eta = 0.25$ and 0.42 are caused by the engine wakes moving upward due to angle of attack and interfering directly on the aft portions of the wing. The normal-force distribution is nearly converged after two iterations as there are only small corrections produced by iterations three and four. The maximum normal-force coefficients at the peaks show the largest change between successive iterations, but these large loadings act on such a small portion of the wing that the total wing normal force is only slightly affected by the peak loadings.

Corresponding normal-force distributions on flaps 1, 2, and 3 are shown in figures 23(b), (c), and (d), respectively, for the four iterations. Flap 1 has high peak loadings similar to those on the wing which is not unexpected since flap 1 has zero deflection and can be looked at as simply an extension of the wing. The high peaks corresponding to the first iteration are caused by the edge of the jets hitting one row of control points. As the jet is bent down by the iteration procedure, the loading is reduced by the third iteration and has obviously converged after the fourth iteration with the peak loadings reduced considerably from their initial values.

Flap 2, with a deflection angle of 20°, is deflected into the center of the initially straight jet. Thus, the jet wakes are directly influencing a larger area of this flap than on the previous flap. This is illustrated by the width of the peak loading regions on flap 2. Each peak covers approximately 10 percent of the semispan of the flap. With each iteration, the jet is bent downward to approach the flap angle and the peak loadings are reduced, but the area of influence of the jets remains larger than on flap 1. As shown in figure 22, the total loading on flap 2 is much larger than that on flap 1.

The normal-force distribution on flap 3 after one iteration is quite different in character than the distribution observed on the other flaps. This loading has a single peak which is higher than that on any other flap. The single high peak is caused by the overlapping of the straight, expanding jets. The flap is deflected 40° into the center of the overlap region of the wakes where the total induced effects are nearly double those on preceding flaps, thus resulting in inordinately high local loadings. With iteration, the wakes are deflected downward such that the overlap region occurs beneath the flaps. This can be seen in the third and fourth iterations where the twin peak character of the flap loading has returned. The converged normal-force distribution on flap 3 has peaks which are broader but lower in maximum magnitude than those of flap 2 because the jets have expanded to a larger radius with the resultant lower jet velocities. Thus, flap 3 experiences lower jet induced velocities over a larger portion of the flap than the flaps upstream.

The convergence of the jet centerlines is shown in figures 24(a) and (b) for the inboard and outboard jets respectively. The initial jet boundary is also shown in these figures as it is superimposed on the wing-flap model. Note that the boundary is straight, indicating a linear expansion from the engine exit. The initial centerline used for the first iteration is straight as shown. The combination of the jet induced velocities, the wing-flap induced velocities, and the free stream produce the centerline, labeled as number 2, which is used for the second iteration. As was inferred from the loading distributions, convergence of the centerlines has been achieved by the fourth iteration. The final centerline calculation at the end of iteration 4 is denoted as centerline number 5 which, in each figure, is nearly the same as number 4. Thus, the fifth centerline is the converged centerline for each jet. The jet boundary can be placed on this centerline and the total flow field

calculated. Such a flow field is compared with a measured flow field in the next section concerning comparisons with data.

Lift and pitching-moment coefficients at two angles of attack, $\alpha = 6.5^\circ$ and 18.5°, are shown in figure 25 for each iteration to illustrate convergence of lift and pitching-moment curve. The values of lift coefficient used on these curves are for the wing and flap lifting surfaces only and do not include any lift components due to engine thrust, fuselage lift, or nacelle lift. Iteration 1 at each angle of attack was started with the same straight centerline jet model. The lift curve from the first iteration is nearly flat, indicating a very small effect of angle of attack. It is apparent that the jet induced effects overshadow all others when the centerlines are straight. At the end of the second iteration, the lift at $\alpha = 6.5^\circ$ is less than that at $\alpha = 18.5^\circ$. Iteration 2 also produces the greatest lift curve slope. The jet induced effects at the lower angle were reduced because the jet centerlines moved downward further from the lifting surface than did the same centerlines at the higher angle. This occurs because the higher angle of attack flow tends to keep the jet closer to the wing and flaps. Iterations 3 and 4 produce the same lift and moment curve slopes and the lift values at both angles of attack agree within approximately 7 percent. The converged jet centerlines calculated at $\alpha = 6.5^\circ$ were used for the initial centerlines for the $\alpha = 0^\circ$ calculation. In two iterations the solution had converged within 3 percent. The converged result at $\alpha = 0^\circ$ is also shown in figure 25.

The convergence results described above are typical of those observed on other EBF configurations. The method has never failed to converge, although convergence is slower for high flap angles. Generally, calculations have been initiated with a straight centerline because of simplicity, but obviously the number of iterations would be reduced if the initial centerline more closely approximated the final one. On the basis of cases run, the convergence is more rapid if the centerline approaches its converged position from above rather than below, because the correcting velocities causing the centerline position to change are larger if the centerline is too close to the wing-flap.

EBF Data

The overall EBF prediction method was evaluated by comparing predicted results with data on several typical EBF configurations. Ideally, one would like to have wing-flap-engine data on overall forces

and moments, loads on individual flap segments, pressure distributions, and jet wake velocity surveys. A large amount of data is available, but most of it is on complete configurations and consists only of overall force and moment coefficients. Thus, there are generally uncertainties due to force contributions from the fuselage, tail, nacelles, and leading-edge slats and to lack of direct knowledge of engine thrust. The results presented in this report attempt to account for these additional factors in the following manner.

Corrections.- The predicted aerodynamic characteristics obtained from the EBF method described in this report are for a wing-flap-jet configuration only. No fuselage, nacelle, or leading-edge slat effects are included. Results in reference 16 indicated that these effects are not negligible and should be included with the predictions to give meaningful comparisons with the data. Thus, the following corrections are made to the predictions.

The total lift coefficient is

$$C_L = C_{L_{WF}} + C_\mu \sin \alpha + C_{L_S} + C_{L_B} \tag{42}$$

where the first term is from the wing-flap vortex-lattice method with jet interference, and the second term is the component of total thrust in the lift direction. The last two terms in equation (42) are the combined lift of the leading-edge slat, the fuselage, and the nacelles. Typical values of these terms for the configuration under consideration are presented in Table III as a function of angle of attack and thrust coefficient. These were obtained in reference 16 from the difference between the total measured lift coefficients and the lift coefficients obtained from integration of the measured pressure distributions.

The total pitching-moment coefficient is

$$C_m = C_{m_{WF}} + C_{m_S} + C_{m_B} \tag{43}$$

where $C_{m_{WF}}$ is the result from the vortex-lattice prediction method. The value C_{m_S} is the pitching moment due to the force on the leading-edge slat and is estimated by integrating the section normal-force distributions in reference 16. These results are also shown in Table III. The value C_{m_B}, the pitching moment due to the fuselage and nacelles, is estimated using slender-body theory to be approximately

$$C_m \simeq 0.64\, \alpha \quad (\alpha \text{ in radians}) \tag{44}$$

Although the body contribution to pitching moment is small in magnitude compared to the wing-flap contribution, it can have an appreciable effect on the total moment curve. The moment center is such that there is no moment produced by the thrust of the engines.

The total (nonviscous) drag coefficient produced by the prediction method is

$$C_D = C_{D_{WF}} + C_{D_{ram}} - C_\mu \cos\alpha \tag{45}$$

where $C_{D_{WF}}$ is the induced drag coefficient calculated by the vortex-lattice method on the wing and flaps. The value $C_{D_{ram}}$ is the ram drag coefficient for the engines. This contribution is given in figure 4 of reference 13 for the particular configuration being considered. These results are reproduced in Table IV for convenience. The last term is the component of total thrust opposing the drag of the model and is included in the predictions to put them in the same form as the data. No estimate of viscous drag is included in the prediction method.

Data available.- The best data available for comparison purposes are that of references 13 and 16. Gross forces and moments and pressure distributions were obtained on a four-engine EBF configuration; thus, the individual loading distributions on each lifting surface are available. Because these data are unique, they will be used almost exclusively to evaluate the prediction method and the associated computer program.

The model is a large-scale, four-engine configuration with an aspect ratio 7.28 wing having a 25° swept quarter chord and a 0.4 taper ratio. High lift devices include full-span, triple-slotted, trailing-edge flaps and a leading-edge slat deflected 50°. Two flap deflections are considered for the full-span flap configuration: a take-off setting of 0°, 20°, and 40° for flaps 1, 2, and 3, respectively, and a landing setting of 15°, 35°, and 55°. The JT15D-1 engines are housed in nacelles mounted beneath the wing on pylons at the $\eta = 0.25$ and 0.42 semispan stations. Tests were run at gross thrust coefficients between 0 and 4.0. More detailed configuration data are available in reference 13.

Chordwise static pressure distributions at ten spanwise stations on each lifting surface are described in reference 16. Section normal-force

coefficients calculated from integrated pressure data on each lifting surface are presented in the same reference. These integrated pressure data are used for the following comparisons.

The vortex-lattice arrangement for the wing and flaps is shown in figure 26 where the flaps are shown undeflected so that the relative size of all the lattice elements can be compared. The lattice layout is based on the guidelines presented in Appendix A of reference 3, where possible. One change that is required by the deflected trailing-leg vortex-lattice method is that an equal number of spanwise elements be placed on each lifting surface and that all trailing legs be aligned with each other. The lattice shown in figure 26 is tailored for the two jet wakes at $\eta = 0.25$ and 0.42 and should be considered a "minimum" lattice for a four-engine wing-flap configuration of this complexity. The effect of changing the lattice layout is investigated later in this report.

A second set of data considered for comparison purposes is that for the four-engine EBF model of reference 17. This model has an aspect ratio 7, unswept, cambered wing with double-slotted, full-span trailing-edge flaps and a leading-edge slat deflected 55°. The model engines are cold-gas-turbine-driven fans which simulate the wake of high-bypass-ratio turbofan engines. The engines were mounted at 3° incidence to the wing root chord in order to direct their exhaust upward toward the lifting surfaces (position 4 in ref. 17). The leading-edge slat has a chord equal to 19 percent of the reference chord and is treated as a highly cambered portion of the wing. The two flaps have chords of 15 and 30 percent of the reference chord. This is the same configuration considered in the comparisons of reference 3.

Circular Jet Results

The jet wake model used in the initial calculations has a circular cross section over its entire length. The vortex cylinder strength, γ/V, is obtained from equations (28) and (29), and the expansion rate is determined from figure 11 which fixes the jet cross-sectional area aft of the last flap. A linear variation of wake radius is used to specify the jet growth between the engine exit position and the axial station defined by figure 11. The jet radius is extrapolated at the same expansion rate over the remainder of the length of the jet.

Take-off configuration.- The first configuration on which comparisons with data are made is the four-engine model with take-off flap setting

40

(δ_f = 0°/20°/40°) described in references 13 and 16. The jet turning efficiency was assumed to be 85 percent which limited the jet deflection angle to -34° for all calculations. The predictions to follow have all converged to within approximately 8-percent tolerance. The convergence is not the same at all angles of attack, which introduces a small uncertainty in the slope of the predicted curves.

In figure 27 the predicted section normal-force coefficients on flaps 1, 2, and 3 are compared with experimental results at C_μ = 4 and α = 18.5° obtained from reference 16. Wing data are not available for this configuration. The predicted values are from the fourth iteration described in figure 23. Figure 27(a) illustrates that the predicted peak loadings due to jet wake interference on flap 1 are greater than those measured and cover a smaller portion of the wing. The dip in the predicted loading between the jets is less than the measured values as is the predicted loading outboard of the second wake ($\eta > 0.45$). This indicates that the model jet has not expanded sufficiently at this station and perhaps should be expanded to a larger cross-sectional area. As noted on the figure, the predicted total normal-force coefficient on the single flap is approximately 30 percent higher than the value obtained by integrating the measured distribution.

The comparison in figure 27(b) for flap 2 shows the same pattern in that the predicted normal force in the vicinity of the engine wakes is much larger than the measured quantities with the result that the total force on the flap is overpredicted by nearly 40 percent.

The comparison for flap 3 in figure 27(c) shows good agreement between the predicted and measured loading distributions. The peak loadings, the width of the loading, and the total force on the flap are all in good agreement. Since this flap is nearest to the point at which the jet wake area is specified, based on measurements near a similar EBF configuration, the jet model is probably in better agreement with the actual jet on this flap than on the previous two flaps.

The predicted and measured longitudinal aerodynamic characteristics on the four-engine EBF model with take-off flap configuration are compared in figures 28(a) and (b). The predicted lift, pitching-moment, and drag results are obtained from equations (42), (43), and (45), respectively. The predicted power-off lift curve has the correct slope but is about 10 percent higher than the data. The corresponding pitching-moment curve

also has the correct slope, but the predicted results have a larger nose-down moment than the data. The predicted drag coefficient in figure 28(b) is slightly lower than the data as would be expected since viscous drag is not considered in the prediction method.

The lift coefficient curve in figure 28(a) for power-on, $C_\mu = 2.32$, is lower than the data, but the predicted slope is higher. It appears that the method is converging on a lift coefficient that is too low at low angles of attack. This result may be caused by the converged jet being too far beneath the lifting surfaces, a difficilty caused by estimating too high a value for jet turning efficiency. The predicted pitching-moment curve generally has too little nose-down moment in the region of low lift, indicating that the lost lift is aft of the moment center and most likely the lost lift should be on the flap surfaces. The drag curve shows very good agreement with the experimental results.

The predicted results in figure 28(a) corresponding to the highest thrust coefficient, $C_\mu = 3.95$, indicate the correct level of lift but a lift curve slope slightly higher than that measured. As the case for the lower thrust coefficient, the region which has the best agreement between measured and predicted lift coefficients also has best agreement for pitching-moment results. The drag coefficients are in fair agreement with the data.

Landing configuration.- The next set of experimental results used for comparison with predictions is on the same EBF model in a landing configuration with flaps 1, 2, and 3, deflected 15°, 35°, and 55°, respectively. In addition to overall force and moment coefficients, data are available on span-load distribution and chordwise pressure distributions from reference 16. The same vortex-lattice arrangement (shown in figure 26) was used for these calculations. As shown in reference 13, the static turning effectiveness of the jet acting on this configuration is approximately 0.70; therefore, the jet turning angle is limited to a maximum deflection of -38.5°.

The results to follow are all converged within approximately 11 percent. Most of these results are obtained from the fourth iteration of the solution, the same number of iterations used for the take-off configuration results. As discussed in those results, not all angles of attack are converged to the same tolerance; therefore, some uncertainty as to the slope of the predicted curves exists.

42

In figure 29, measured and predicted spanwise distribution of section normal-force coefficients are compared for the landing-flap configuration at 18.5° angle of attack. Two power settings, power off and C_μ = 2.3, are shown in this figure. Results on the wing, shown in figure 29(a), indicate that the predicted loading for power off is higher than was measured to the extent that the total predicted normal force is almost double the measured value. When the engines are operating, the predicted wing loading is in good agreement with experiment in the near vicinity of the engines; however, outboard of the engines ($\eta > 0.5$) the predicted results are too low. Integrating the two curves gives a predicted normal-force coefficient, on one wing panel, of 1.37 to be compared with the experimental result of 1.57.

Similar results on flap 1 are shown in figure 29(b). The predicted power-off loading distribution is again above that measured with the result that the total predicted normal force is much larger than the measured result. With power on, the predicted interference loading due to the inboard engine wake is higher than the measured value and covers a more narrow band of the wing than is illustrated by the measurements. The opposite situation is evident near the outboard engine; and outboard of the engines, the predicted loading is less than the measured results. The difference in levels of the predicted peak loadings near the two engine centerlines is due to small differences in the inboard and outboard jet centerline heights with respect to flap 1. This causes the jet induced velocities at the control points in line with the two centerlines to be different, thus producing quite different loadings.

Measured and predicted loading distributions on flaps 2 and 3 are shown in figure 29(c) and (d), respectively. The power-off results are similar to those on the previous flap. The predicted power-on loading curves on both flaps exhibit similar shapes, and on each flap, the loading around the engine centerlines is similar in shape and magnitude. The measured loadings on each flap show a larger interference effect from the outboard engine than from the inboard engine. The predicted total loading on each flap is in reasonable agreement with the measured result. As is the case on all flap surfaces, the predicted loading drops off more rapidly outboard of the mid-semispan than the measurements indicate.

Measured and predicted section normal-force coefficients on the same configuration at 18.5° angle of attack are compared in figure 30 for a high thrust setting, $C_\mu = 4$. The only difference in the theoretical model used for these results and the model used for the lower thrust setting in the previous figure is the jet model. The higher thrust jet has a higher jet exit velocity; consequently, the jet expands at a faster rate than the jet corresponding to $C_\mu = 2.3$.

The effect of the change in jet model is seen on the predicted results on the wing shown in figure 30(a). The predicted span loading on the wing has two loading peaks which are caused by the direct interference of the jet on the wing lifting-surface model. Similar peaks are not shown by the data. The differences between the measured and predicted loadings on the wing in the vicinity of the jet wakes will be discussed later in this section when chordwise pressure distributions are examined. The predicted loading on the outboard portion of the wing is again lower than measured results; however, the additional loading due to the peaks causes the predicted net normal force on the wing to be in good agreement with the value obtained from integration of the experimental curve.

The normal-force distributions on flap 1 are shown in figure 30(b) where the predicted peak loadings are again much larger than those measured. The peak attributed to the outboard jet is at $c_n \approx 34$ which is off the scale chosen for this figure.

Results on flap 2, figure 30(c), show good agreement for the loading induced by both the inboard and outboard jets, except that again the predicted loads drop more rapidly outboard of the outer jet than is indicated by the data. The total normal force on this flap is in good agreement with the value obtained from integration of the experimental curve.

The measured and predicted normal-force distributions on flap 3 are compared in figure 30(d). The measured results appear as on previous flaps, but the predicted results have a different appearance brought about by the lack of two well-defined areas of peak loading. This is caused by the meeting of the jet boundaries in the vicinity of the third flap. The expansion rates are such that the two jets come together near this flap causing the jet induced loading to be spread out over the entire interference region of the flap. The small dip occurring at

$\eta = 0.37$ is due to one of the two control points at this spanwise station falling just outside the boundary of the outboard jet, thus reducing the induced velocity field at this point.

Similar comparisons of the measured and predicted section normal-force coefficients on the EBF configuration of references 13 and 16 with the flaps deflected 15°, 35°, and 55° and a high thrust condition are presented in figure 31 for a lower angle of attack ($\alpha = 6.5^\circ$). The jet model is identical in strength and expansion rate to the model used for the previous figure, but the jet centerlines converge to different positions due to the change in angle of attack. The results have the same overall appearance as those in figure 30.

The chordwise distribution of pressure coefficients on the wing and flap surfaces at a semispan station aligned with the outboard engine are shown in figure 32. The data are shown as dashed curves with the long dashed portion of each curve representing the length over which measurements were made and the short dashed portion representing extrapolation to the trailing edge. Since the vortex-lattice method implies constant pressure on each lattice element, the theoretical pressure coefficients are shown as such. Too few chordwise lattice elements are used to permit a smooth cruve through predicted points. Notice that the jet induced loading on the aft quarter of the wing chord contributes all the additional loading which makes up the peak shown in figure 31(a). The absence of pressure taps on this part of the wing does not permit evaluation of the predicted pressure rise. The airfoil section in this region of the wing is distorted to provide for retraction of the flaps; therefore, it is unlikely that an idealized lifting-surface theory with no thickness effects included can adequately predict the detailed loading distribution in this region.

The measured and predicted longitudinal aerodynamic characteristics of the four-engine EBF model with landing flap configuration are compared in figure 33(a) and (b). The predicted results presented on this figure are corrected for the body, slat, and nacelle effects using the same information used to correct the take-off configuration results. These results are similar to those shown for the lower flap deflection angles in figure 28. The predicted power-off lift curve has the correct slope but is above the data. The power-on results are within 10 percent of the data over the angle of attack range shown ($0 \le \alpha \le 18.5^\circ$).

The pitching-moment results shown in figure 33 agree reasonably well. The inconsistent shape of the predicted curve at $c_\mu = 2.3$ may be due to differences in the degree of convergence of the calculations at different angles of attack, since the loading, particularly the pitching moment, is sensitive to small changes in wake position.

The drag results are shown in figure 33(b). The results are generally similar to those at the lower flap angle. One would expect best agreement at the higher thrust settings and negative drag values (small angles of attack), since the power effects are largest relative to viscous effects at these conditions. Such is the case, both with figures 33(b) and 28(b).

Flow fields.- The predicted flow field aft of the trailing edge of the last flap at a spanwise station corresponding to the centerline of the inboard jet is shown in figure 34. In figure 34(a), the final converged flow field at $\alpha = 6.5^\circ$ and $c_\mu = 3.95$ for the take-off flap configuration ($\delta_f = 0^\circ/20^\circ/40^\circ$) is shown. The uniformity of the jet flow characteristics of the vortex ring model is well illustrated. In the inset, a measured flow field aft of a similar EBF configuration under similar flow conditions is reproduced from reference 7. The measured flow field, also aligned with the centerline of the inboard jet, is very similar in magnitude and direction to the predicted flow field. The same type of comparison and results are shown in figure 34(b) for a lower thrust coefficient and higher angle of attack.

Lattice arrangement.- The effect of increasing the number of lattice elements representing the wing-flap configuration of references 13 and 16 has been investigated. Additional chordwise rows of vortices were added to each flap (fig. 26) so that flap 1 had two rows, and flaps 2 and 3 each had three rows of vortices. Results from a power-on calculation indicated less than 2-percent difference in the predicted aerodynamic coefficients. As anticipated from the conclusions of reference 3, increasing the number of lattice elements reduced the magnitudes of the predicted forces. Based on this investigation, it is felt that the lattice shown in figure 26 is probably a reasonable lattice for the particular configuration for force calculations. If more detailed pressure distributions are desired, one would want to increase the number of chordwise area elements. Guidelines for choosing a lattice layout for EBF configurations are presented in the program manual (ref. 4).

Unswept wing configuration.- The prediction method is next applied
to the rectangular wing, four-engine, EBF model of reference 17.
Comparisons of measured and predicted longitudinal aerodynamic character-
istics on this model with trailing-edge flaps deflected 17.5° and 35°
are shown in figure 35(a). The power-off predicted lift curve is approxi-
mately 10 percent above the data, but it has the correct slope. The
moment curve also has the correct slope, but too much nose-down moment
is predicted. The lift and moment curves are corrected for the force
and moment on the fuselage using slender-body theory. The predicted drag
curve, which includes no friction drag, is too low as would be expected.

The power-on comparisons shown in the same figure are for a gross
thrust coefficient of 5.5. For these predictions, the jet deflection
angle limit was taken as -22° from the static turning curves in refer-
ence 17. The comparisons between the measured and predicted results
show excellent agreement for both lift and pitching-moment curves, but
the predicted drag curve is again lower than the data. The predicted
lift and moment curves are corrected for the presence of the fuselage
with the same factors used in the power-off case. The lift and drag
curves are also corrected for thrust effects, and an estimate of the
engine ram drag coefficient is included in the predicted drag curve.

The same configuration with flaps deflected 27.5° and 55° is shown
in figure 35(b). The power-off lift is overpredicted by approximately
30 percent, but the lift curve slope is in good agreement with the experi-
mental value. The only explanation for the lift results is that there
may be some separation on the model with the large flap deflection. The
measured moment curve indicates a larger nose-up moment component than
the prediction. This is indicative of a loss of lift on the flaps.

When the engines are operating at a gross thrust coefficient of
5.5, the predicted results are approximately 10 percent beneath the data
at low angles of attack. The predicted lift curve slope is also higher
than the measured slope. The pitching moments are in reasonably good
agreement. The predicted results for the higher flap deflection were
obtained with the same engine wake model used for the previous figure,
but in this case, the jet deflection angle was limited to approximately
-38° as recommended by the static turning curves in reference 17. This
may be an overly optimistic turning efficiency, and a lower choice would
have the effect of raising the predicted lift curve in figure 35(b).

Elliptical Jet Results

The results presented thus far have all been obtained using a circular cross-sectional jet model. The effect of using an elliptical cross-section jet will now be examined on the four-engine EBF configuration with landing flap setting of references 13 and 16. The elliptic jet used for these calculations has the same momentum and the cross-sectional area distribution along the jet centerline as the circular jet. The elliptical jet is assumed to have an axis ratio of 2:1 at a point just aft of the trailing edge of the last flap. Since no data are available on the manner in which the jet axes change from circular to elliptical, a linear variation is chosen. The details of the specific elliptic cross-section jet used in the following calculations are presented in the program manual (ref. 4). In an effort to conserve computation time, the initial guess for the elliptic jet centerline is taken as the circular jet centerline two iterations before convergence. The elliptic jet calculation was carried out for two iterations; and all comparisons which follow are taken from the last iteration of both the circular jet and elliptic jet results. The same jet turning efficiency used in the previous circular jet calculations was used for the elliptic jet calculations.

The predicted section normal-force distributions corresponding to the circular jet and elliptic jet results are compared with experimental distributions in figure 36. The circular jet curves and the data are the same information shown in figure 30. The predicted loading on the wing under the influence of the elliptic jet is shown in figure 36(a). The interference loading due to the elliptic jet is less than the loading due to the circular jet. The major difference is the absence of the peak loadings which are caused by the circular jet moving up to contact the wing. The elliptic jet, in the vicinity of the wing trailing edge where the peak loadings were concentrated, has a smaller vertical height than the circular jet and it does not interfere directly on the wing. As shown on the figure, the total normal force on the wing under the influence of the elliptic jet is less than the measured result.

Similar loading comparisons on flap 1 are shown in figure 36(b). Again the elliptic jet interference is less than the circular jet results, and there is a large difference in the predicted distributions in the

region of the outboard jet ($\eta \approx 0.42$). The explanation for the differences between the two predicted loadings is that the elliptic jet, being of different shape, nearly misses the control points near $\eta = 0.42$ on this flap while the circular jet has a shape which results in direct interference on control points in this region. As was the case on the wing, the total normal force on flap 1 under the influence of the elliptic jet is less than the measured value.

The circular and elliptic jet results have a similar shape on flap 2 as shown in figure 36(c). The elliptic jet induced loading is less than the circular jet loading in the region near $\eta = 0.30$. This is again caused by the elliptic jet missing certain control points. However, the total results from both jets are in agreement with each other and the data.

An unusual predicted loading distribution is produced on flap 3 by the elliptic cross-section jet. The high peak loading at $\eta \simeq 0.34$ is caused by the overlapping of the inboard and outboard jets directly at one control point. This causes the loading on one area element to be double its usual level, thus resulting in an unrealistic loading distribution and a large net loading on this flap.

The above results indicate some large differences in local loadings due to a change in jet cross-sectional shape. Some of these differences are caused by the choice of the vortex-lattice arrangement. The same lattice was used for both calculations, and it is possible that the lattice could be optimized for an elliptic jet shape. For example, on flaps 1 and 2, several control points are just outside the boundary of the jet model; consequently, the entire lattice element is unaffected by the direct interference of the jet.

It is interesting to compare the total normal force on the complete wing-flap configuration for each jet shape. The normal-force coefficient on the circular jet configuration is 7.85, and that on the elliptic jet configuration is 7.69, a difference of only 2 percent. The loading is distributed differently over the wing and flap surfaces, but the total normal force imparted to the wing-flap configuration by the two jets is nearly the same. Since both the circular and elliptic jets had the same momentum and assumed turning efficiency, it can be concluded that similar total lifting-surface loading is required to turn the jets beneath the wing and flaps. The cross-sectional shape of the jet is

important if local loading and pressure distributions are required, but if gross aerodynamic forces are the goal of the calculation, the jet cross-sectional shape is not as important as the momentum and the entrainment of the jet model.

CONCLUDING REMARKS

An engineering prediction method has been developed to predict the loading distributions and longitudinal aerodynamic characteristics of externally blown flap configurations. Two potential flow models are combined for the method. The first is a vortex-lattice lifting-surface method capable of representing a wing of arbitrary sweep, taper, dihedral, camber, and twist with large multiple-slotted, partial or full-span flaps which can have large deflection angles. The second is a vortex ring model of a jet wake from a turbofan engine which represents the mass, momentum, and spreading of a turbulent jet with circular or elliptic cross section. It may be placed along a curved centerline. These models are combined in an iterative fashion to predict the loading on the wing and flaps in the presence of the jet wakes. The method yields chordwise pressure distributions and span-load distributions on each individual lifting surface and the total forces and moments on each surface. The method has the capability to compute flap hinge moments, but no results are presented in this report because of the lack of data for comparison purposes. Use of the method is restricted to the case of symmetry of the configuration about the vertical plane through the wing root chord.

The complete prediction method was applied to EBF configurations on which detailed aerodynamic data are available. The comparisons of measured and predicted gross lift, drag, and pitching-moment coefficients on configurations with moderate flap angles ($\delta_f \leq 40^\circ$) indicate generally good agreement for all thrust levels. This is felt to be due principally to the correct modeling of the entrainment and momentum characteristics of the engine wakes and to the proper treatment of the mutual interference between the jet wake and wing-flap. The interference model creates, on the wing-flap, both the momentum reaction due to jet deflection and the additional induced circulation characteristic of externally blown flap systems.

As the flap angles increase beyond 40°, the predicted results agree less well with the data for both swept and unswept wings. As was

50

indicated by the intermediate iteration solutions, the predicted loads are sensitive to centerline location. The assumption that the wing-flap induced interference on the jet affects only its centerline and not its boundary becomes less accurate as the jet is more highly deformed, and it is probable that this is responsible for the poorer agreement at the higher flap angles.

Comparisons of measured and predicted spanwise distributions of section normal force on each lifting surface indicate good quantitative agreement in some cases and poor agreement in other cases. Generally, the correct qualitative behavior is shown in which large peak loadings occur locally on the flaps due to direct impingement of the jet wakes, but the magnitude of the peaks is not consistently in agreement with the data. The differences are felt to be due to a combination of three factors: vortex-lattice arrangement, modeling of the velocity profile within the jet wake, and the boundary of the wake.

The distribution of loading on the wing and flap segments is sensitive to lattice layout, in that a control point may be just inside or outside the wake impingement region and have quite a different load on its panel than that of an adjacent panel. As the number of panels is increased, sensitivity of the total loading to the loading on individual panels decreases; therefore, the complete solution becomes less sensitive to lattice/jet location characteristics.

The jet wake model has the proper mass, momentum, and induced velocity field outside the jet, but a velocity profile inside the jet which is probably quite different than the EBF wake profile and certainly different than an axisymmetric jet profile. Since the wake induced detailed load distribution is determined by the wake velocity distribution, the use of a more realistic parabolic-type velocity profile inside the wake would affect the predicted flap load distribution.

Finally, the wake boundaries are limited at the present time to elliptical shapes centered around the wake centerline. This boundary shape is reasonable for the forward part of the wake, but when substantial interaction with the wing or flap occurs, the boundary will distort and influence the widths and heights of the peak induced loadings. At the present time, the method cannot handle more complex shapes.

The predicted pressure distributions on the lifting surfaces in the region of maximum jet interference show the correct general trends, but the use of only a small number of discrete constant pressure panels prevents the prediction of the details of the pressures. Power-off pressure distributions are generally predicted quite well.

The comparison of measured and predicted flow fields aft of EBF configurations show good similarity. Even though the two configurations are not the same, they have similar flap angles and identical thrust coefficients. The predicted flow field, corresponding to a converged solution, indicates similar flow angles and jet position beneath the wing as shown by the data.

The preceding comments generally indicate that the overall momentum reaction and jet induced circulation effects are properly modeled, but the details of the loading distribution are not consistently adequate, based on the one set of data available.

NIELSEN ENGINEERING & RESEARCH, INC.
    Mountain View, California
        November 1975

APPENDIX A

INDUCED VELOCITY FIELD DUE TO AN
ELLIPTIC CROSS-SECTION JET MODEL

The concept of circular vortex rings is described in reference 14. If the vorticity is allowed to lie along an elliptical shape, the result is what shall be termed herein as an elliptic vortex ring. The purpose of the following analysis is to determine the induced velocity field due to an elliptic vortex ring with constant vorticity and arbitrary eccentricity.

Consider an ellipse specified by the equation

$$\frac{y^2}{a^2} + \frac{z^2}{b^2} = 1 \tag{A-1}$$

and a field point P located at the point (x_o, y_o, z_o) as shown in figure 6. A system of confocal elliptic coordinates (ξ, η) is given by

$$\left. \begin{array}{l} y = c \cosh \xi \cos \eta \\ \\ z = c \sinh \xi \sin \eta \end{array} \right\} \tag{A-2}$$

where

$$c^2 = a^2 - b^2 \tag{A-3}$$

and is constant for all confocal ellipses. The semi-major and semi-minor axes, a and b, respectively, are given by

$$\left. \begin{array}{l} a = c \cosh \xi \\ \\ b = c \sinh \xi \end{array} \right\} \tag{A-4}$$

Therefore, from (A-2)

$$\left. \begin{array}{l} \frac{y}{a} = \cos \eta \\ \\ \frac{z}{b} = \sin \eta \end{array} \right\} \tag{A-5}$$

APPENDIX A

Note that constant values of ξ correspond to ellipses in which the distance between the foci is $2c$, and constant values of η correspond to hyperbolas confocal with one another and with the ellipses. Thus, ξ_O and η_O represent the ellipse and hyperbola through the point (x_O, y_O, z_O) and can be called the elliptic coordinates of P.

Differential Induced Velocity Components

The general formula for the induced velocity components at $P(x_O, y_O, z_O)$ due to a line segment of length ds and circulation Γ is given by the Biot-Savart law as

$$\overrightarrow{dv} = \frac{\Gamma \, ds}{4\pi R^3} \, (\overrightarrow{s} \times \overrightarrow{R}) \tag{A-6}$$

where

$\overrightarrow{R}$ = vector from ds to P

$\overrightarrow{s}$ = unit vector tangent to line segment; positive direction corresponds to direction of $\overrightarrow{\Gamma}$

Assume the line segment ds to be in the plane $x = 0$. Therefore,

$$\overrightarrow{R} = (x_O)\overrightarrow{i} + (y_O - y)\overrightarrow{j} + (z_O - z)\overrightarrow{k} \tag{A-7}$$

and

$$\overrightarrow{s} \, ds = dy \, \overrightarrow{j} + dz \, \overrightarrow{k} \tag{A-8}$$

where dy and dz lie on the ellipse described by equation (A-5). Equation (A-8) can be written as

$$\overrightarrow{s} \, ds = \overrightarrow{ds} = -a \sin \eta \, d\eta \, \overrightarrow{j} + b \cos \eta \, d\eta \, \overrightarrow{k} \tag{A-9}$$

Consider the confocal elliptic coordinates of P to be

$$\left.\begin{array}{l} y_O = a_O \cos \eta_O \\[2mm] z_O = b_O \sin \eta_O \end{array}\right\} \tag{A-10}$$

The cross product in equation (A-6) can be carried out as follows.

$$ds(\vec{s} \times \vec{R}) = d\vec{s} \times \vec{R} = \begin{vmatrix} \vec{i} & \vec{j} & \vec{k} \\ 0 & -a \sin \eta & b \cos \eta \\ x_o & y_o - y & z_o - z \end{vmatrix}$$

$$= (ab - ab_o \sin \eta_o \sin \eta - a_o b \cos \eta_o \cos \eta) d\eta \; \vec{i}$$

$$+ (bz_o \cos \eta \; d\eta)\vec{j} + (az_o \sin \eta \; d\eta)\vec{k} \qquad (A-11)$$

From (A-6) we can now write the three components of the induced velocity in differential form.

$$dv_x = \frac{\Gamma}{4\pi} \frac{(ab - ab_o \sin \eta_o \sin \eta - a_o b \cos \eta_o \cos \eta) d\eta}{R^3} \qquad (A-12)$$

$$dv_y = \frac{\Gamma}{4\pi} \frac{bx_o \cos \eta \; d\eta}{R^3} \qquad (A-13)$$

$$dv_z = \frac{\Gamma}{4\pi} \frac{ax_o \sin \eta \; d\eta}{R^3} \qquad (A-14)$$

The radial distance R is obtained from (A-7)

$$R^2 = (x_o)^2 + (a_o \cos \eta_o - a \cos \eta)^2 + (b_o \sin \eta_o - b \sin \eta)^2 \qquad (A-15)$$

Induced Velocity Components Due to First Quadrant of Elliptical Vortex Ring

Equations (A-12), (A-13), and (A-14) can be integrated over the first quadrant of the ellipse to obtain the portion of the induced velocities due to that part of the vortex ring. A variable change from η to t is made in accordance with the following transformation suggested in reference 18.

$$\left. \begin{array}{ll} t = \tan \dfrac{\eta}{2} & d\eta = \dfrac{2}{1 + t^2} \; dt \\[3mm] \cos \eta = \dfrac{1 - t^2}{1 + t^2} & \sin \eta = \dfrac{2t}{1 + t^2} \end{array} \right\} \qquad (A-16)$$

APPENDIX A

Expanding R^2 in equation (A-15) results in

$$R^2 = \frac{1}{(1 + t^2)^2} \left\{ t^4 \left[c^2 \cos^2 \eta_0 + b^2 + b_0^2 + x_0^2 + 2a\, a_0 \cos \eta_0 + c^2 \right] \right.$$

$$+ t^3 \left[-4b\, b_0 \sin \eta_0 \right] + t^2 \left[2(c^2 \cos^2 \eta_0 + b^2 + b_0^2 + x_0^2 - c^2) \right]$$

$$\left. + t \left[-4b\, b_0 \sin \eta_0 \right] + \left[c^2 \cos^2 \eta_0 + b^2 + b_0^2 + x_0^2 - 2a\, a_0 \cos \eta_0 + c^2 \right] \right\}$$

(A-17)

Equation (A-17) can be rewritten as

$$R^2 = \frac{Q}{(1 + t^2)^2} \left[t^4 + \lambda_3 t^3 + \lambda_2 t^2 + \lambda_1 t + \lambda_0 \right]$$

(A-18)

where

$$Q = c^2 \cos^2 \eta_0 + b^2 + b_0^2 + x_0^2 + 2a\, a_0 \cos \eta_0 + c^2$$

(A-19)

and

$$\lambda_0 = \frac{c^2 \cos^2 \eta_0 + b^2 + b_0^2 + x_0^2 - 2a\, a_0 \cos \eta_0 + c^2}{Q}$$

$$\lambda_1 = \frac{-4b\, b_0 \sin \eta_0}{Q}$$

$$\lambda_2 = \frac{2(c^2 \cos^2 \eta_0 + b^2 + b_0^2 + x_0^2 - c^2)}{Q}$$

$$\lambda_3 = \lambda_1$$

(A-20)

From equations (A-12), (A-13), and (A-14),

$$dv_x = \frac{\Gamma}{2\pi Q^{3/2}} \frac{(1 + t^2)}{\left[t^4 + \lambda_3 t^3 + \lambda_2 t^2 + \lambda_1 t + \lambda_0 \right]^{3/2}} \left[t^2 (ab + a_0 b \cos \eta_0) \right.$$

$$\left. + t(-2ab_0 \sin \eta_0) + (ab - a_0 b \cos \eta_0) \right]$$

(A-21)

56

$$dv_y = \frac{\Gamma}{2\pi Q^{3/2}} \frac{bx_0(1 - t^2)(1 + t^2)}{\left[t^4 + \lambda_3 t^3 + \lambda_2 t^2 + \lambda_1 t + \lambda_0\right]^{3/2}} dt \qquad (A-22)$$

$$dv_z = \frac{\Gamma}{2\pi Q^{3/2}} \frac{ax_0 t(1 + t^2)}{\left[t^4 + \lambda_3 t^3 + \lambda_2 t^2 + \lambda_1 t + \lambda_0\right]^{3/2}} \qquad (A-23)$$

The limits of integration for the above velocity components are obtained from equation (A-5). The lower limit at $y = a$, $z = 0$ corresponds to $\eta = 0$ which gives $t = 0$ from (A-16). The upper limit at $y = 0$, $z = b$ corresponds to $\eta = \pi/2$ and $t = 1$. Now define a set of integrals $J_0, J_1, \ldots, J_4$ to be

$$J_n = \int_0^1 \frac{t^n dt}{\left[t^4 + \lambda_3 t^3 + \lambda_2 t^2 + \lambda_1 t + \lambda_0\right]^{3/2}} \qquad (A-24)$$

The velocity components from (A-21), (A-22), and (A-23) become

$$v_x = \frac{\Gamma}{2\pi Q^{3/2}} \Big[(ab + a_0 b \cos \eta_0)J_4 - (2ab_0 \sin \eta_0)J_3$$

$$+ 2ab\, J_2 - (2ab_0 \sin \eta_0)J_1 + (ab - a_0 b \cos \eta_0)J_0\Big] \qquad (A-25)$$

$$v_y = \frac{\Gamma bx_0}{2\pi Q^{3/2}} (J_0 - J_4) \qquad (A-26)$$

$$v_z = \frac{\Gamma ax_0}{\pi Q^{3/2}} (J_1 + J_3) \qquad (A-27)$$

These velocity components are those induced by the first quadrant of the elliptic vortex ring. Details of the evaluation of the J integrals in equation (A-24) are presented in Appendix B.

Induced Velocity Components Due to Complete Vortex Ring

The velocity components induced by the four quadrants of an elliptic vortex ring are obtained from equations (A-25), (A-26), and (A-27) through an appropriate change in the coordinate system and a corresponding change in the sign of the resulting velocity component. Thus, the four components of the x velocity are

$$\left. v_x \right|_I = v_x \quad \text{at} \quad (x_o, y_o, z_o)$$

$$\left. v_x \right|_{II} = v_x \quad \text{at} \quad (x_o, -y_o, z_o)$$

$$\left. v_x \right|_{III} = v_x \quad \text{at} \quad (x_o, -y_o, -z_o) \qquad\qquad \text{(A-28)}$$

$$\left. v_x \right|_{IV} = v_x \quad \text{at} \quad (x_o, y_o, -z_o)$$

where the subscripts I, II, III, and IV correspond to the particular quadrant of the vortex ring and v_x is computed from equation (A-25) at the noted coordinates.

The y velocity components are

$$\left. v_y \right|_I = v_y \quad \text{at} \quad (x_o, y_o, z_o)$$

$$\left. v_y \right|_{II} = v_y \quad \text{at} \quad (x_o, -y_o, z_o)$$

$$\left. v_y \right|_{III} = v_y \quad \text{at} \quad (x_o, -y_o, -z_o) \qquad\qquad \text{(A-29)}$$

$$\left. v_y \right|_{IV} = v_y \quad \text{at} \quad (x_o, y_o, -z_o)$$

where v_y is computed from equation (A-26) at the noted coordinates.

In the same fashion, the z velocity components are computed from equation (A-27).

$$\left. v_z \right|_I = v_z \quad \text{at} \quad (x_o, y_o, z_o)$$

$$\left. v_z \right|_{II} = v_z \quad \text{at} \quad (x_o, -y_o, z_o)$$

$$\left. v_z \right|_{III} = v_z \quad \text{at} \quad (x_o, -y_o, -z_o) \qquad\qquad \text{(A-30)}$$

$$\left. v_z \right|_{IV} = v_z \quad \text{at} \quad (x_o, y_o, -z_o)$$

Each component of induced velocity at (x_0, y_0, z_0) from a single ring is the sum of the contributions from the four quadrants. Some induced velocities from a family of elliptic rings with various axis ratios are presented in the results section of this report.

Velocities Induced by Complete Jet Model

The jet-wake model is made up of a series of vortex rings with their axes lying along the prescribed centerline of the jet as shown in figure 7. If the jet is deflected spanwise under the wing, as shown in the top view of figure 7, the rings are assumed not to tilt by the centerline deflection angle, σ. However, for vertical deflection, which is generally much larger, the rings tilt by the local angle θ, as shown in the lower view of figure 7. As the jet centerline is deflected, the orientation of a field point P with respect to a vortex ring changes with the ring position along the centerline. Since the jet induced velocities on the wing are required for interference calculations, the following set of equations transforms the induced velocities from the ring coordinate system to the wing system.

The coordinates of P in the jet centered coordinate system are:

$$\left.\begin{array}{l} x_{j_P} = -X_P + X_Q \\[2mm] y_{j_P} = Y_P - Y_Q \\[2mm] z_{j_P} = -Z_P + Z_Q \end{array}\right\} \tag{A-31}$$

where point Q denotes the center of the origin of the jet. Transforming (A-31) one step further, the coordinates of P in a ring centered coordinate system are

$$\left.\begin{array}{l} x_P = (x_{j_P} - x_{j_S})\cos\theta + (z_{j_P} - z_{j_S})\sin\theta \\[2mm] y_P = (y_{j_P} - y_{j_S}) \\[2mm] z_P = -(x_{j_P} - x_{j_S})\sin\theta + (z_{j_P} - z_{j_S})\cos\theta \end{array}\right\} \tag{A-32}$$

where the point S denotes the location of the center of a particular vortex ring.

The three components of induced velocity in the ring system, v_x, v_y, and v_z, are obtained by summing the four parts of each component as noted in equations (A-28), (A-29), and (A-30), respectively. These velocity components, when resolved into components in the jet coordinate system, become

$$\left.\begin{array}{l} u_j = v_x \cos\theta - v_z \sin\theta \\[2ex] v_j = v_y \\[2ex] w_j = v_x \sin\theta + v_z \cos\theta \end{array}\right\} \quad \text{(A-33)}$$

The induced velocities in the wing coordinate system are:

$$\left.\begin{array}{l} u = -u_j \\[2ex] v = v_j \\[2ex] w = -w_j \end{array}\right\} \quad \text{(A-34)}$$

The total velocity induced at P by the entire jet-wake model is obtained by summing the velocities induced by all the rings forming the wake.

EVALUATION OF J_n INTEGRALS FOR
AN ELLIPTIC VORTEX RING

The set of integrals

$$J_n = \int_0^1 \frac{t^n dt}{\left[t^4 + \lambda_3 t^3 + \lambda_2 t^2 + \lambda_1 t + \lambda_0\right]^{3/2}} \tag{B-1}$$

appearing in equations (A-25), (A-26), and (A-27) need to be solved analytically in order to calculate the induced velocity components due to an elliptic vortex ring.

The general solution of a quartic equation can be written as

$$t^4 + \lambda_3 t^3 + \lambda_2 t^2 + \lambda_1 t + \lambda_0 = (t - \alpha)(t - \bar{\alpha})(t - \beta)(t - \bar{\beta})$$

$$= \left[(t - b_1)^2 + a_1^2\right]\left[(t - b_2)^2 + a_2^2\right] \tag{B-2}$$

where

$$\left.\begin{array}{ll} \alpha = b_1 + ia_1, & \bar{\alpha} = b_1 - ia_1 \\[2mm] \beta = b_2 + ia_2, & \bar{\beta} = b_2 - ia_2 \end{array}\right\} \tag{B-3}$$

The variable t in equation (B-2) is replaced by υ using the transformation

$$tn\, u = \frac{t - b_1 + a_1 g_1}{a_1 + b_1 g_1 - g_1 t} \tag{B-4}$$

from page 146 of reference 18. The constants in equation (B-4) are defined as follows.

$$\left.\begin{array}{ll} b_1 = \dfrac{\alpha + \bar{\alpha}}{2} & a_1^2 = -\dfrac{(\alpha - \bar{\alpha})^2}{4} \\[4mm] b_2 = \dfrac{\beta + \bar{\beta}}{2} & a_2^2 = -\dfrac{(\beta - \bar{\beta})^2}{4} \\[4mm] & g_1^2 = \dfrac{4a_1^2 - (A - B)^2}{(A + B)^2 - 4a_1^2} \end{array}\right\}$$

APPENDIX B

$$A^2 = (b_1 - b_2)^2 + (a_1 + a_2)^2 \left.\vphantom{\int}\right\} \qquad \text{(B-5)}$$

$$\text{(concluded)}$$

$$B^2 = (b_1 - b_2)^2 + (a_1 - a_2)^2 .$$

From (B-4)

$$t = \frac{(a_1 + g_1 b_1)\,\text{tn}\ u + b_1 - a_1 g_1}{1 + g_1\,\text{tn}\ u} \qquad \text{(B-6)}$$

which can be differentiated to give

$$dt = \frac{a_1(1 + g_1^2)}{(1 + g_1\,\text{tn}\ u)^2}\ \frac{\text{dn}\ u}{\text{cn}^2 u}\ du \qquad \text{(B-7)}$$

Page 146 of reference 18 provides the relation

$$\frac{dt}{\left[(t - \alpha)(t - \overline{\alpha})(t - \beta)(t - \overline{\beta})\right]^{1/2}} = g\ du \qquad \text{(B-8)}$$

where

$$u = \int_0^\phi \frac{d\phi}{\sqrt{1 - k^2\sin^2\phi}} = F(\phi, k) \qquad \text{(B-9)}$$

and

$$g = \frac{2}{A + B} \left.\vphantom{\int}\right\}$$

$$\qquad\qquad\qquad\qquad \text{(B-10)}$$

$$k^2 = \frac{4AB}{(A + B)^2}$$

Substituting equation (B-6) into the first term of (B-2) results in the following:

$$(t - b_1)^2 + a_1^2 = \frac{a_1^2(1 + g_1^2)(1 + \text{tn}^2 u)}{(1 + g_1\,\text{tn}\ u)^2} \qquad \text{(B-11)}$$

62

Therefore,

$$\frac{1}{(t - \alpha)(t - \bar{\alpha})} = \frac{(1 + g_1 tn\ u)^2}{a_1^2(1 + g_1^2)(1 + tn^2 u)} \qquad (B-12)$$

Applying the same substitution to the second term of equation (B-2) does not result in a simple relationship like equation (B-11). The second term becomes

$$(1 + g_1 tn\ u)^2 \left[(t - b_2)^2 + a_2^2 \right] = \left[(a_1 + b_1 g_1)^2 - 2b_2 g_1(a_1 + g_1 b_1) \right.$$

$$+ g_1^2(a_2^2 + b_2^2) \Big] tn^2 u$$

$$+ 2 \Big[(a_1 + g_1 b_1)(b_1 - a_1 g_1) - b_2(a_1 + b_1 g_1)$$

$$- b_2 g_1(b_1 - a_1 g_1) + g_1(a_2^2 + b_2^2) \Big] tn\ u$$

$$+ \Big[(b_1 - a_1 g_1)^2 - 2b_2(b_1 - a_1 g_1)$$

$$+ (a_2^2 + b_2^2) \Big] \qquad (B-13)$$

Assuming that (B-13) has the same form as (B-11), the coefficient of the tn u term of (B-13) must be zero. This coefficient can be written as

$$a_1(b_2 - b_1)g^2 + \Big[(b_1 - b_2)^2 + (a_2^2 - a_1^2) \Big] g_1 + a_1(b_1 - b_2) = 0 \qquad (B-14)$$

which is a quadratic in g_1. Therefore,

$$g_1 = \frac{-\Big[(b_1 - b_2)^2 + (a_2^2 - a_1^2) \Big] \pm \sqrt{\Big[(b_1 - b_2)^2 + (a_2^2 - a_1^2) \Big]^2 + 4a_1^2(b_2 - b_1)^2}}{2a_1(b_2 - b_1)}$$

$$(B-15)$$

which can be rewritten in a general form and simplified as follows

$$g_1 = \frac{-R + \sqrt{R^2 + Q^2}}{Q} \times \frac{-R \mp \sqrt{R^2 + Q^2}}{-R \mp \sqrt{R^2 + Q^2}}$$

$$= \frac{-Q}{-R \mp \sqrt{R^2 + Q^2}} \tag{B-16}$$

Multiplying (B-15) by (B-16) results in an expression for g_1^2.

$$g_1^2 = \frac{\left[(b_1 - b_2)^2 + (a_2^2 - a_1^2)\right] \mp \sqrt{\left[(b_2 - b_1)^2 + (a_2^2 - a_1^2)\right]^2 + 4a_1^2(b_2 - b_1)^2}}{-\left[(b_1 - b_2)^2 + (a_2^2 - a_1^2)\right] \mp \sqrt{\left[(b_2 - b_1)^2 + (a_2^2 - a_1^2)\right]^2 + 4a_1^2(b_2 - b_1)^2}} \tag{B-17}$$

Substituting the relations for A^2 and B^2 from equation (B-5) into (B-17) and using the upper sign of the square root terms results in

$$g_1^2 = \frac{4a_1^2 - (A - B)^2}{(A + B)^2 - 4a_1^2} \tag{B-18}$$

which is identical to the relationship in equation (A-5). Thus, equation (B-13) becomes

$$(1 + g_1 \,\text{tn}\, u)^2 \left[(t - b_2)^2 + a_2^2\right] = \left[(a_1 + b_1 g_1)^2 - 2b_2 g_1 (a_1 + b_1 g_1)\right.$$

$$\left. + g_1^2 (a_2^2 + b_2^2)\right] \text{tn}^2 u$$

$$+ \left[(b_1 - a_1 g_1)^2 - 2b_2 (b_1 - a_1 g_1)\right.$$

$$\left. + (a_2^2 + b_2^2)\right] \tag{B-19}$$

A great deal of effort was expended to get the right-hand side of this equation into the same form as the numerator of equation (B-12), but with no success. An alternate approach follows.

Substituting equation (B-7) into (B-8) results in

$$g = \frac{a_1(1 + g_1^2)}{(1 + g_1 \tan u)^2} \frac{dn\ u}{cn^2 u} \frac{1}{\sqrt{[(t - b_1)^2 + a_1^2][(t - b_2)^2 + a_2^2]}} \tag{B-20}$$

or

$$[(t - b_1)^2 + a_1^2][(t - b_2)^2 + a_2^2] = \left(\frac{a_1}{g}\right)^2 \frac{(1 + g_1^2)^2}{(1 + g \tan u)^4} \frac{dn^2 u}{cn^4 u} \tag{B-21}$$

It can be shown that

$$\frac{dn^2 u}{cn^4 u} = (1 + tn^2 u)(1 + k'^2 tn^2 u) \tag{B-22}$$

where

$$k'^2 = 1 - k^2$$

Equation (B-21) becomes

$$[(t - b_1)^2 + a_1^2][(t - b_2)^2 + a_2^2] = \frac{a_1^2(1 + g_1^2)^2}{g^2(1 + g_1 \tan u)^4}(1 + tn^2 u)(1 + k'^2 tn^2 u) \tag{B-23}$$

Removing the identity in (B-11) from this result produces the required relationship for the second term.

$$[(t - b_2)^2 + a_2^2] = \frac{(1 + g_1^2)(1 + k'^2 tn^2 u)}{g^2(1 + g_1 \tan u)^2} \tag{B-24}$$

Substituting equation (B-2) into (B-1) and letting $n = 0$, the integral for J_0 becomes

$$J_0 = \int_0^1 \frac{dt}{\{[(t - b_1)^2][(t - b_2)^2 + a_2^2]\}^{3/2}} \tag{B-25}$$

APPENDIX B

Substituting equation (B-8) and (B-23) into (B-25) results in

$$J_o = \frac{g^3}{a_1^2(1 + g_1^2)^2} \int_{u_L}^{u_U} \frac{(1 + g_1 \tn u)^4}{(1 + \tn^2 u)(1 + k'^2 \tn^2 u)} \, du \qquad (B-26)$$

where the lower and upper limits are obtained from equation (B-4).

$$\left.\begin{array}{ll} (t = 0) & \tn u_L = \dfrac{-b_1 + a_1 g_1}{a_1 + b_1 g_1} \\[3mm] (t = 1) & \tn u_U = \dfrac{1 - b_1 + a_1 g_1}{a_1 + b_1 g_1 - g_1} \end{array}\right\} \qquad (B-27)$$

The following relations are obtained from reference 18.

$$\left.\begin{array}{l} 1 + \tn^2 u = \dfrac{1}{\cn^2 u} \\[4mm] 1 + k'^2 \tn^2 u = \left(\dfrac{\dn u}{\cn u}\right)^2 \end{array}\right\} \qquad (B-28)$$

Substituting equation (B-28) into (B-26) gives

$$J_o = \frac{g^3}{a_1^2(1 + g_1^2)^2} \int_{u_L}^{u_U} (1 + g_1 \tn u)^4 \frac{\cn u}{\dn^2 u} \, du$$

$$= \frac{g^3}{a_1^2(1 + g_1^2)^2} \int_{u_L}^{u_U} (\cn u + g_1 \sn u)^4 \frac{1}{\dn^2 u} \, du \qquad (B-29)$$

which, when expanded, results in the following integrals.

$$\Lambda_o = \int_{u_L}^{u_U} \frac{\sn^4 u}{\dn^2 u} \, du$$

$$= \frac{1}{k'^2 k^4} \left[(1 + k'^2) E(u) - 2k'^2 u - k^2 (\sn u)(\cd u) \right]_{u_L}^{u_U} \qquad (B-30)$$

66

$$\Lambda_1 = \int_{u_L}^{u_U} \frac{cn\ u\ sn^3 u}{dn^2 u}\ du$$

$$= \frac{1}{k^4} \left[dn\ u + \frac{1}{dn\ u} \right]_{u_L}^{u_U} \tag{B-31}$$

$$\Lambda_2 = \int_{u_L}^{u_U} \frac{cn^2 u\ sn^2 u}{dn^2 u}\ dn$$

$$= \frac{1}{k^4} \left[(1 + k'^2)u - 2E(u) + k^2 (sn\ u)(cd\ u) \right]_{u_L}^{u_U} \tag{B-32}$$

$$\Lambda_3 = \int_{u_L}^{u_U} \frac{cn^3 u\ sn\ u}{dn^2 u}\ du$$

$$= \frac{-1}{k^4} \left[dn\ u + \frac{k'^2}{dn\ u} \right]_{u_L}^{u_U} \tag{B-33}$$

$$\Lambda_4 = \int_{u_L}^{u_U} \frac{cn^4 u}{dn^2 u}\ du$$

$$= \frac{1}{k^4} \left[-2k'^2 u + (1 + k'^2)E(u) - k^2 k'^2 (sn\ u)(cd\ u) \right]_{u_L}^{u_U} \tag{B-34}$$

where

$$\left. \begin{array}{l} u = F(\phi, k) \\[6pt] E(u) = E(\phi, k) \\[6pt] sn\ u = \sin \phi \\[6pt] cn\ u = \cos \phi \end{array} \right\} \tag{B-35}$$

67

APPENDIX B

Finally,

$$J_o = \frac{g^3}{a_1^2 (1 + g_1^2)^2} \left[\Lambda_4 + 4g_1 \Lambda_3 + 6g_1^2 \Lambda_2 + 4g_1^3 \Lambda_1 + g_1^4 \Lambda_o \right] \qquad (B-36)$$

When $n = 1$ in equation (B-1),

$$J_1 = \int_0^1 \frac{t\ dt}{\left\{ \left[(t - b_1)^2 + a_1^2 \right] \left[(t - b_2)^2 + a_2^2 \right] \right\}^{3/2}} \qquad (B-37)$$

which can be simplified in the same manner described above for J_o. Therefore,

$$J_1 = \frac{g^3}{a_1^2 (1 + g_1^2)^2} \int_{u_L}^{u_U} (1 + g_1 \tn u)^3 \left[(a_1 + b_1 g_1) \tn u + (b_1 - a_1 g_1) \right] \frac{\cn^4 u}{\dn^2 u}\ du$$

$$= \frac{g^3 (b_1 - a_1 g_1)}{a_1^2 (1 + g_1^2)^2} \int_{u_L}^{u_U} (\cn u + g_1 \sn u)^3 (\cn u + \tau \sn u) \frac{1}{\dn^2 u}\ du \qquad (B-38)$$

where

$$\tau = \frac{a_1 + b_1 g_1}{b_1 - a_1 g_1} \qquad (B-39)$$

Making use of the Λ_n integrals in equations (B-30) through (B-34), equation (B-38) can be written as follows.

$$J_1 = \frac{g^3 (b_1 - a_1 g_1)}{a_1^2 (1 + g_1^2)^2} \left[\Lambda_4 + (3g_1 + \tau) \Lambda_3 + 3g_1 (g_1 + \tau) \Lambda_2 + g_1^2 (g_1 + 3\tau) \Lambda_1 \right.$$

$$\left. + g_1^3 \tau \Lambda_o \right] \qquad (B-40)$$

Similarly,

$$J_2 = \frac{g^3 (b_1 - a_1 g_1)^2}{a_1^2 (1 + g_1^2)^2} \left[\Lambda_4 + 2(g_1 + \tau) \Lambda_3 + (g_1^2 + 4\tau g_1 + \tau^2) \Lambda_2 \right.$$

$$\left. + 2\tau g_1 (g_1 + \tau) \Lambda_1 + \tau^2 g_1^2 \Lambda_o \right] \qquad (B-41)$$

68

$$J_3 = \frac{g^3(b_1 - a_1 g_1)^3}{a_1^2(1 + g_1^2)^2} \left[\Lambda_4 + (3\tau + g_1)\Lambda_3 + 3\tau(g_1 + \tau)\Lambda_2 \right.$$

$$\left. + \tau^2(\tau + 3g_1)\Lambda_1 + \tau^3 g_1 \Lambda_0 \right] \tag{B-42}$$

$$J_4 = \frac{g^3(b_1 - a_1 g_1)^4}{a_1^2(1 + g_1^2)^2} \left[\Lambda_4 + 4\tau\Lambda_3 + 6\tau^2\Lambda_2 + 4\tau^3\Lambda_1 + \tau^4\Lambda_0 \right] \tag{B-43}$$

REFERENCES

1. Lopez, M. L. and Shen, C. C.: Recent Developments in Jet Flap Theory and Its Application to STOL Aerodynamic Analysis. AIAA Paper No. 71-578, June 1971.

2. Shollenberger, C. A.: A Three-Dimensional Wing/Jet Interaction Analysis Including Jet Distortion Influences. AIAA Paper No. 73-655, July 1973.

3. Dillenius, M. F. E., Mendenhall, M. R., and Spangler, S. B.: Calculation of the Longitudinal Aerodynamic Characteristics of STOL Aircraft with Externally-Blown Jet-Augmented Flaps. NASA CR-2358, Feb. 1974.

4. Mendenhall, M. R., Goodwin, F. K., and Spangler, S. B.: A Computer Program to Calculate the Longitudinal Aerodynamic Characteristics of Wing-Flap Configurations with Externally Blown Flaps. NASA CR-2706, 1976.

5. Mendenhall, M. R., Perkins, S. C., Jr., Goodwin, F. K., and Spangler, S. B.: Calculation of Static Longitudinal Aerodynamic Characteristics of STOL Aircraft with Upper-Surface-Blown Flaps. NASA CR-137646, Apr. 1975.

6. Rubbert, P. E.: Theoretical Characteristics of Arbitrary Wings by a Non-Planar Vortex Lattice Method. Boeing Rept. D6-9244, Feb. 1964.

7. Johnson, W. G., Jr. and Kardas, G. E.: A Wind-Tunnel Investigation of the Wake Near the Trailing Edge of a Deflected Externally Blown Flap. NASA TM X-3079, Oct. 1974.

8. Sforza, P. M., Steiger, M. H., and Trentacoste, N.: Studies on Three-Dimensional Viscous Jets. AIAA Jour., vol. 4, no. 5, May 1966, p. 800.

9. Trentacoste, N. and Sforza, P.: Further Experimental Results for Three-Dimensional Free Jets. AIAA Jour., vol. 5, no. 5, May 1967, p. 885.

10. Abramovich, G. N.: The Theory of Turbulent Jets. MIT Press, 1963.

11. Carter, A. W.: Pressure Distributions on a Wing Having NACA 4415 Airfoil Sections with Trailing-Edge Flaps Set at $0°$ and $40°$. NASA TM X-2225, June 1971.

12. Hammond, A. D. and Keefer, B. M.: The Effect at High Subsonic Speed of a Flap-Type Aileron on the Chordwise Pressure Distribution Near Mid-Semispan of a Tapered $35°$ Sweptback Wing of Aspect Ratio 4 Having NACA 65A006 Airfoil Section. NACA RML 53C23, May 1953.

13. Aoyagi, K., Falarski, M. D., and Koenig. D. G.: Wind-Tunnel Investigation of a Large-Scale $25°$ Swept-Wing Jet Transport Model with an External Blowing Triple-Slotted Flap. NASA TM X-62,197, Nov. 1973.

14. Küchemann, D. and Weber, J.: _Aerodynamics of Propulsion._ McGraw-Hill Book Co., Inc., 1953.

15. Margason, R. J.: The Path of a Jet Directed at Large Angles to a Subsonic Free Stream. NASA TN D-4919, Nov. 1968.

16. Perry, B., III and Greene, G. C.: Wind-Tunnel Investigation of Aerodynamic Loads on a Large-Scale Externally Blown Flap Model and Comparison with Theory. NASA TN D-7863, Mar. 1975.

17. Smith, C. C., Jr.: Effect of Engine Position and High-Lift Devices on Aerodynamic Characteristics of an External-Flow Jet-Flap STOL Model. NASA TN D-6222, Mar. 1971.

18. Byrd, P. F. and Friedman, M. D.: _Handbook of Elliptic Integrals for Engineers and Physists._ Springer-Verlag, 1954.

$$\frac{u_j b}{\Gamma} \quad \text{at} \quad \frac{x}{b} = 0.0, \quad \frac{y}{a} = 0.0$$

z/b a/b	0	0.25	0.50	0.75	0.90	0.95	1.05	1.10	1.25	1.50
1.0	0.500	0.525	0.623	0.959	1.962	3.600	-2.792	-1.263	-0.393	-0.142
1.5	0.421	0.444	0.535	0.855	1.829	3.441	-2.936	-1.373	-0.460	-0.178
3.0	0.354	0.376	0.463	0.770	1.725	3.321	-3.050	-1.467	-0.526	-0.222
5.0	0.334	0.356	0.441	0.746	1.696	3.375	-3.173	-1.495	-0.548	-0.240
10.0	0.323	0.345	0.430	0.733	1.726	5.571	-5.400	-1.509	-0.560	-0.250
∞	0.318	0.339	0.424	0.728	1.675	3.265	-3.106	-1.516	-0.566	-0.255

Table I.- Induced axial velocity in the plane
of an elliptic vortex ring.

$$\frac{u_j b}{\Gamma} \quad \text{at} \quad \frac{x}{b} = 0.5, \quad \frac{y}{a} = 0.0$$

z/b \ a/b	0	0.25	0.50	0.75	0.90	0.95	1.05	1.10	1.25	1.50
1.0	0.358	0.357	0.346	0.286	0.204	0.170	0.102	0.072	0.004	−0.035
1.5	0.326	0.327	0.321	0.270	0.192	0.160	0.092	0.060	−0.010	−0.049
3.0	0.284	0.286	0.283	0.238	0.165	0.133	0.066	0.030	−0.030	−0.074
5.0	0.268	0.270	0.268	0.224	0.152	0.120	0.054	0.023	−0.048	−0.086
10.0	0.259	0.261	0.259	0.216	0.144	0.112	0.046	0.014	−0.055	−0.094
∞	0.255	0.257	0.255	0.211	0.140	0.108	0.042	0.010	−0.060	−0.098

$$\frac{w_j b}{\Gamma} \quad \text{at} \quad \frac{x}{b} = 0.5, \quad \frac{y}{a} = 0.0$$

z/b \ a/b	0	0.25	0.50	0.75	0.90	0.95	1.05	1.10	1.25	1.50
1.0	0	0.056	0.129	0.220	0.259	0.264	0.255	0.242	0.188	0.102
1.5	0	0.056	0.130	0.228	0.276	0.283	0.278	0.268	0.214	0.122
3.0	0	0.055	0.129	0.231	0.284	0.293	0.293	0.284	0.233	0.140
5.0	0	0.054	0.128	0.231	0.235	0.295	0.296	0.287	0.238	0.144
10.0	0	0.054	0.127	0.230	0.285	0.295	0.297	0.288	0.239	0.146
∞	0	0.054	0.127	0.231	0.286	0.296	0.297	0.289	0.240	0.147

Table II.- Induced velocity field out of the plane
of an elliptic vortex ring.

$$\frac{u_j b}{\Gamma} \quad \text{at} \quad \frac{x}{b} = 1.0, \quad \frac{y}{a} = 0.0$$

z/b a/b	0	0.25	0.50	0.75	0.90	0.95	1.05	1.10	1.25	1.50
1.0	0.177	0.170	0.151	0.118	0.093	0.085	0.069	0.061	0.039	0.014
1.5	0.186	0.180	0.161	0.127	0.102	0.093	0.075	0.066	0.043	0.014
3.0	0.178	0.172	0.155	0.123	0.098	0.089	0.071	0.062	0.037	0.007
5.0	0.169	0.164	0.147	0.115	0.091	0.082	0.064	0.055	0.031	0.000
10.0	0.163	0.158	0.141	0.109	0.085	0.076	0.058	0.049	0.025	−0.005
∞	0.159	0.154	0.137	0.106	0.081	0.073	0.055	0.046	0.022	−0.009

$$\frac{w_j b}{\Gamma} \quad \text{at} \quad \frac{x}{b} = 1.0, \quad \frac{y}{a} = 0.0$$

z/b a/b	0	0.25	0.50	0.75	0.90	0.95	1.05	1.10	1.25	1.50
1.0	0	0.033	0.063	0.084	0.090	0.091	0.090	0.089	0.082	0.064
1.5	0	0.037	0.071	0.098	0.106	0.108	0.108	0.107	0.100	0.080
3.0	0	0.039	0.077	0.108	0.119	0.121	0.123	0.123	0.117	0.098
5.0	0	0.040	0.078	0.110	0.122	0.124	0.126	0.126	0.121	0.103
10.0	0	0.040	0.078	0.110	0.123	0.125	0.128	0.128	0.123	0.105
∞	0	0.040	0.078	0.111	0.123	0.126	0.128	0.128	0.124	0.105

Table II.- Continued.

$$\frac{u_j b}{\Gamma} \quad \text{at} \quad \frac{x}{b} = 1.5, \quad \frac{y}{a} = 0.0$$

z/b \ a/b	0	0.25	0.50	0.75	0.90	0.95	1.05	1.10	1.25	1.50
1.0	0.085	0.082	0.074	0.061	0.052	0.049	0.042	0.040	0.031	0.019
1.5	0.101	0.097	0.088	0.073	0.063	0.059	0.052	0.048	0.038	0.023
3.0	0.108	0.105	0.095	0.079	0.068	0.064	0.056	0.053	0.041	0.025
5.0	0.105	0.102	0.092	0.076	0.065	0.062	0.054	0.050	0.038	0.022
10.0	0.101	0.098	0.088	0.072	0.062	0.058	0.050	0.046	0.035	0.018
∞	0.098	0	0.085	0.070	0.059	0.055	0.047	0.043	0.032	0.015

$$\frac{w_j b}{\Gamma} \quad \text{at} \quad \frac{x}{b} = 1.5, \quad \frac{y}{a} = 0.0$$

z/b \ a/b	0	0.25	0.50	0.75	0.90	0.95	1.05	1.10	1.25	1.50
1.0	0	0.014	0.027	0.036	0.039	0.039	0.040	0.040	0.039	0.035
1.5	0	0.018	0.033	0.045	0.049	0.050	0.051	0.051	0.050	0.046
3.0	0	0.021	0.040	0.054	0.060	0.062	0.063	0.064	0.064	0.060
5.0	0	0.022	0.042	0.057	0.063	0.065	0.067	0.068	0.068	0.065
10.0	0	0.022	0.042	0.058	0.064	0.066	0.068	0.069	0.070	0.067
∞	0	0.022	0.042	0.058	0.065	0.066	0.069	0.070	0.071	0.067

Table II.- Concluded.

c_μ	α (degs.)	$c_{L_S} + c_{L_B}$	c_{m_S}
0	18.5	----	0.028
2.3	6.5	0.14	-----
	18.5	1.10	0.070
4.0	6.5	0.54	0.032
	18.5	1.25	0.074
	26.5	1.72	0.096

Table III.- Combined lift due to leading-edge slat, fuselage, and nacelles; and pitching moment due to leading-edge slats on the EBF configuration of references 13 and 16.

c_T	$c_{D_{ram}}$
0.25	0.057
0.58	0.088
1.0	0.118

Table IV.- Ram drag coefficient for a single JT15D-1 turbofan engine, reference 13.
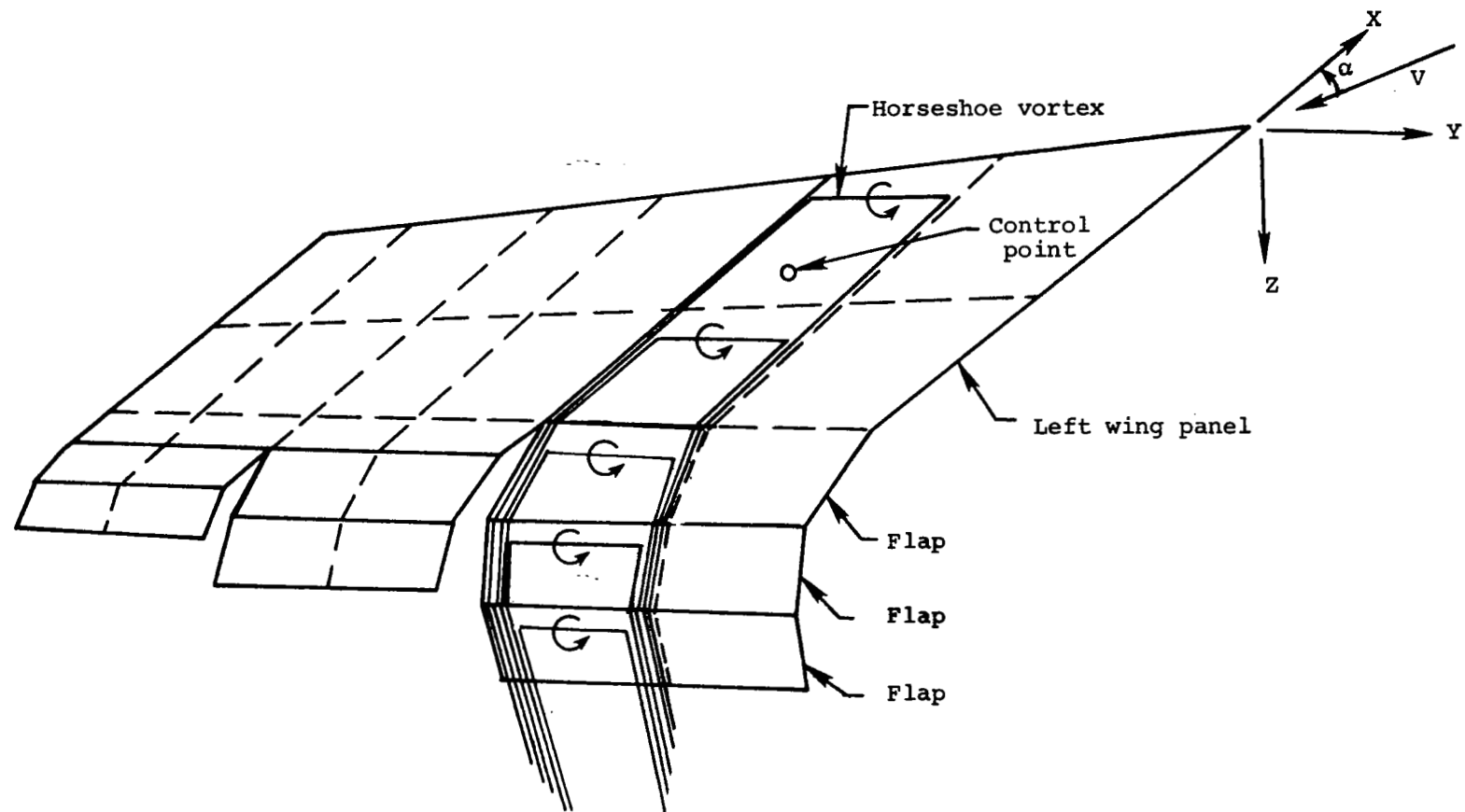
Figure 1.- Multiple flap vortex lattice arrangement.
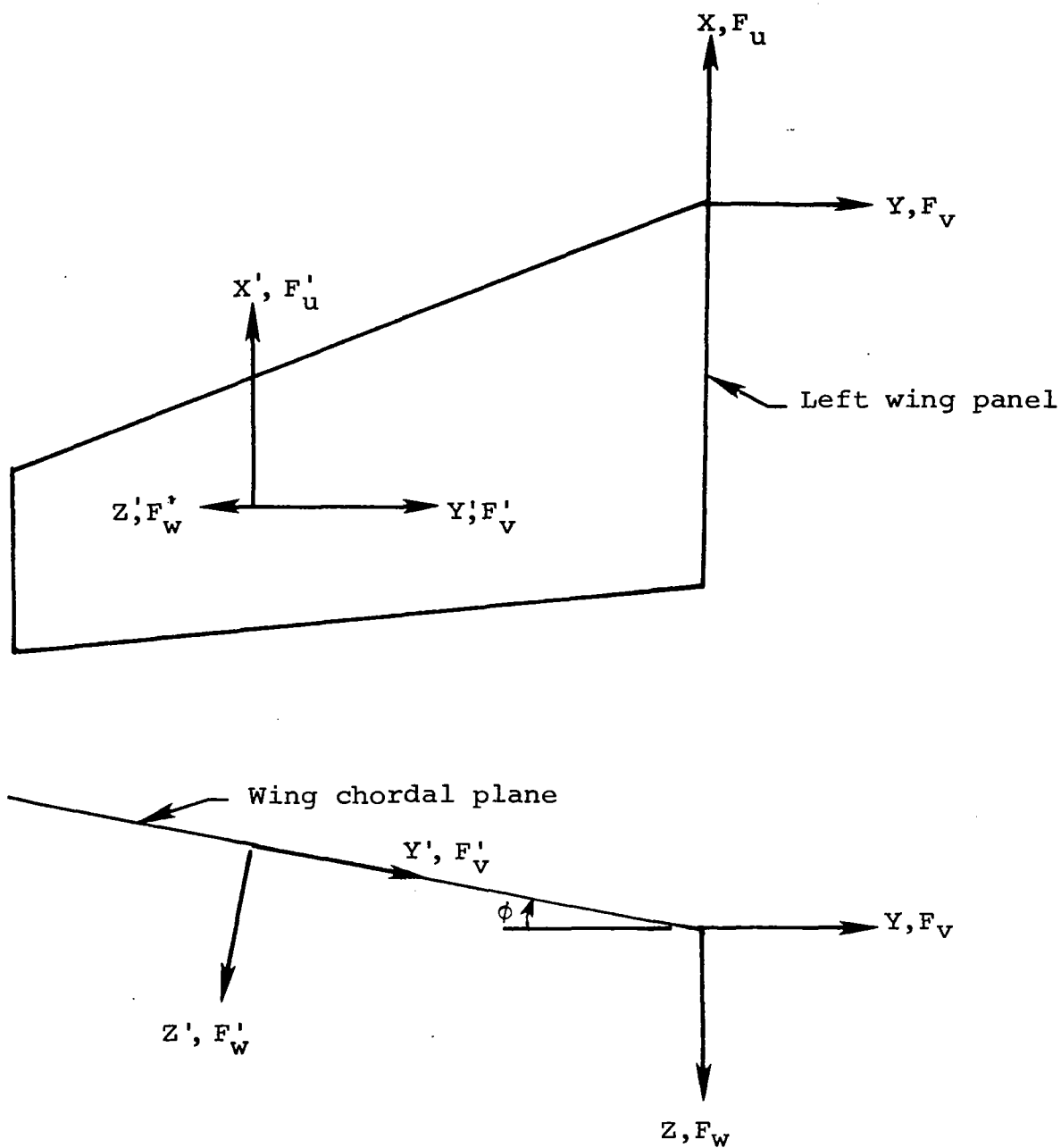
(a) Wing coordinate systems.

Figure 2.- Coordinate systems used in
determining wing boundary condition.
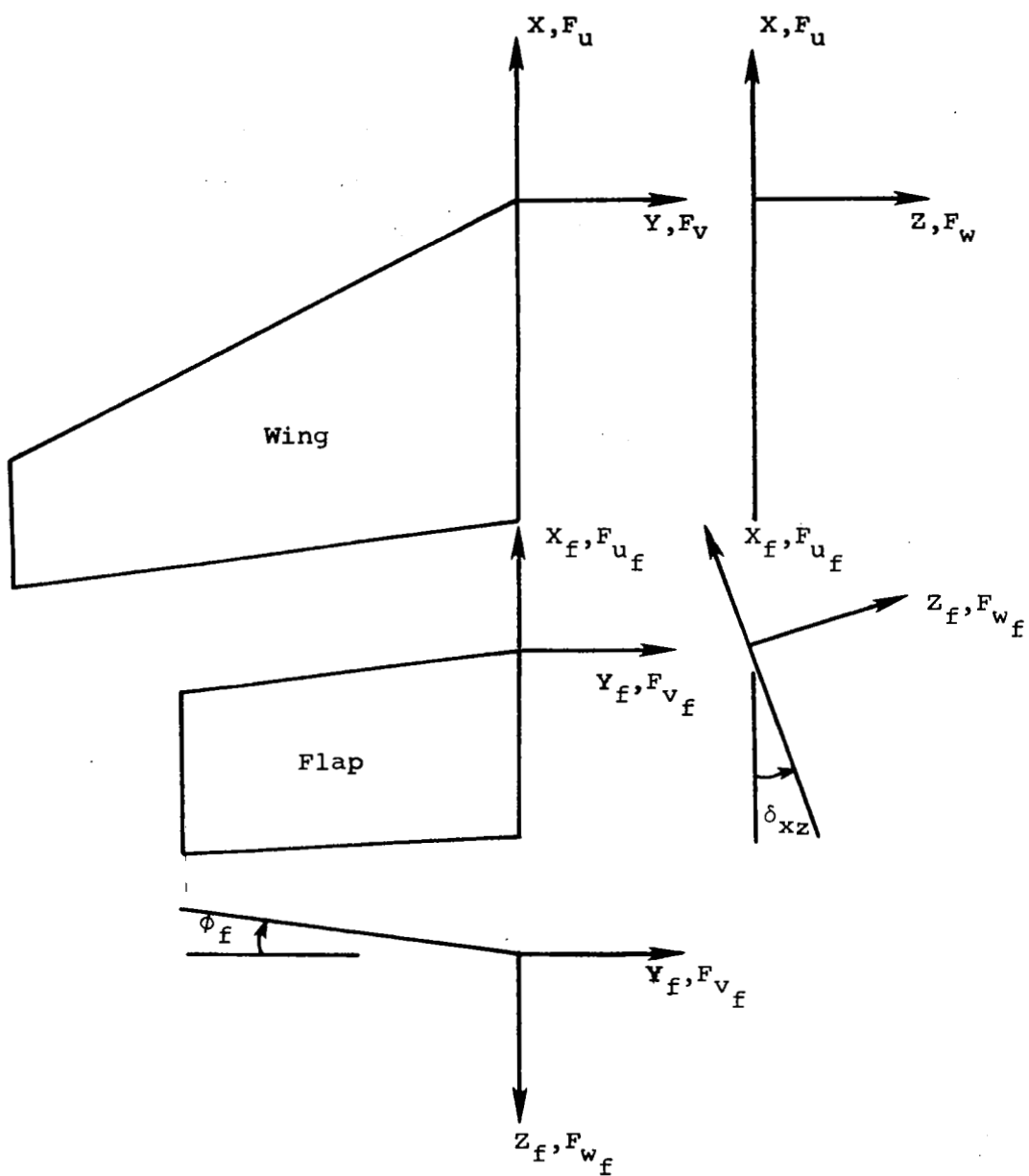
(b) Relationship between wing and flap
coordinate system.

Figure 2.- Concluded.
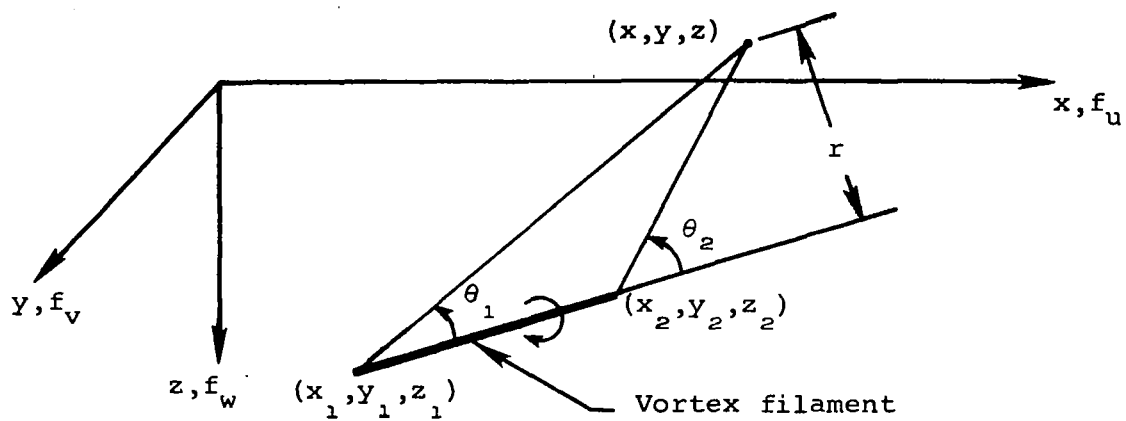
(a) Finite length vortex filament.
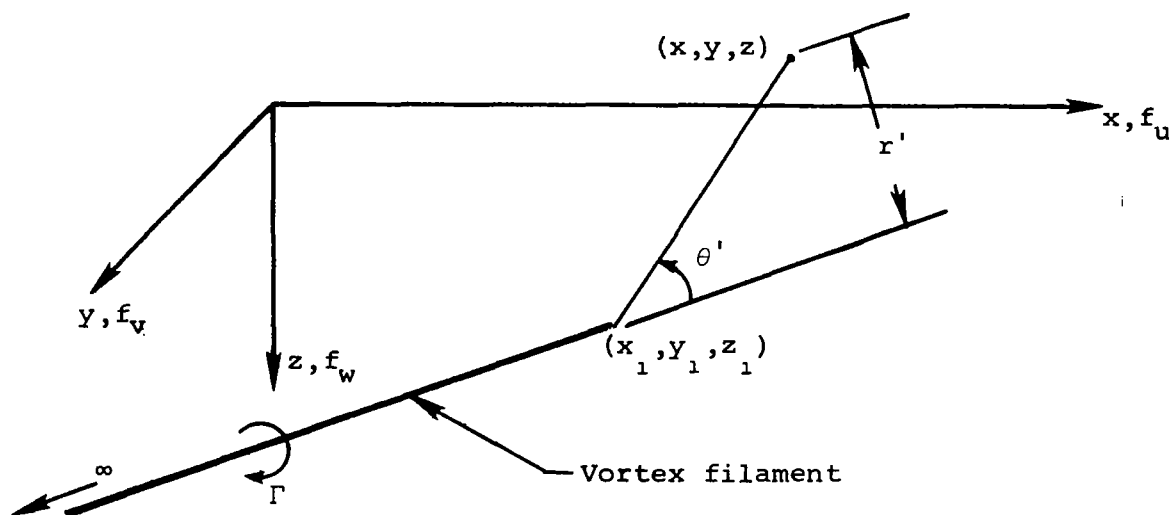
(b) Semi-infinite vortex filament.

Figure 3.- Influence function coordinate systems.
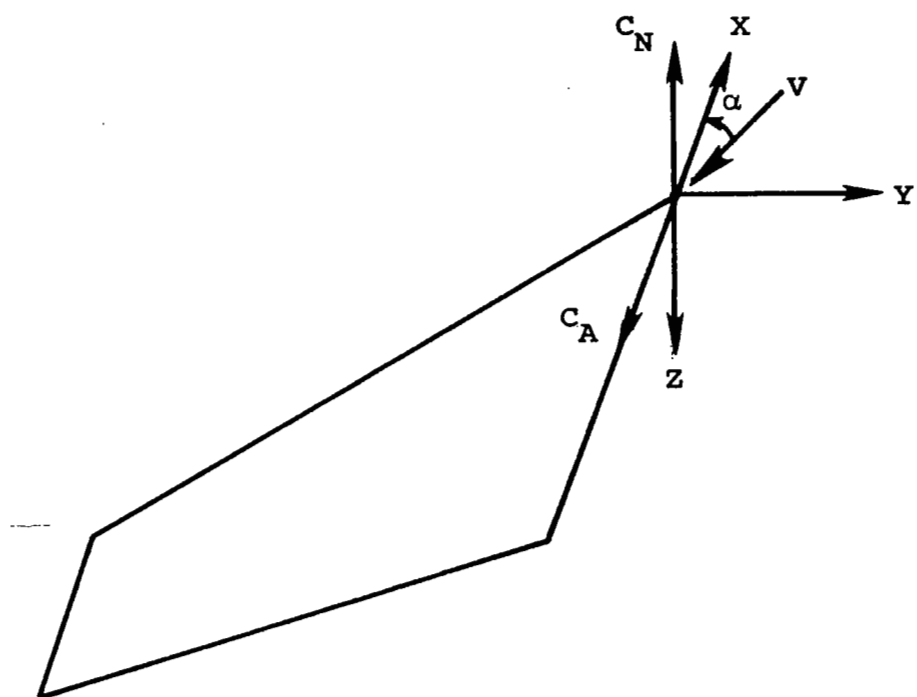
(a)   Positive directions of wing forces.
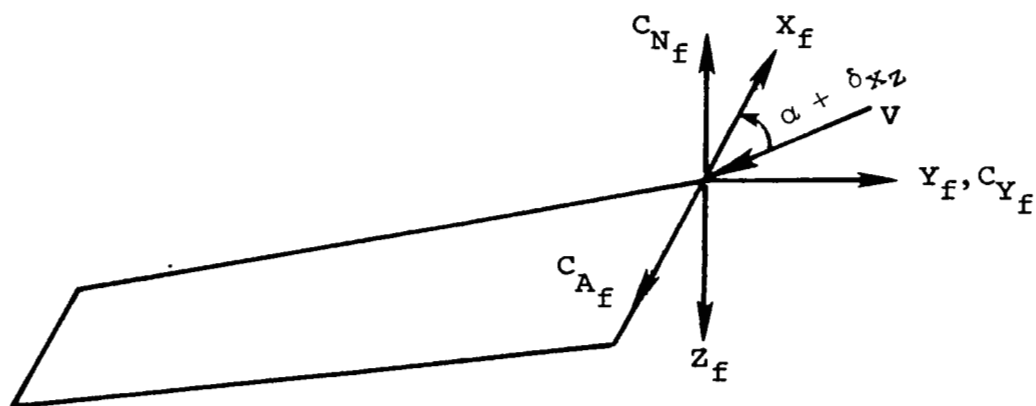
(b)   Positive directions of flap forces.

Figure 4.- Force and moment coefficient definitions
on individual wing and flap surfaces.
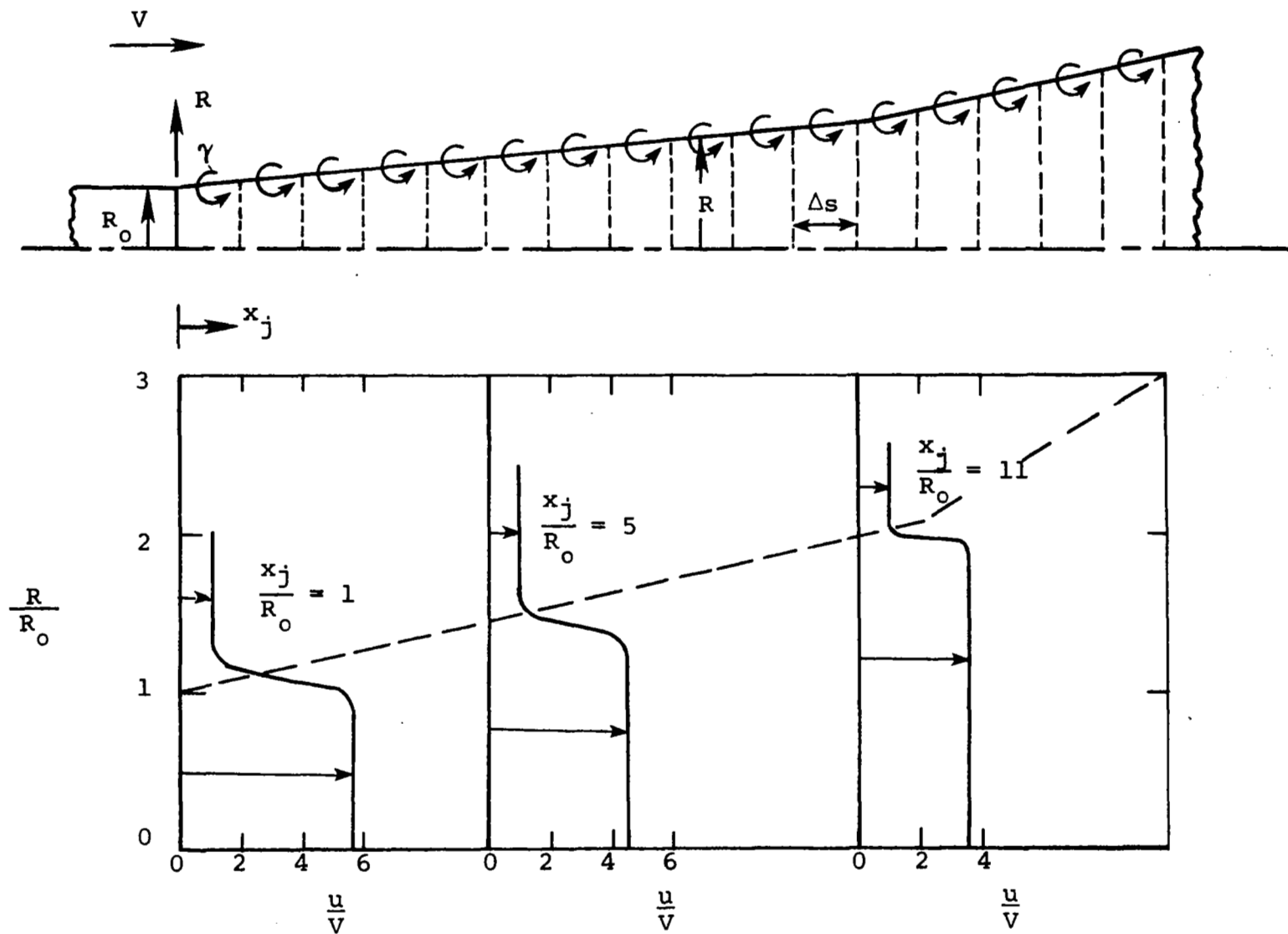
Figure 5.- Vortex ring wake model and velocity
profiles for $V_j/V = 6$.
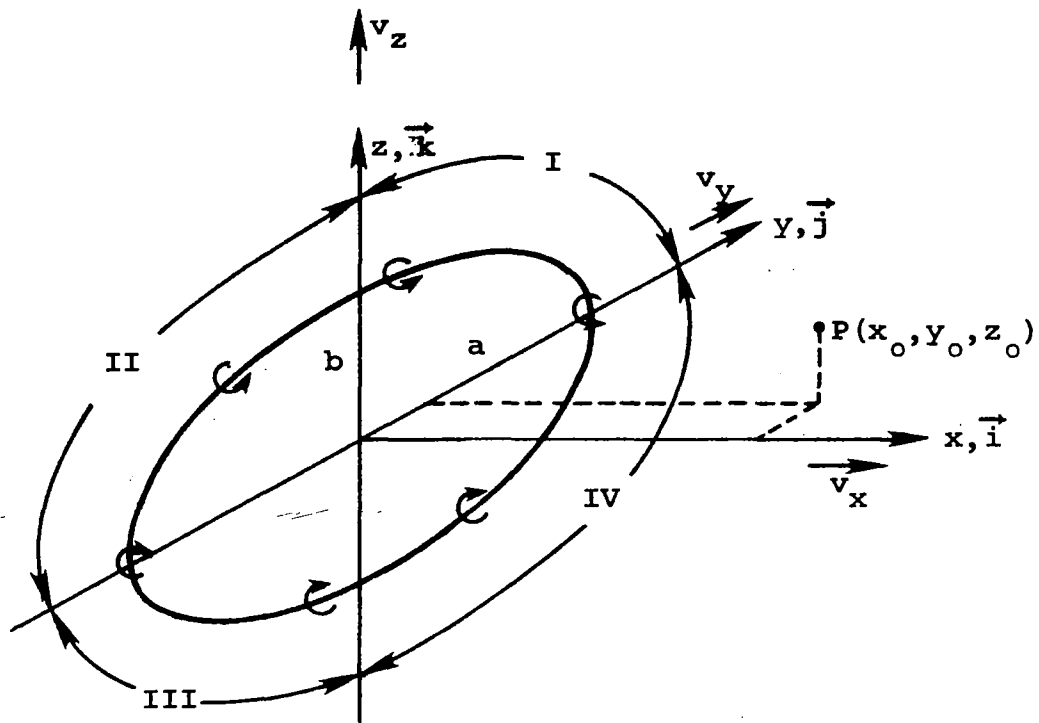
(a) Ring coordinate system.
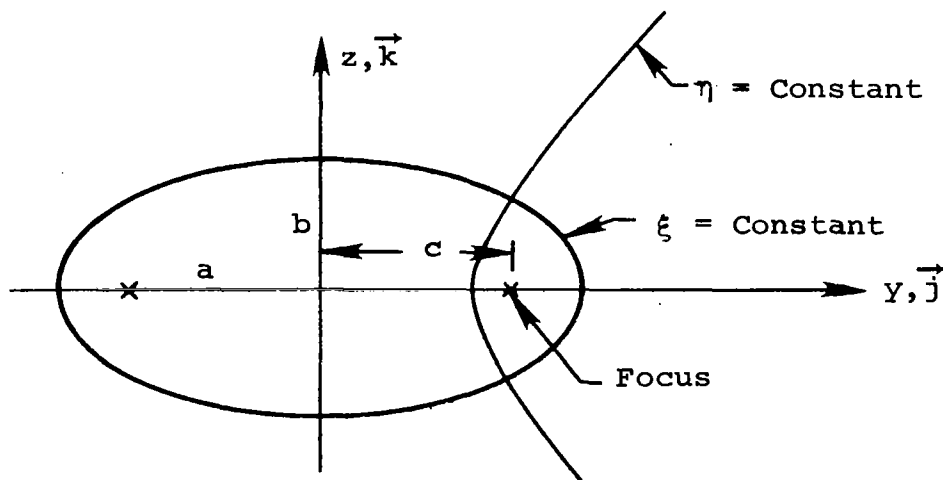
(b) Sketch of ellipse.

Figure 6.- Elliptic vortex ring.
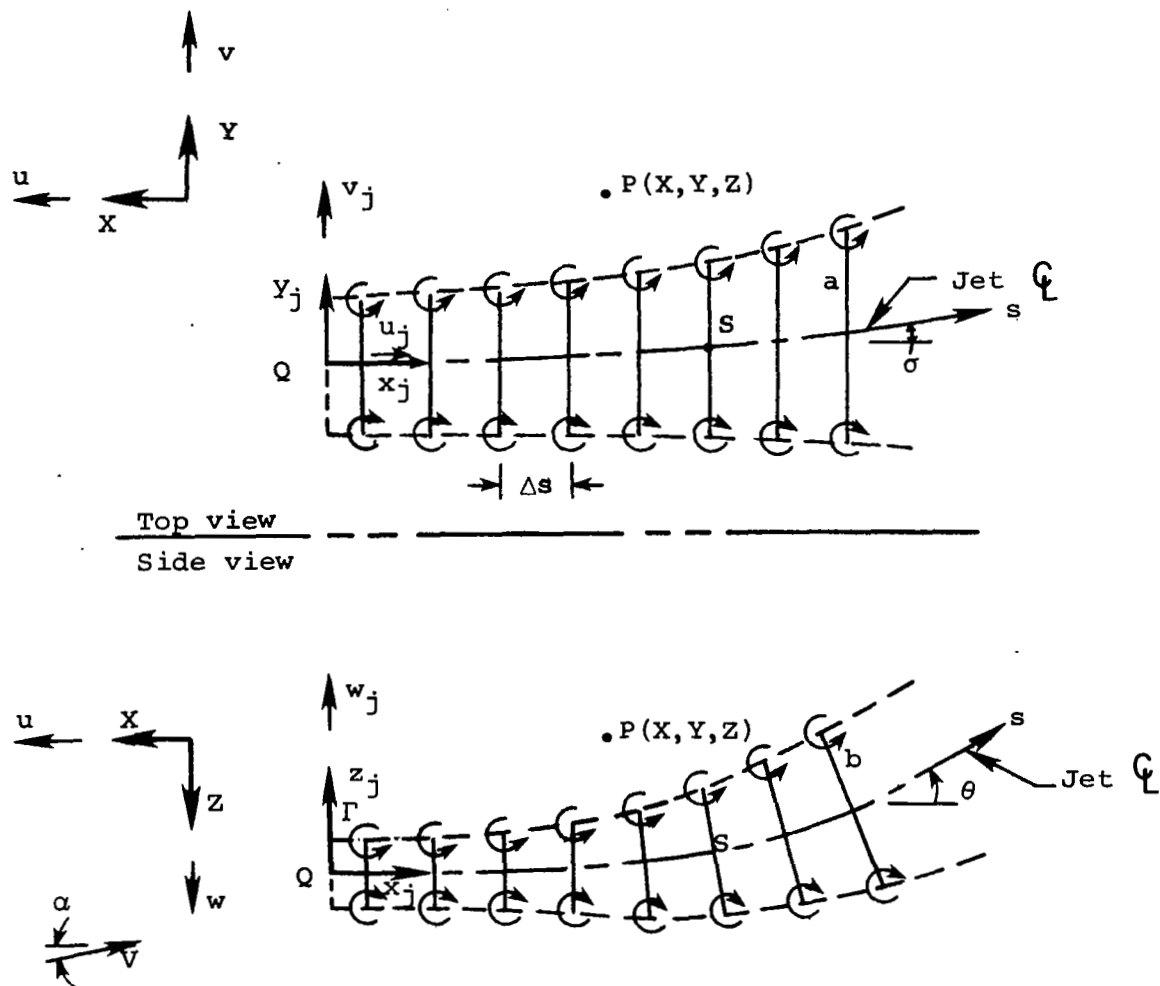
Figure 7.- Vortex ring jet model.
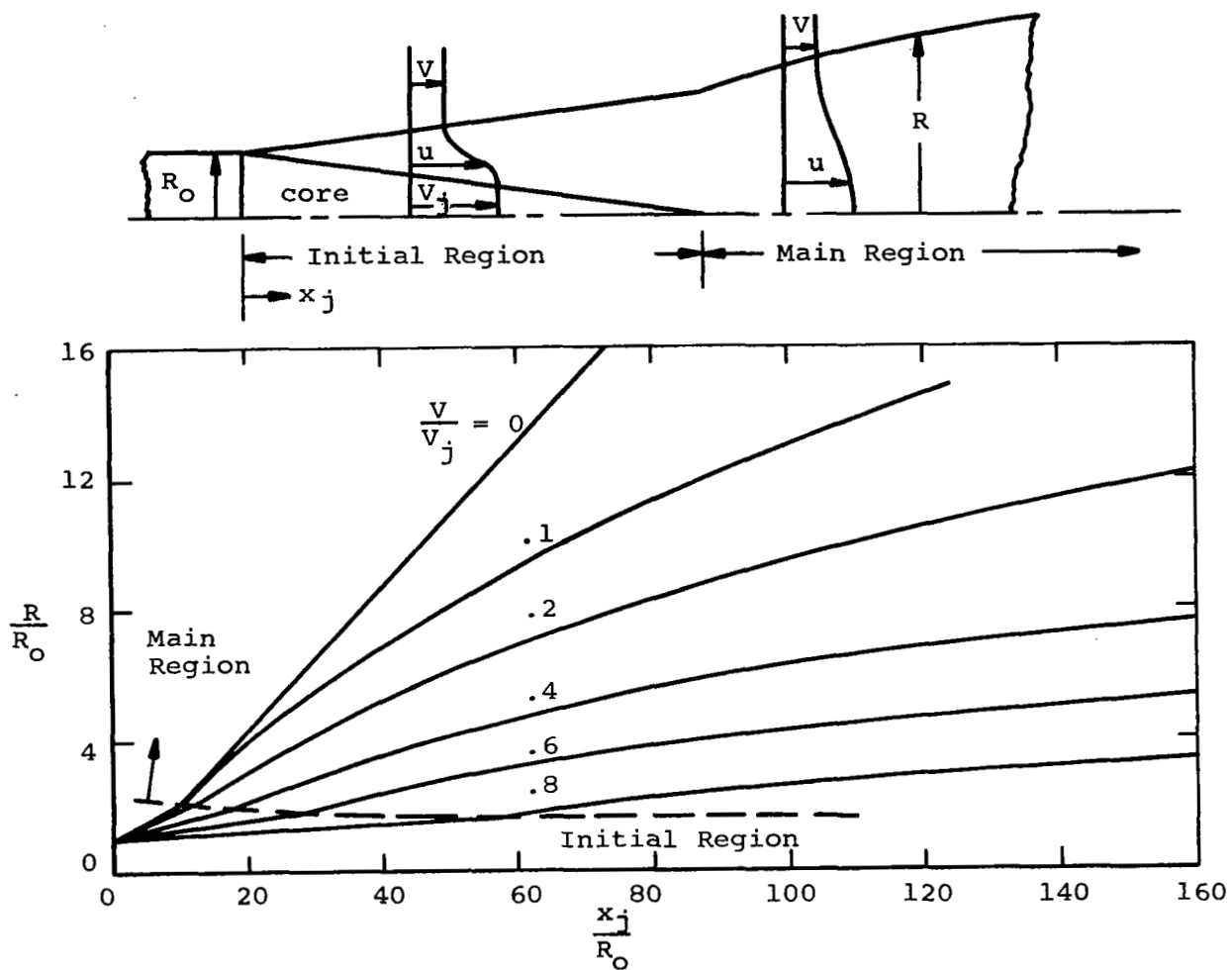
Figure 8.- Analytical spreading rate of an
axisymmetric jet in a coflowing stream.
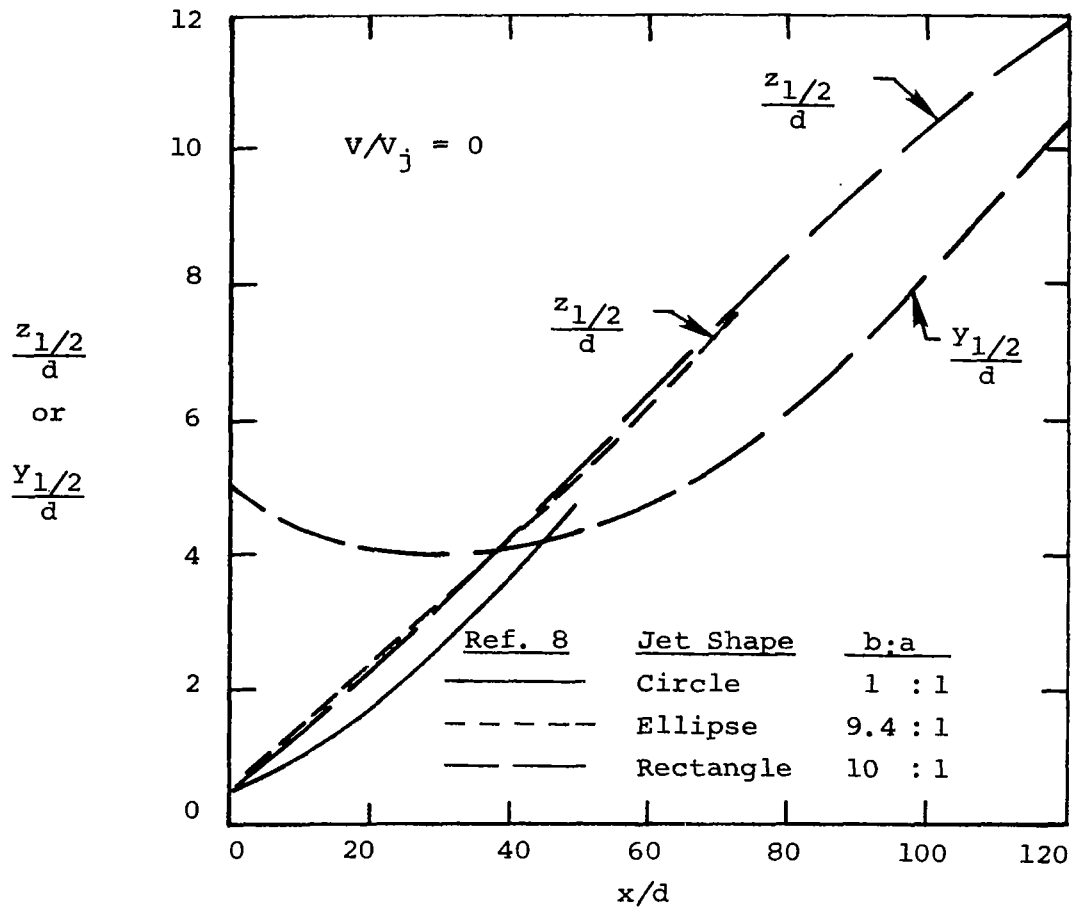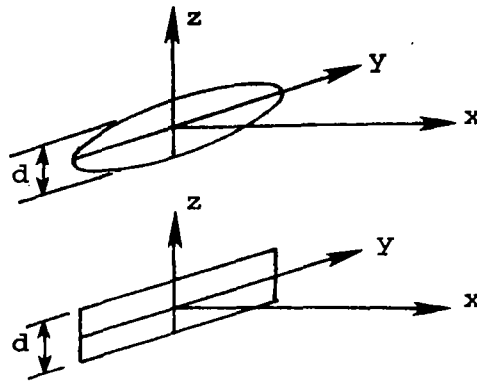
Figure 9.- Measured half-width boundaries of circular, elliptical, and rectangular cross-section jets exhausting into still air.
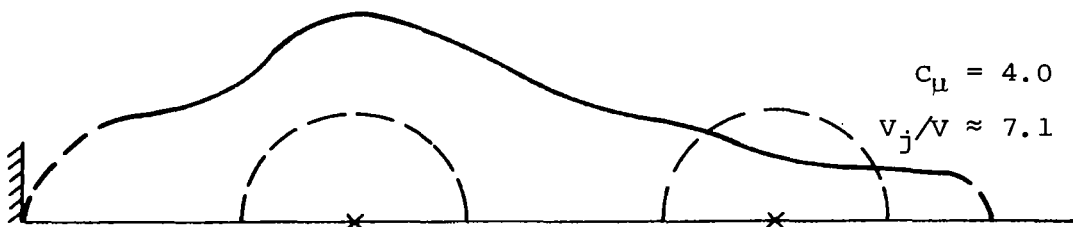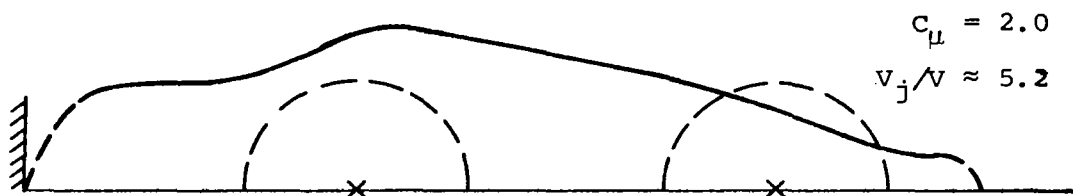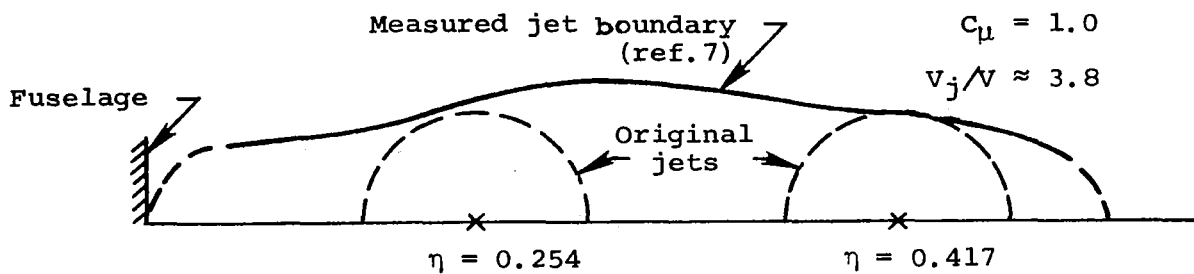
Figure 10.- Spanwise variation of measured jet height
distributions at approximately one flap chord aft
of EBF model at various thrust coefficients.
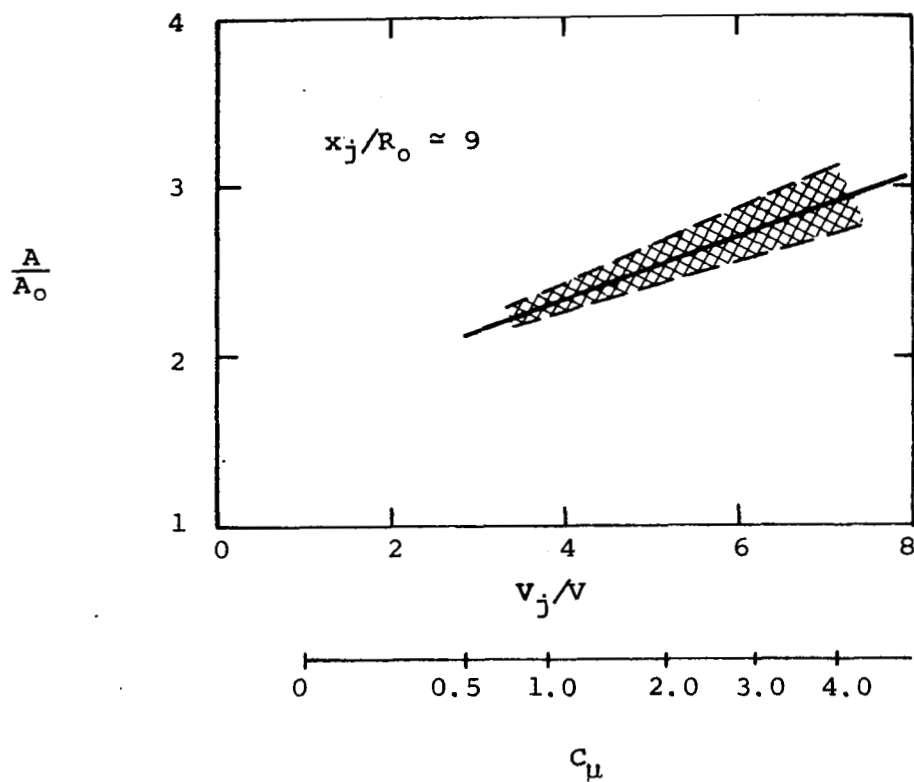
(a) Jet area ratio.
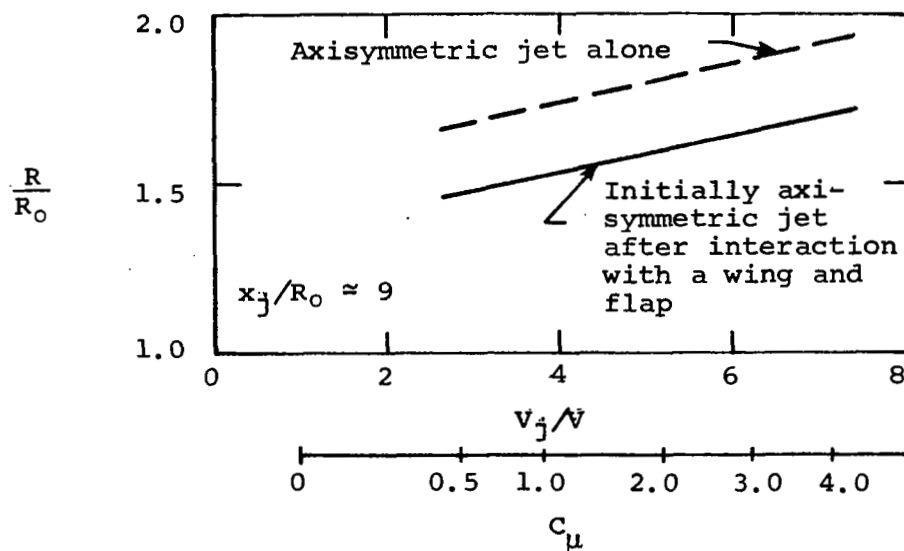
(b) Equivalent radius ratio.

Figure 11.- Measured jet expansion on
an EBF model.
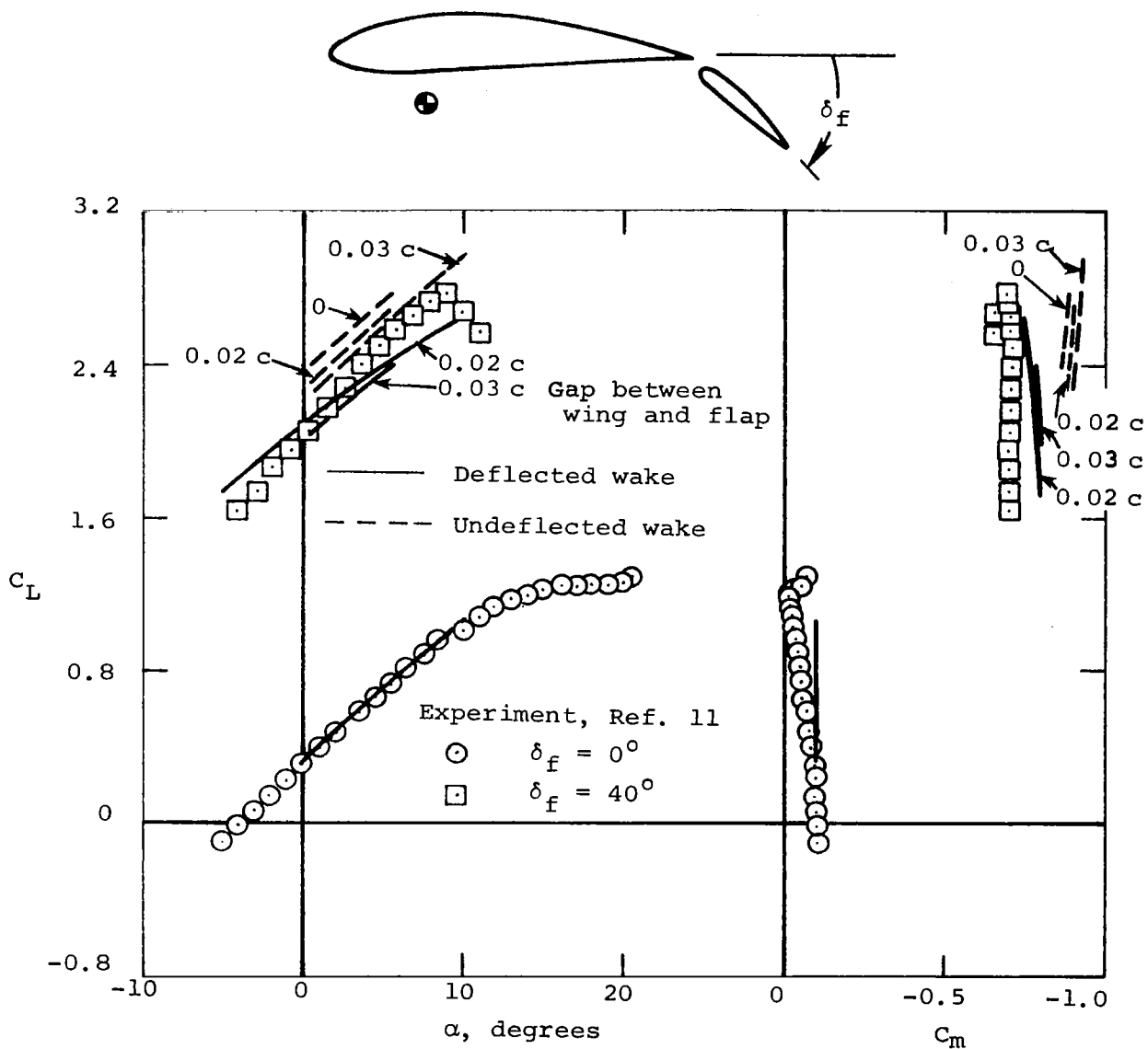
(a) Lift and pitching moment coefficients.

Figure 12.- Measured and predicted aerodynamic characteristics of an unswept wing with single slotted flap deflected 40°.

α = 0.47°

⊙   Experiment, Ref. 11

——— Deflected wake } gap = 0.02 c
- - - Undeflected wake

α = 5.65°
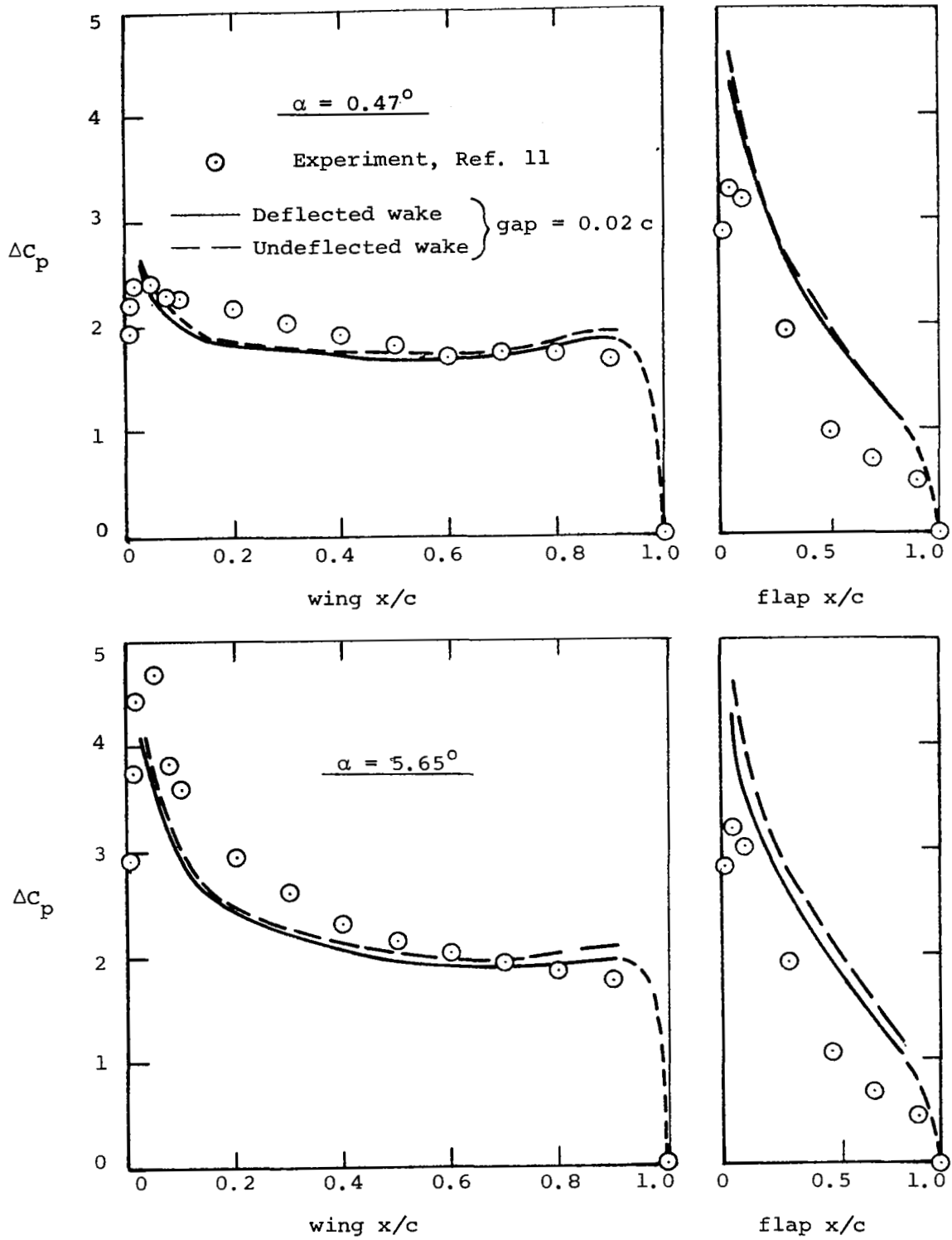
(b) Pressure distribution at η̇ = 0.25.

Figure 12.- Concluded.

	Predicted Values	
	Deflected Wake	Undeflected Wake
C_L	0.162	0.166
C_m	-0.168	-0.170
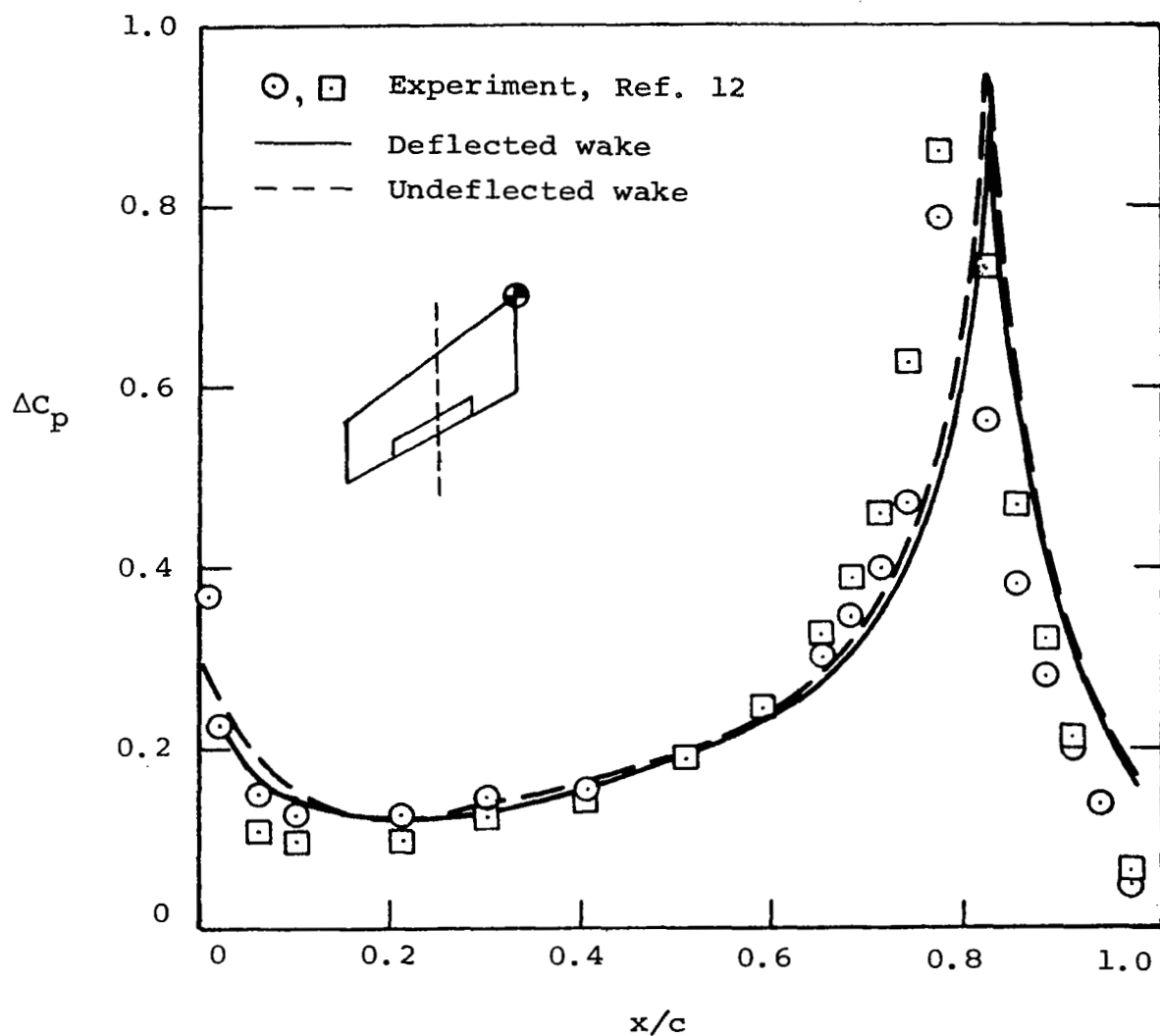
Figure 13.- Measured and predicted pressure distribution at $\eta = 0.46$ on a 35° swept wing with a partial span flap deflected 10°.
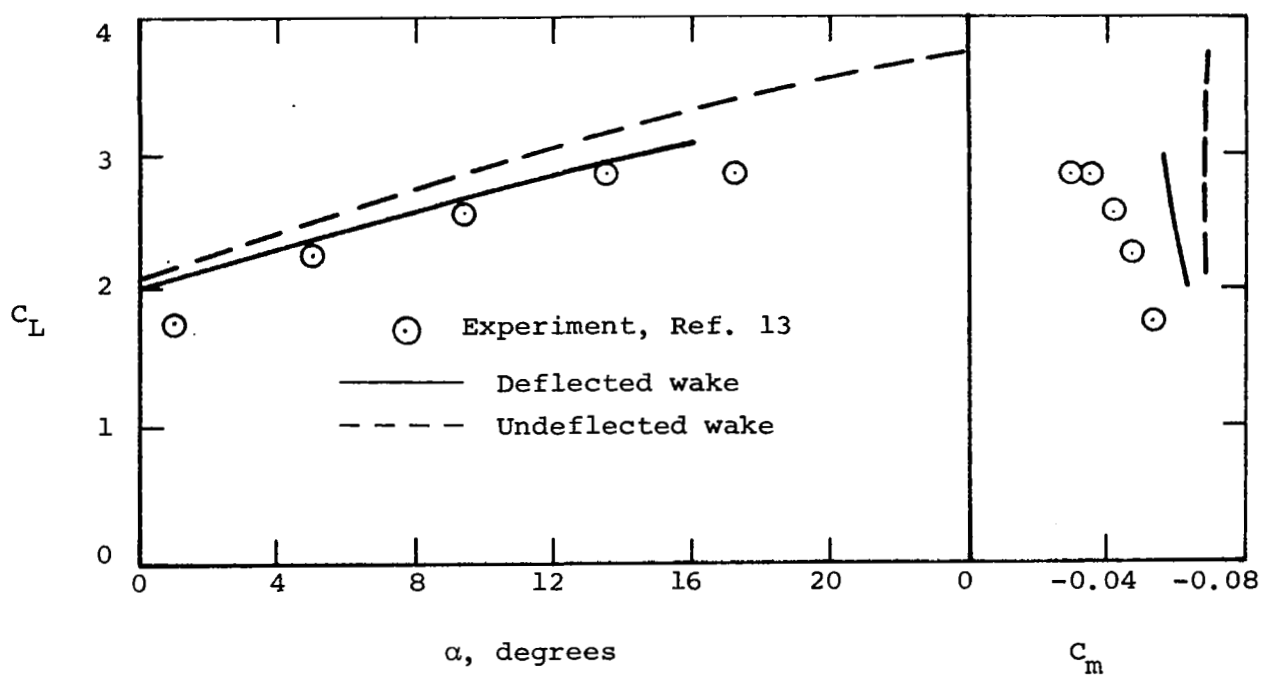
Figure 14.- Effect of vortex lattice trailing-leg position
on the predicted lift and moment characteristics
of a swept wing with triple slotted flaps
deflected 0°, 20°, and 40°.
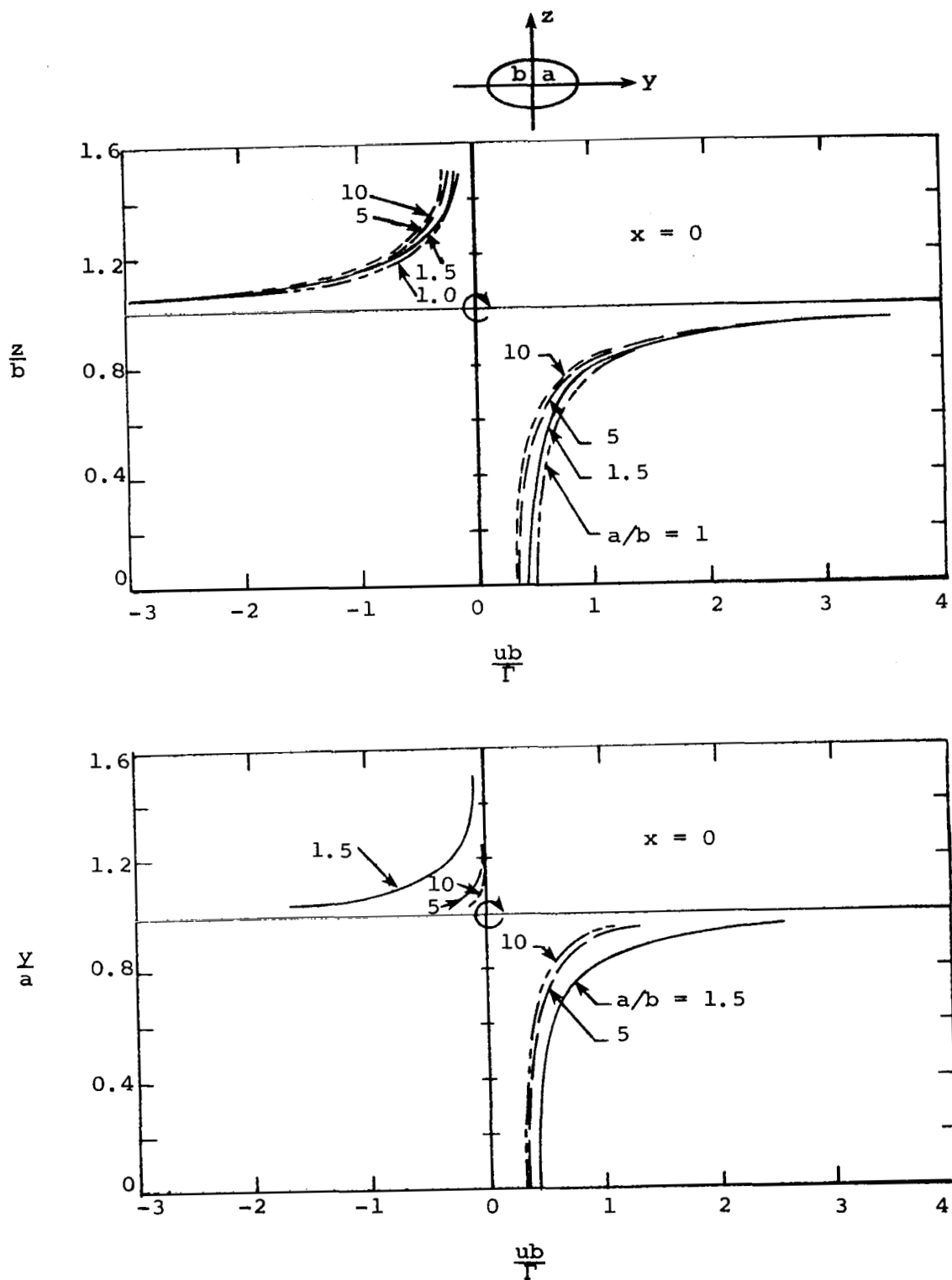
Figure 15.- Axial velocity induced by an elliptic
vortex ring in the plane of the ring.
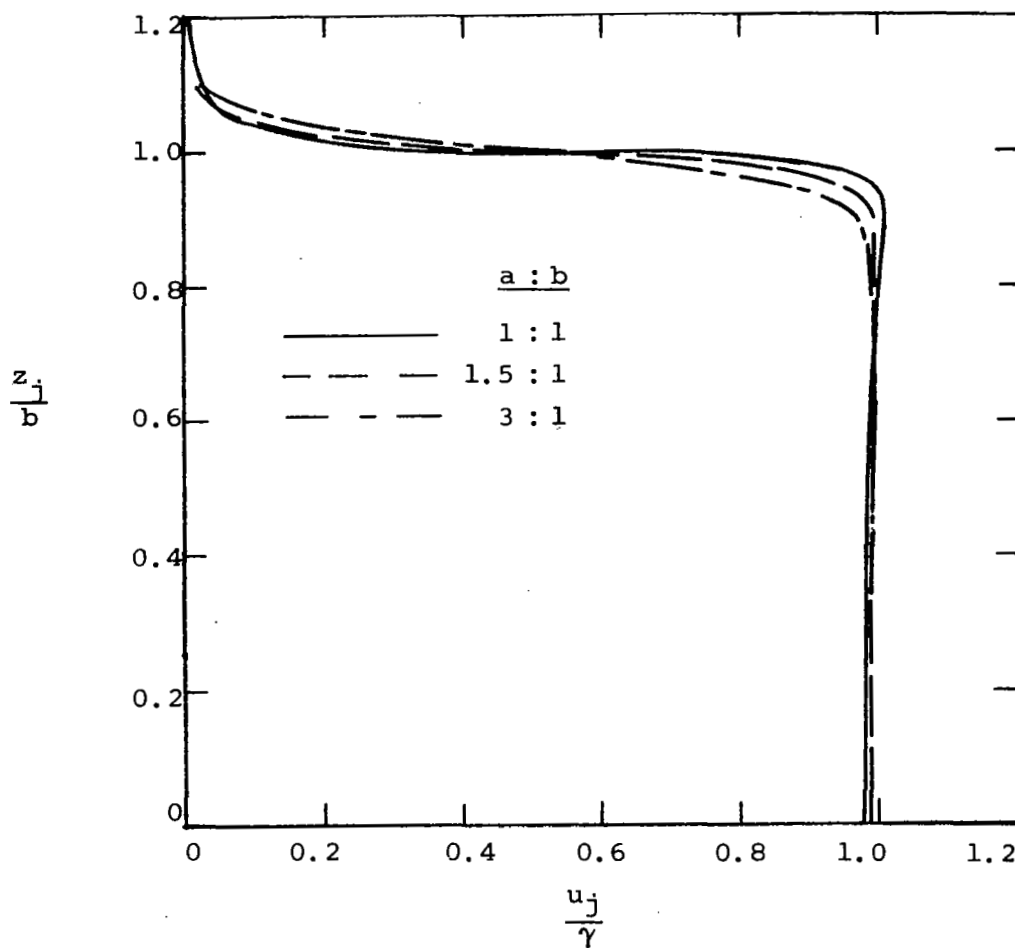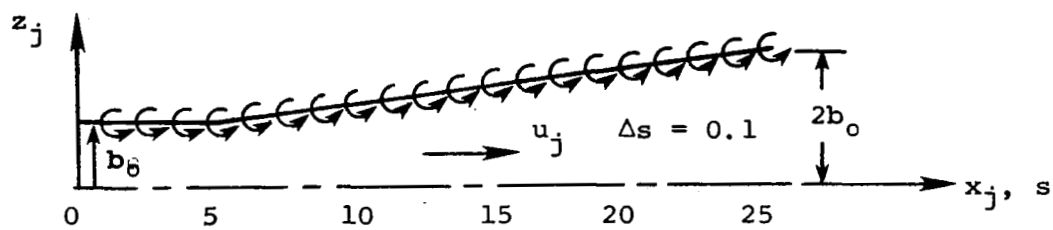
(a) $P/P_o = 1.0$, $y/a = 0.0$

Figure 16.- Induced axial velocity profiles inside elliptic jets.
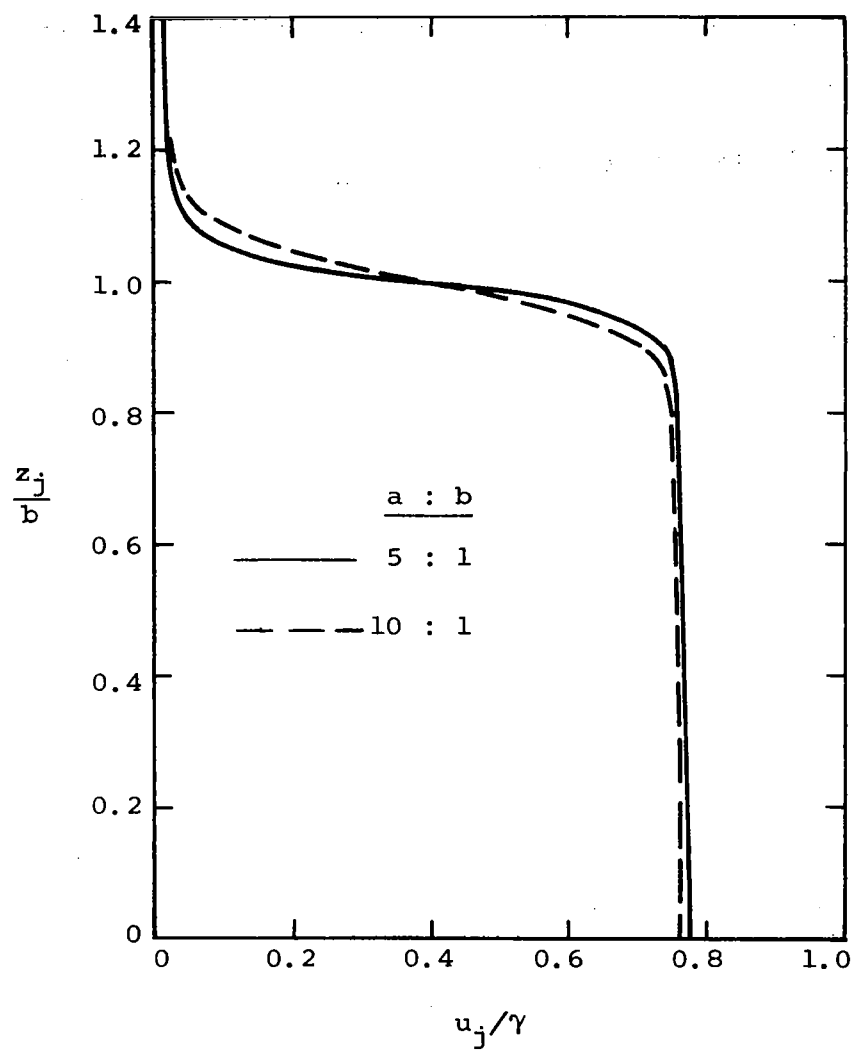
(b) $P/P_o = 1.25$, $y_j/a = 0$.

Figure 16.- Continued.
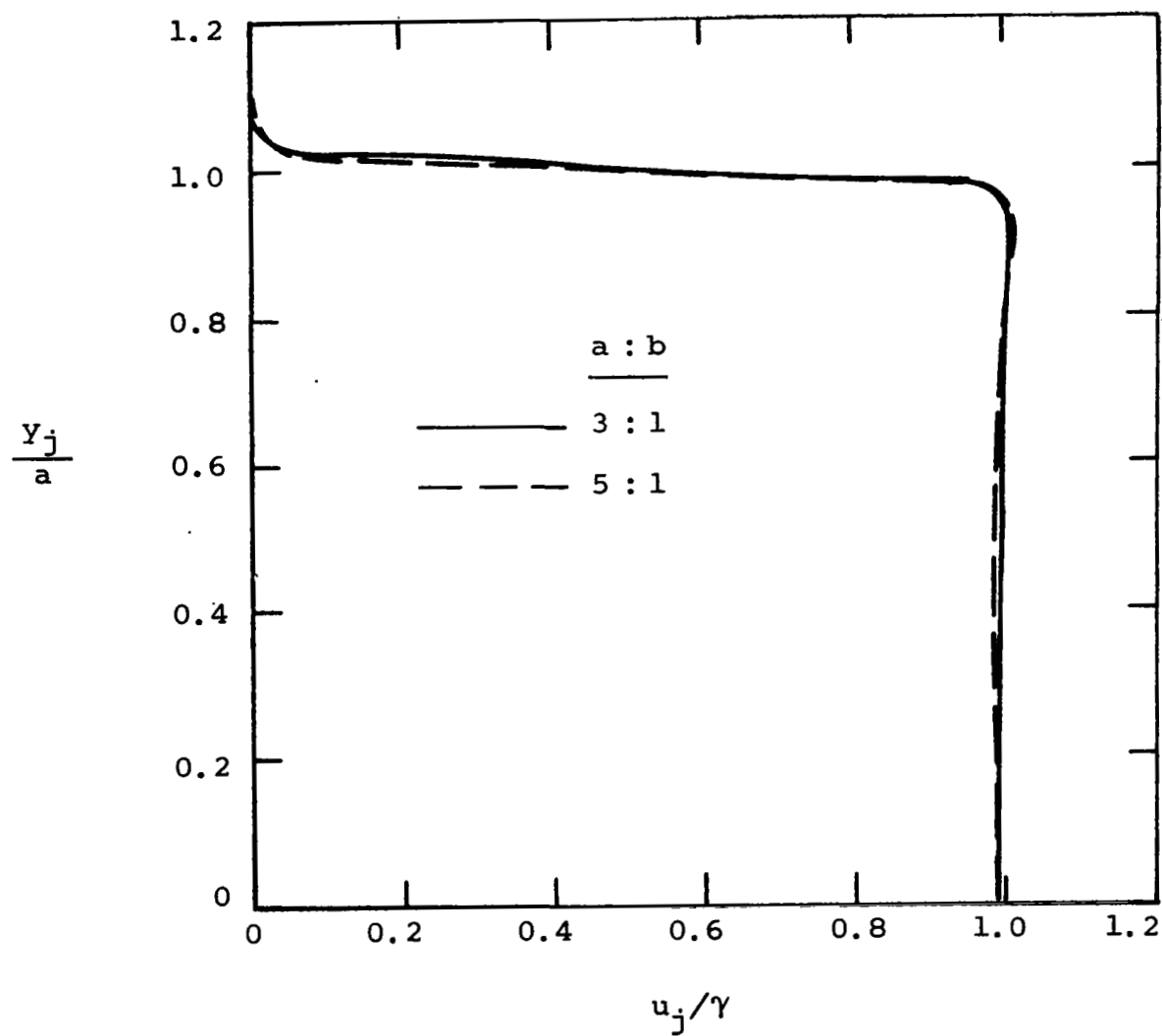
(c) $P/P_0 = 1.0$, $z_j/b = 0.0$.

Figure 16.- Continued.
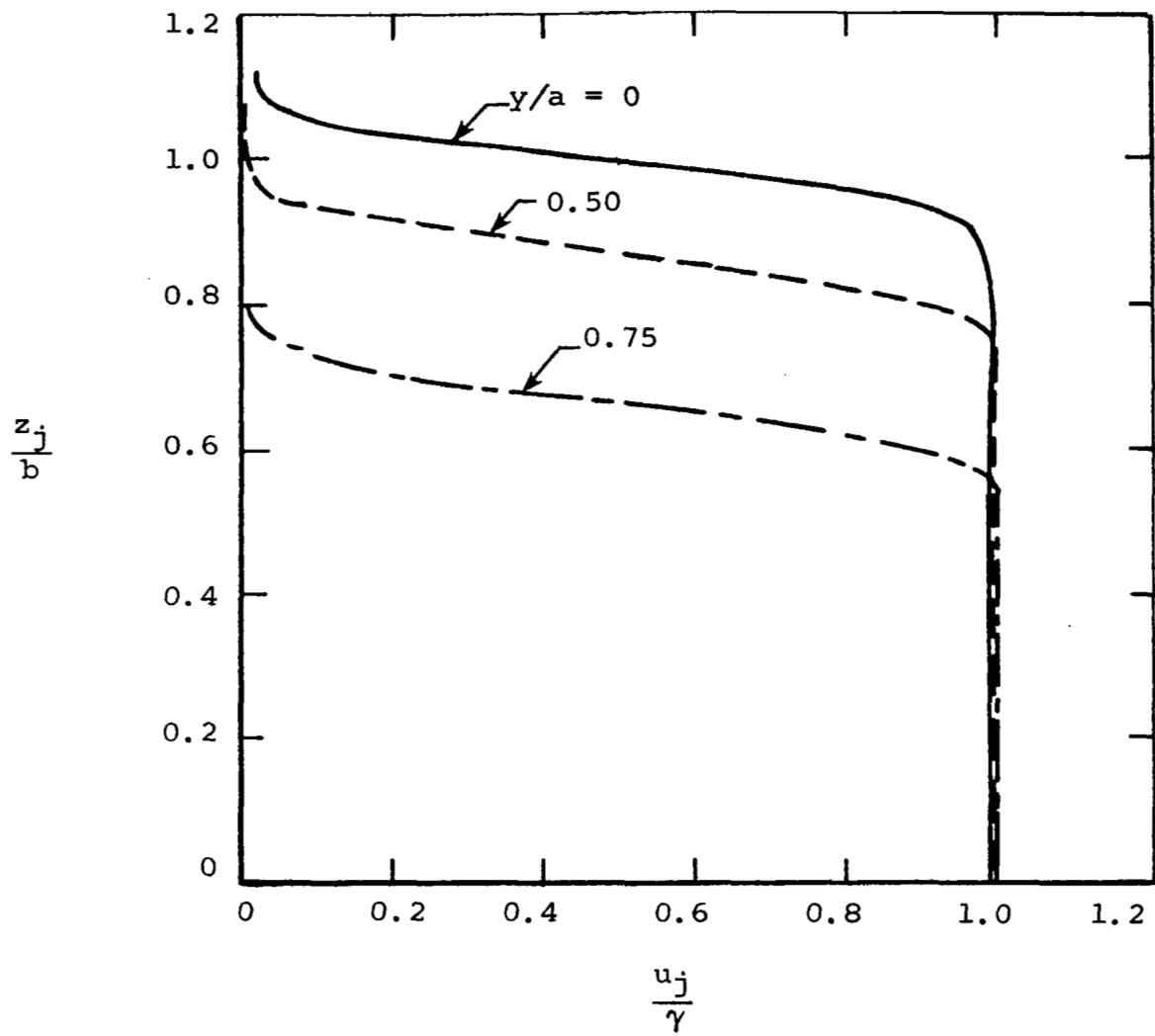
(d) $P/P_o = 1.0$, $a/b = 3$.

Figure 16.- Concluded.
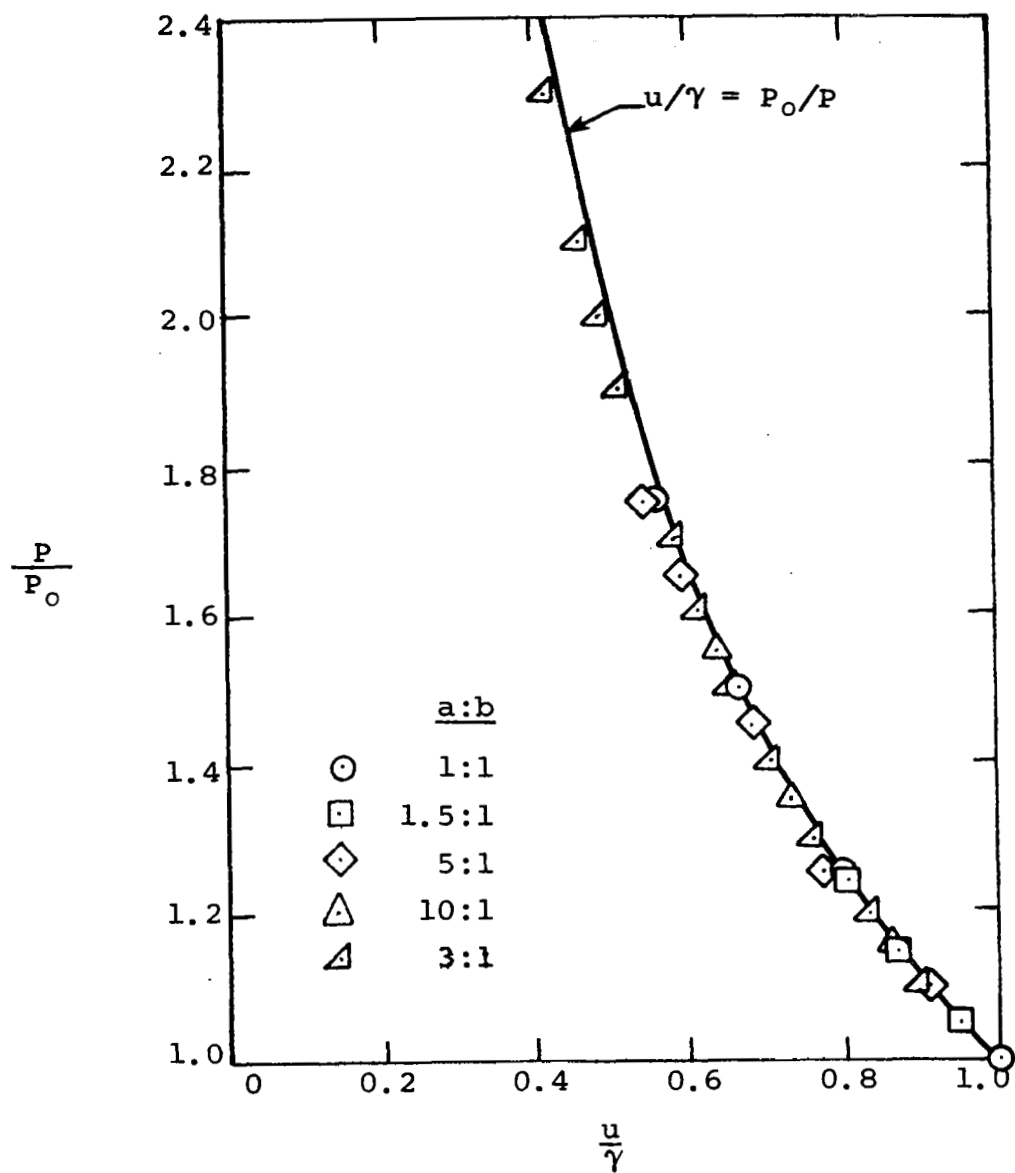
Figure 17.- Effect of jet expansion on
the predicted axial velocity
on the jet centerline.

98
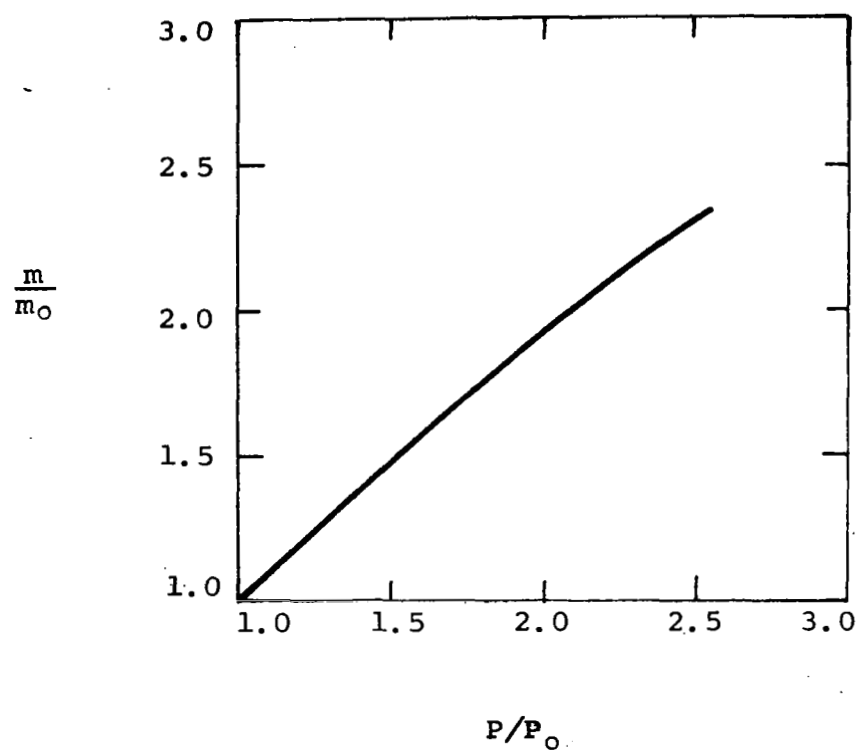
Figure 18.- Mass flow in expanding
vortex ring jet model.
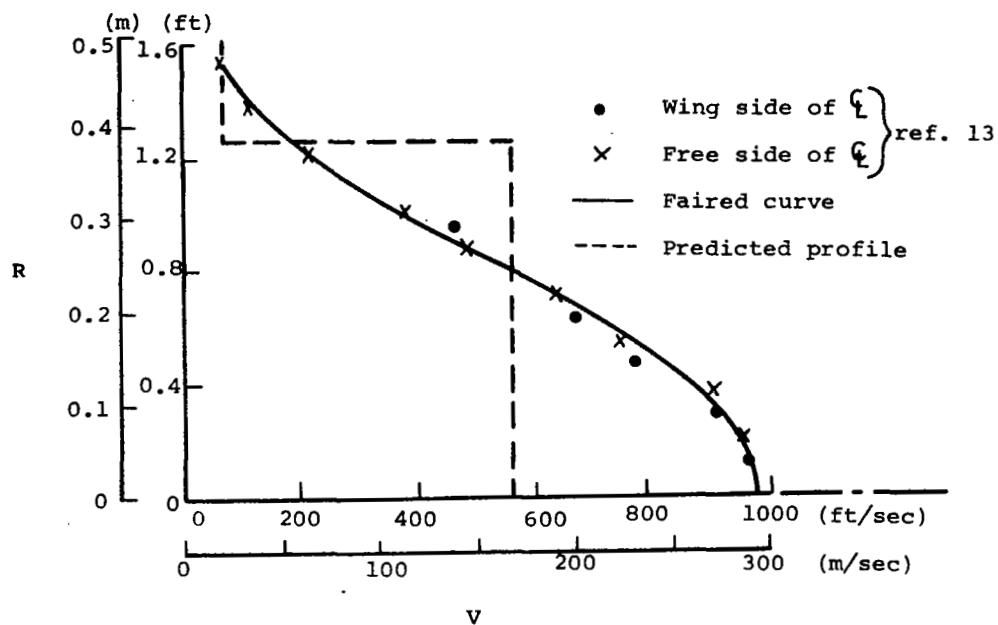
(a) $C_T = 0.966$, T = 5338 newtons (1200 pounds).
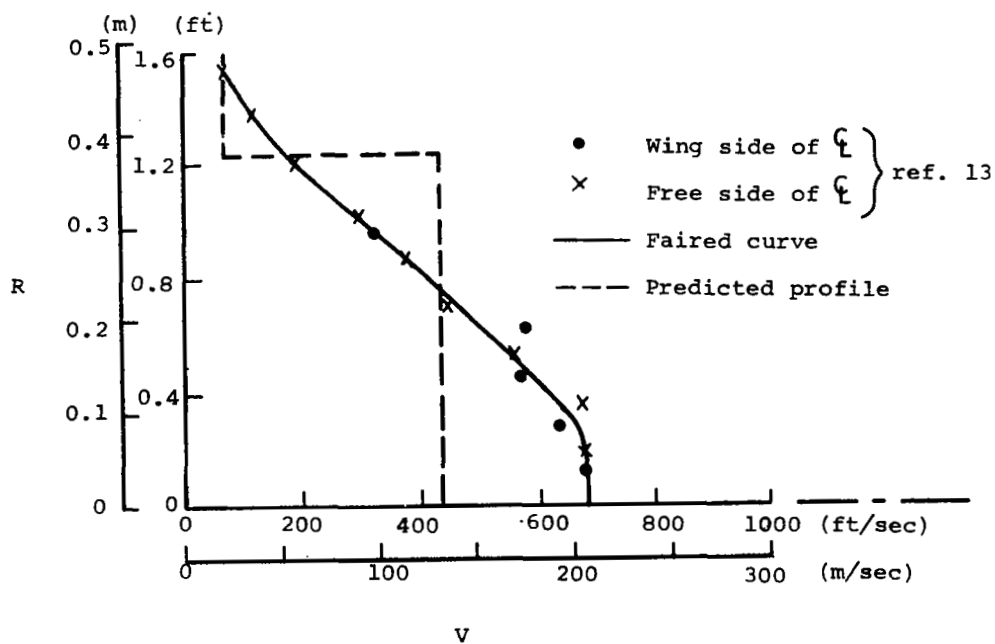
(b) $C_T = 0.564$, T = 3114 newtons (700 pounds).

Figure 19.- Measured and predicted velocity profiles in the wake of a bypass ratio 3 jet engine, q = 297 newton/m² (6.2 lb/ft²).
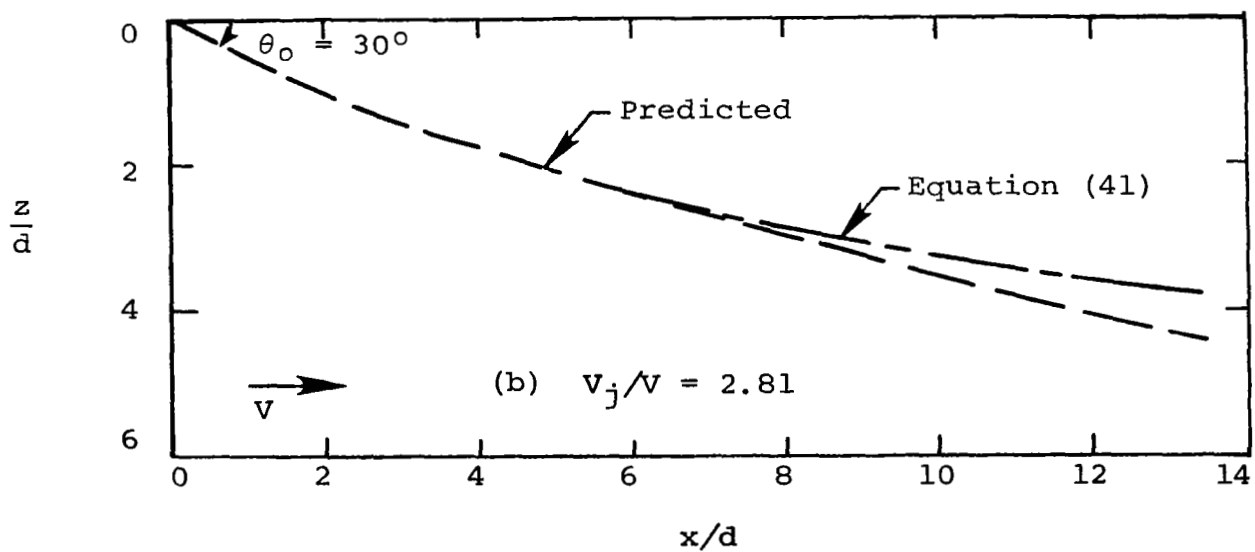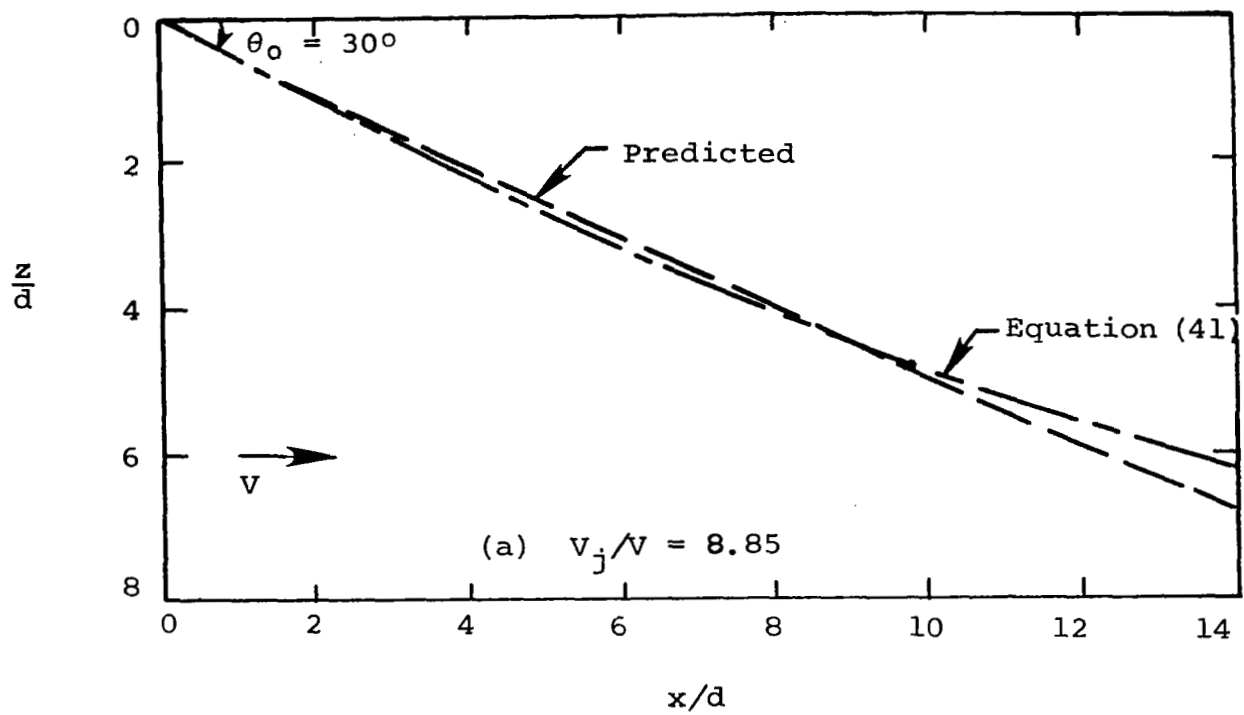
Figure 20.- Comparison of measured and predicted path
of a jet in a crossflow.
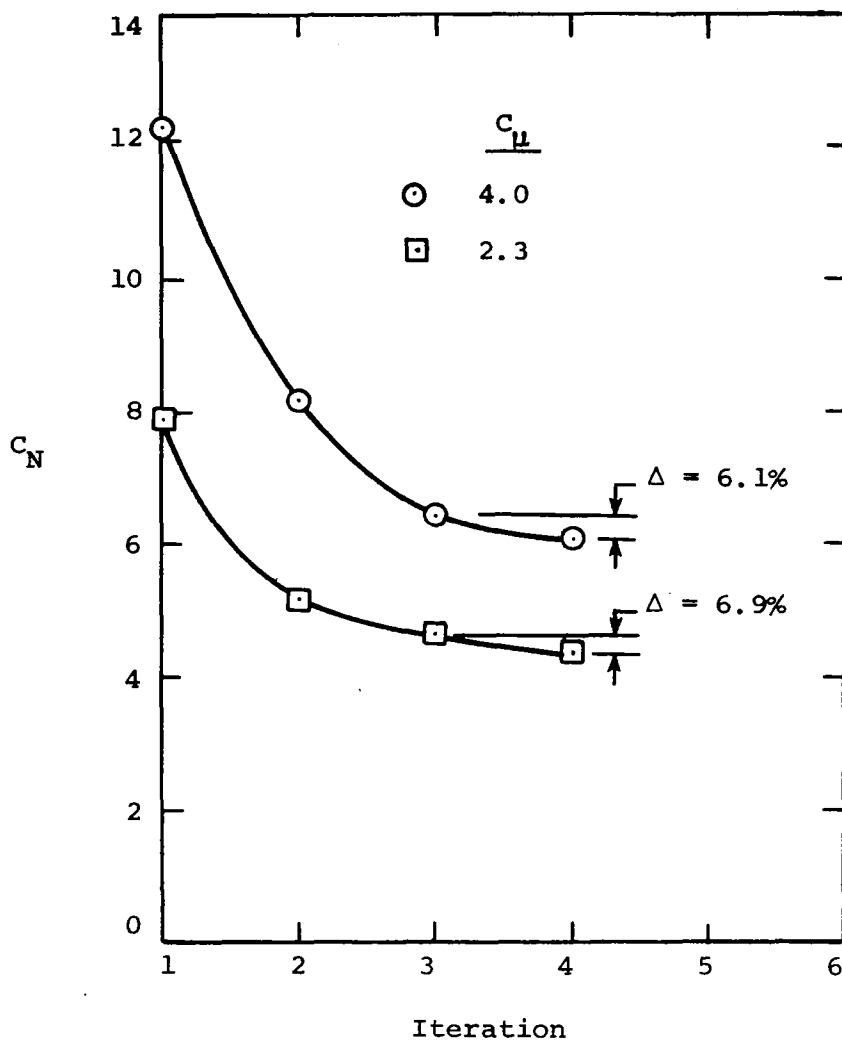
Figure 21.- Convergence of the total wing-flap normal-force coefficient on a four-engine EBF configuration, $\delta_f = 0^\circ /20^\circ /40^\circ$, $\alpha = 18.5^\circ$.
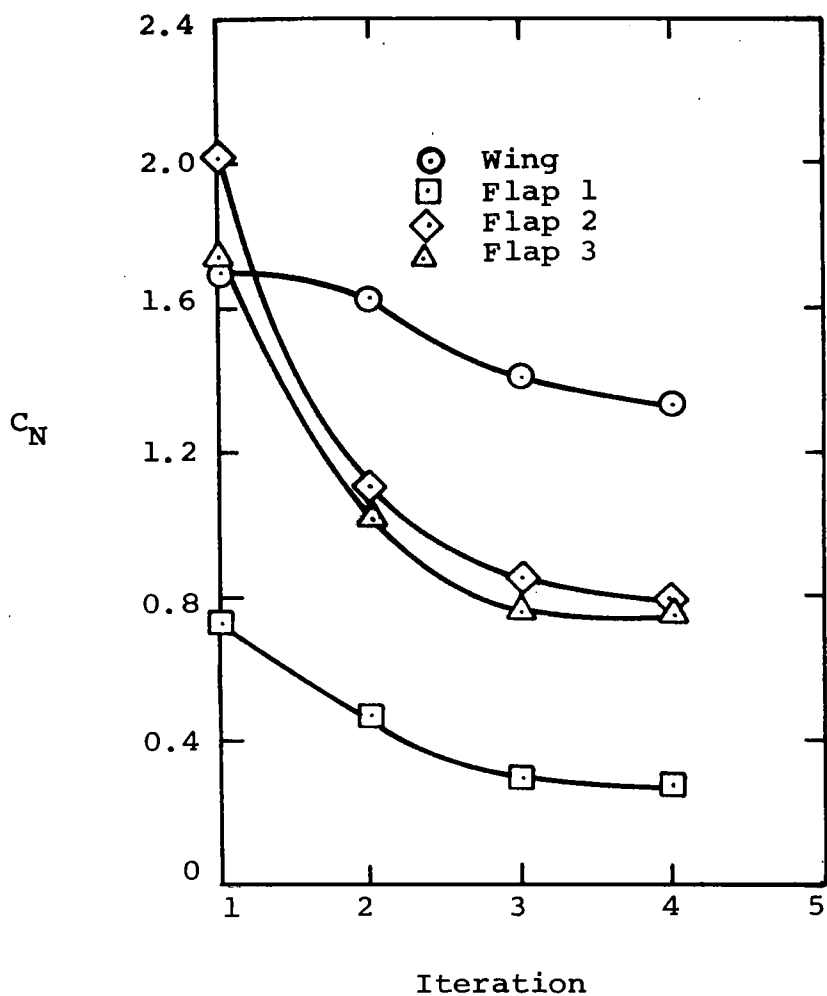
Figure 22.- Convergence of normal-force coefficients on the wing and flaps of a four-engine EBF configuration, $\delta_f = 0°/20°/40°$, $\alpha = 18.5°$, $C_\mu = 4.0$.

(a) Wing.
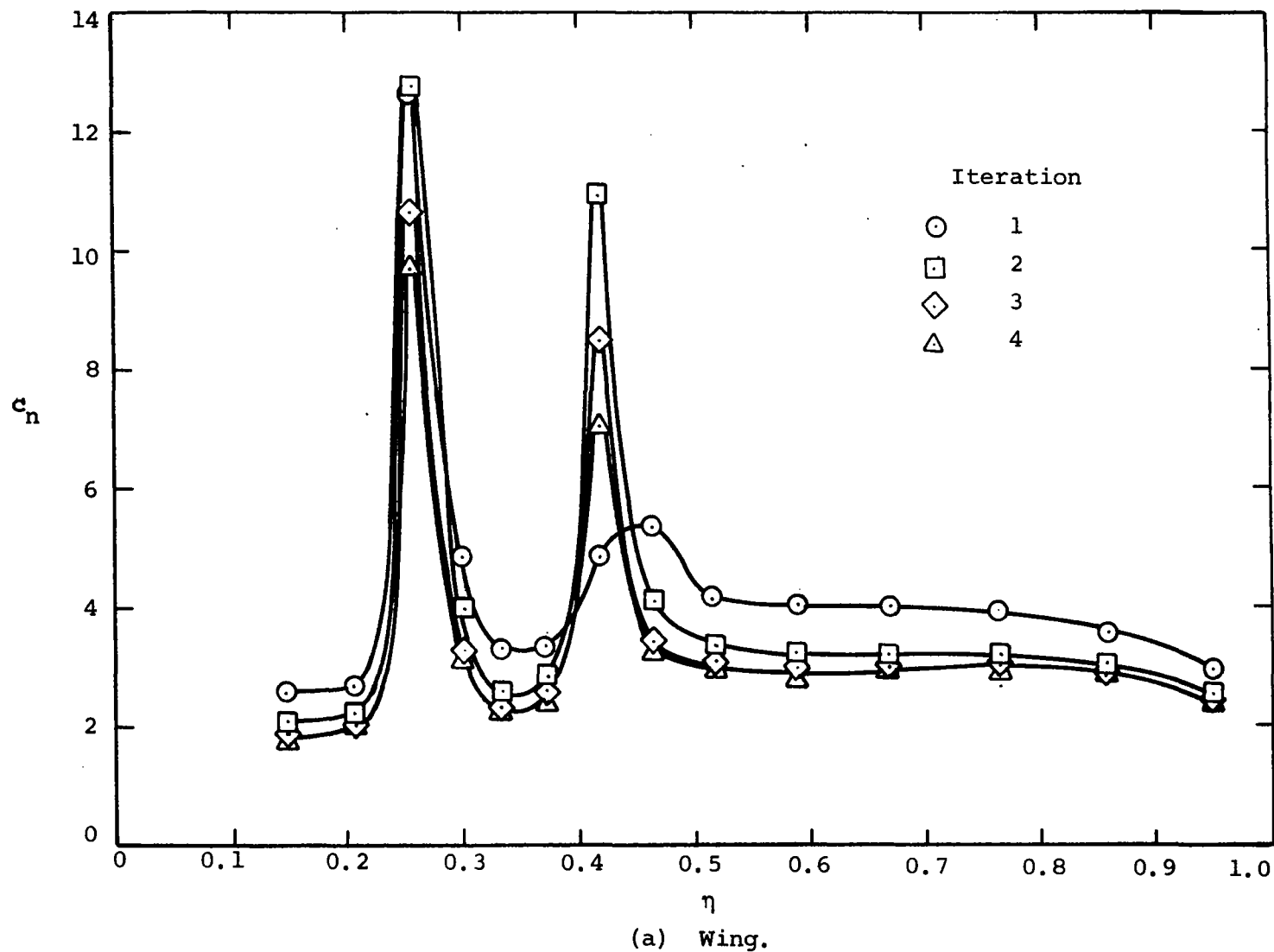
Figure 23.- Convergence of predicted spanwise distribution of section normal-force coefficients on a four-engine EBF configuration, $\delta_f = 0°/20°/40°$, $C_\mu = 4.0$, $\alpha = 18.5°$.
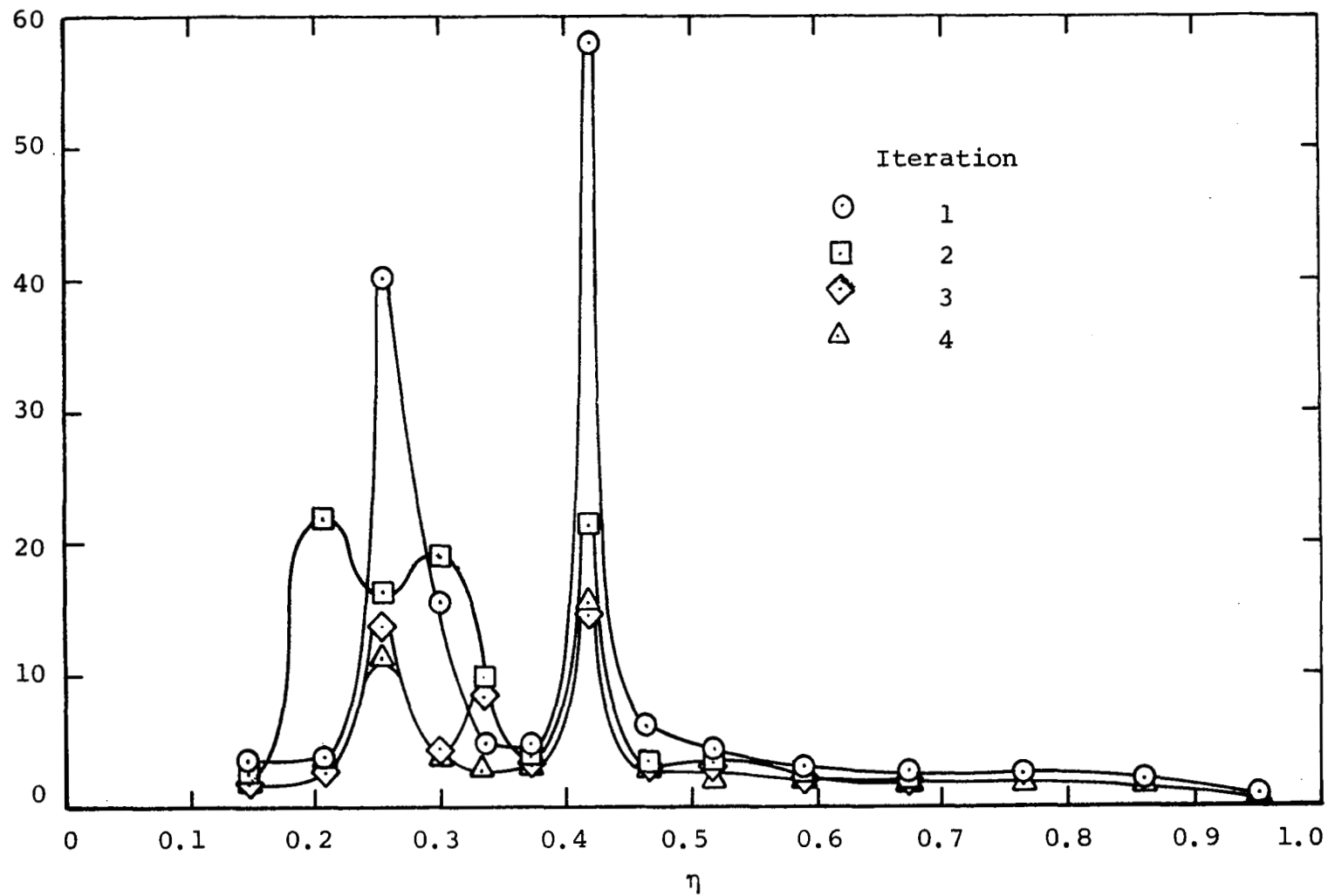
(b) Flap 1, $\delta_{f_1} = 0°$.

Figure 23.- Continued.
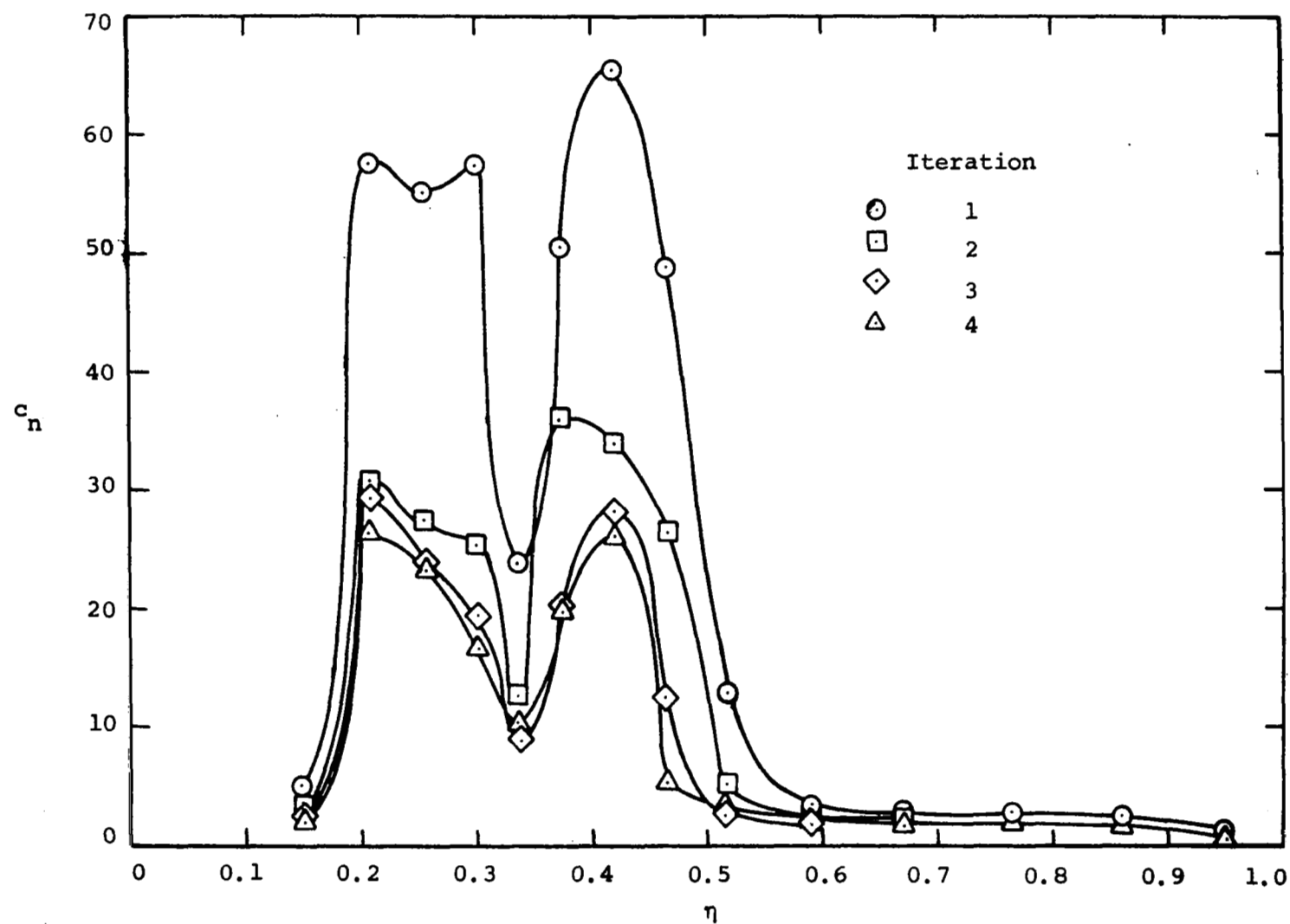
(c) Flap 2, $\delta_{f_2} = 20^{\Omega}$.

Figure 23.- Continued.
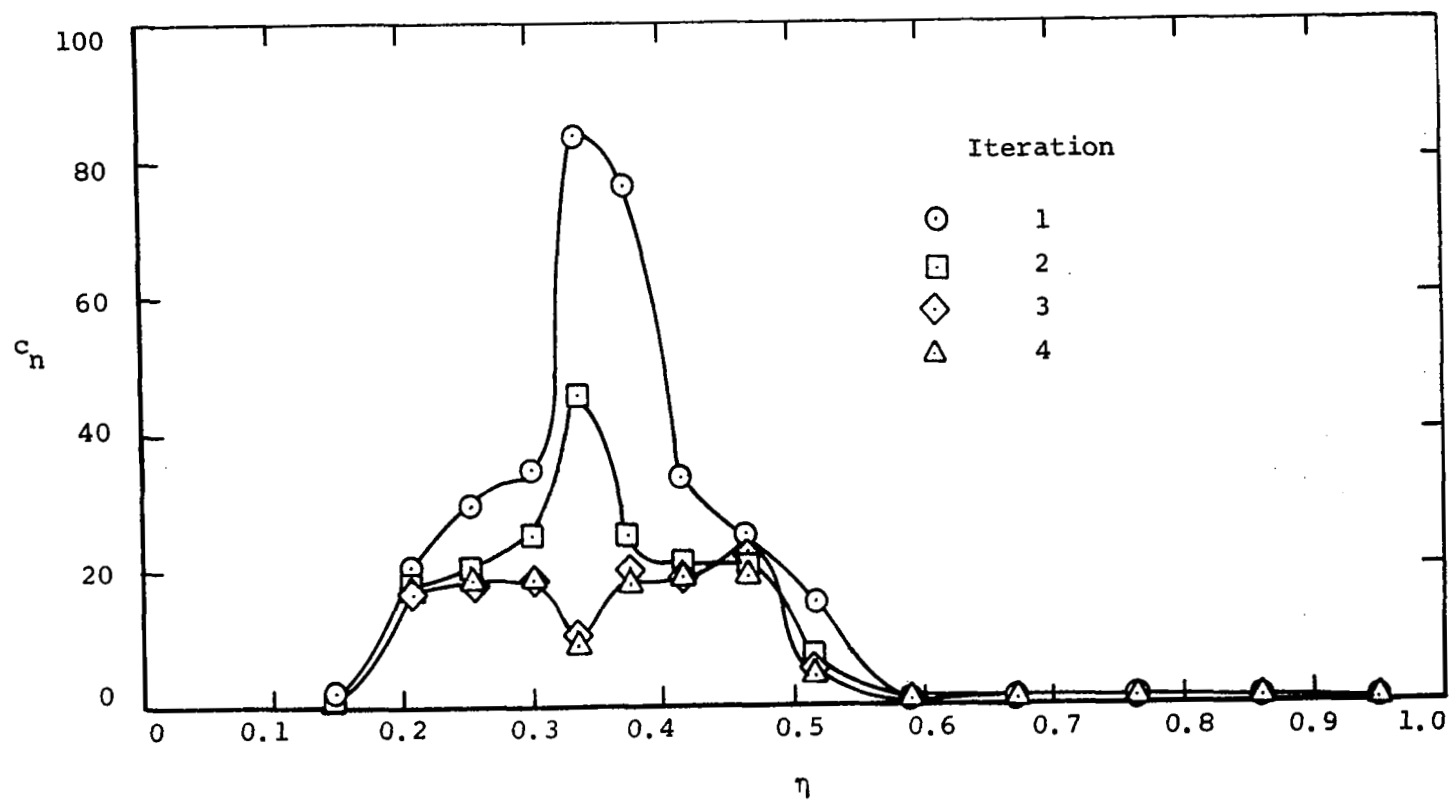
(d) Flap 3, $\delta_{f_3} = 40^\circ$.

Figure 23.- Concluded.

(a)   Inboard jet, $\bar{\eta}$ = 0.25.
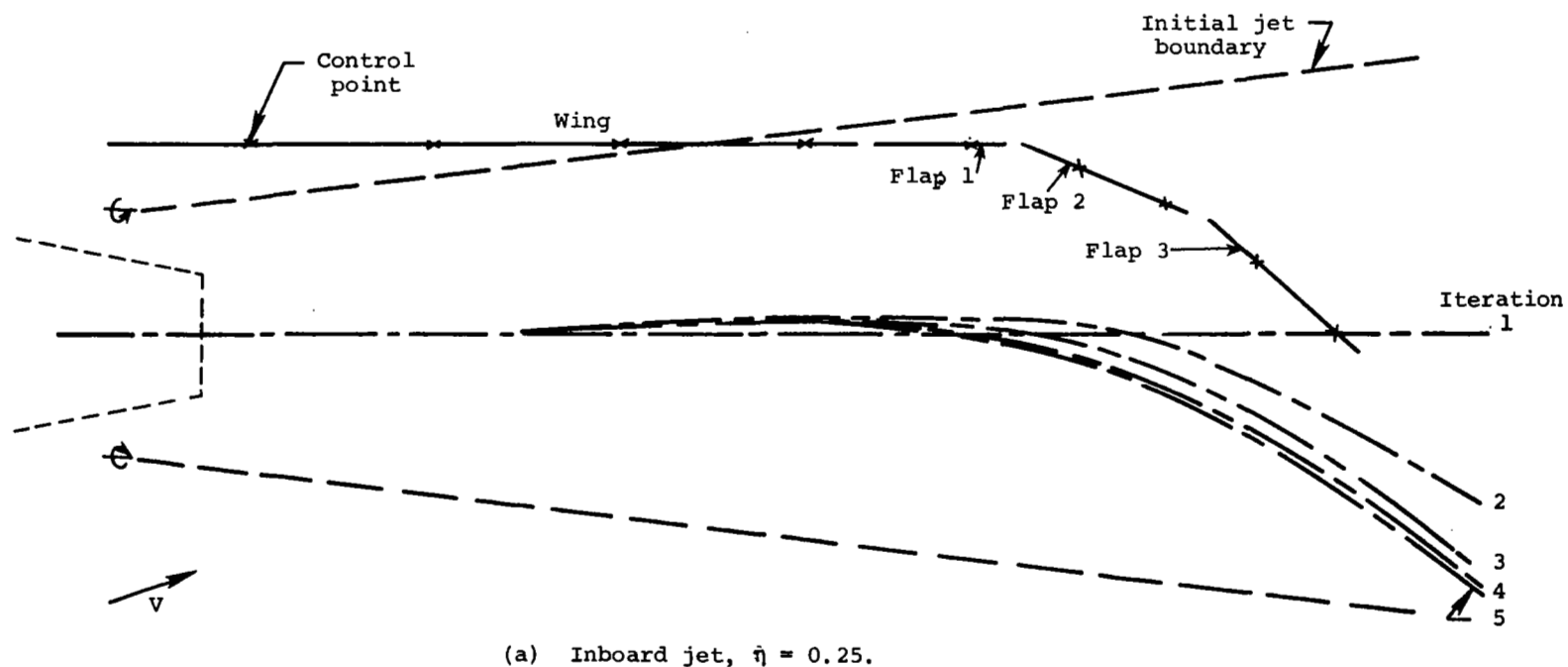
Figure 24.- Convergence of jet centerlines on a four-engine EBF
configuration, δ_f = 0°/20°/40°, C_μ = 4.0, α = 18.5°.
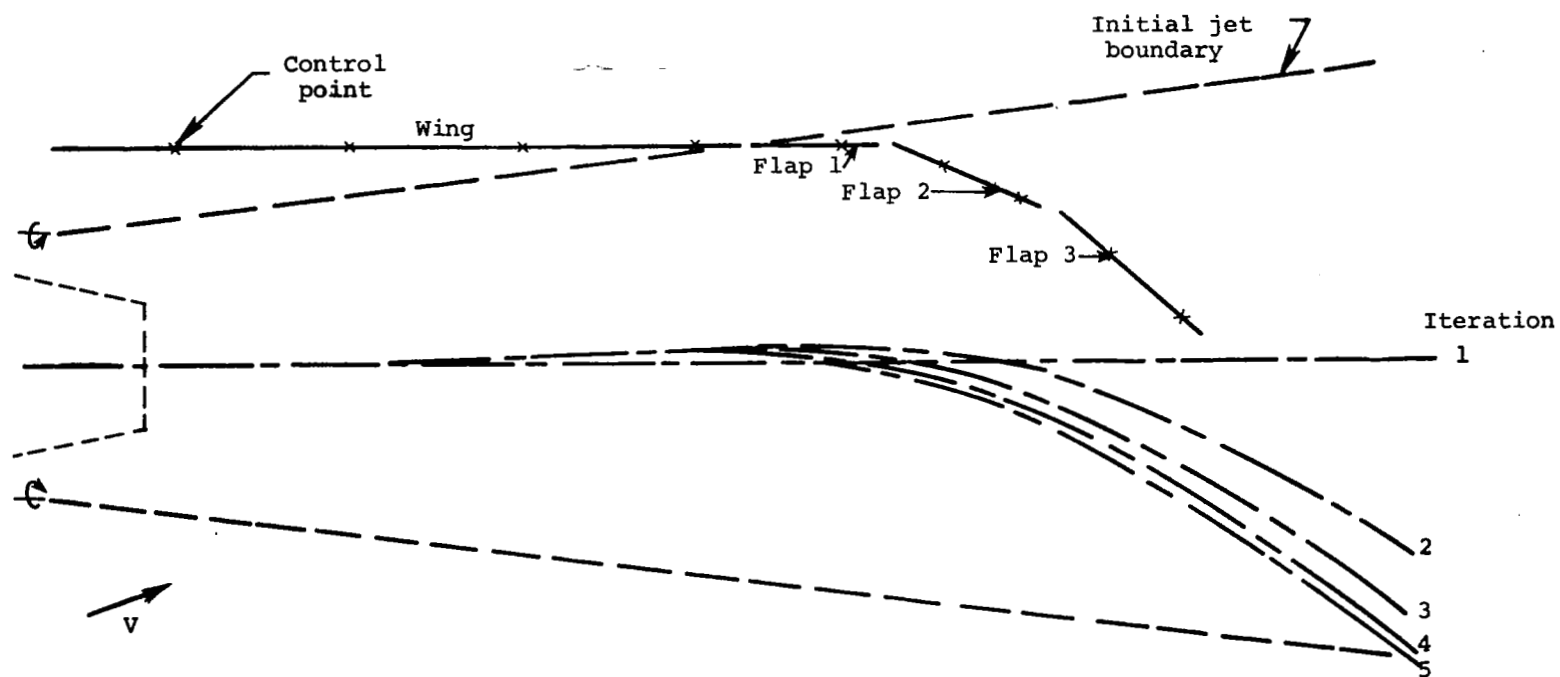
(b) Outboard jet, $\eta = 0.42$.

Figure 24.- Concluded.
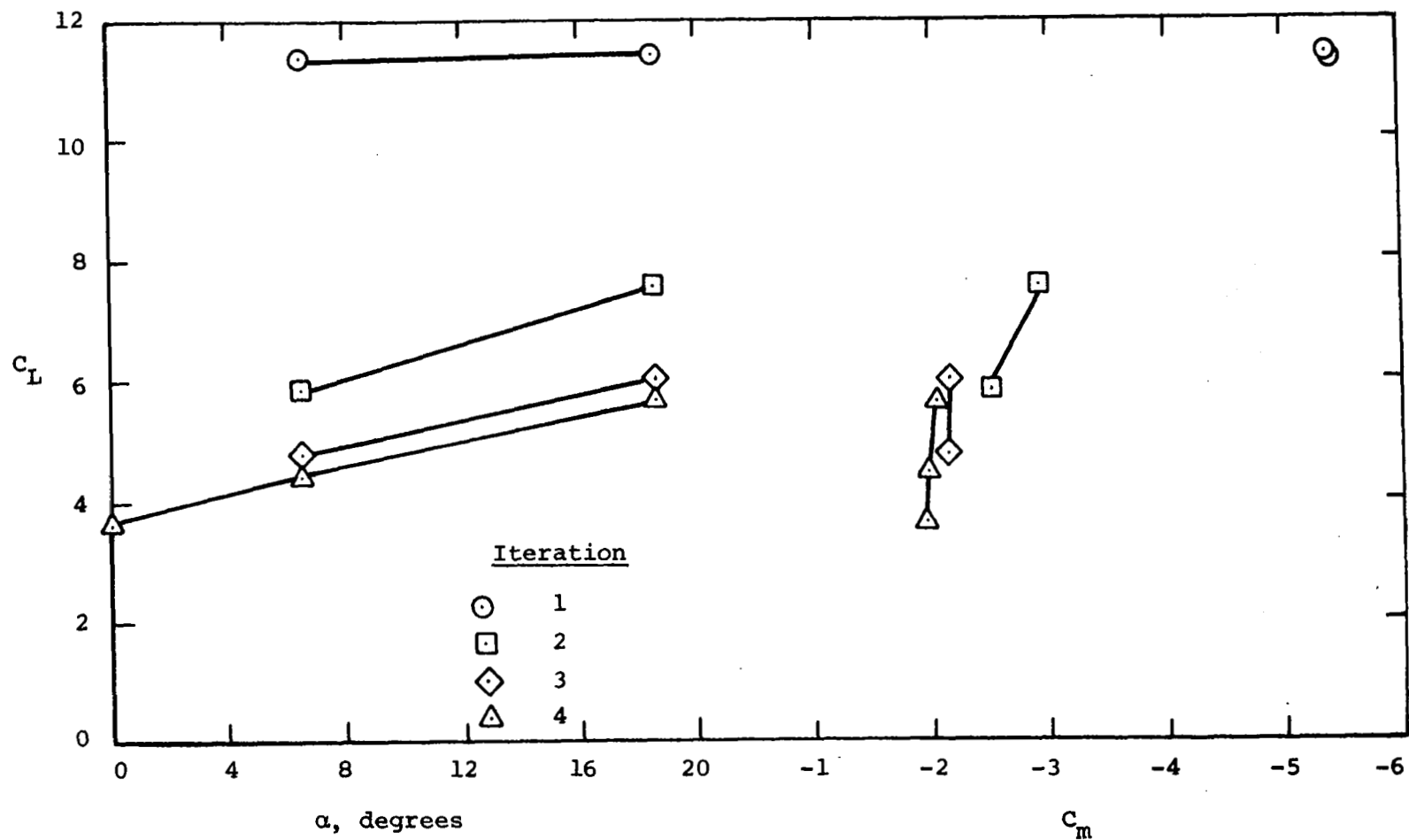
Figure 25.- Convergence of predicted lift and pitching-moment coefficients on a four-engine EBF configuration, $\delta_f = 0°/20°/40°$, $C_\mu = 4.0$.
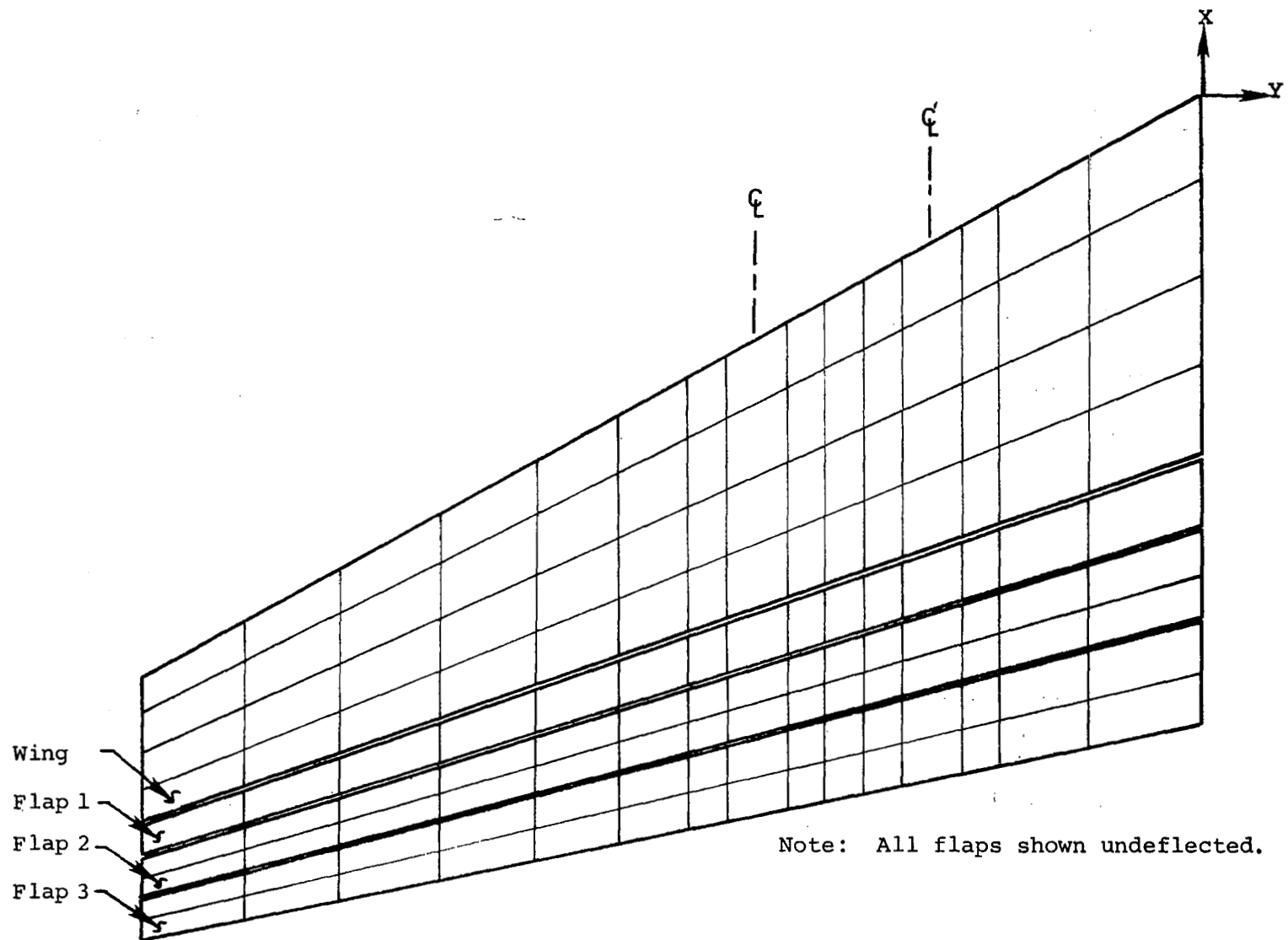
Figure 26.- Vortex lattice arrangement for EBF
configuration of reference 13.
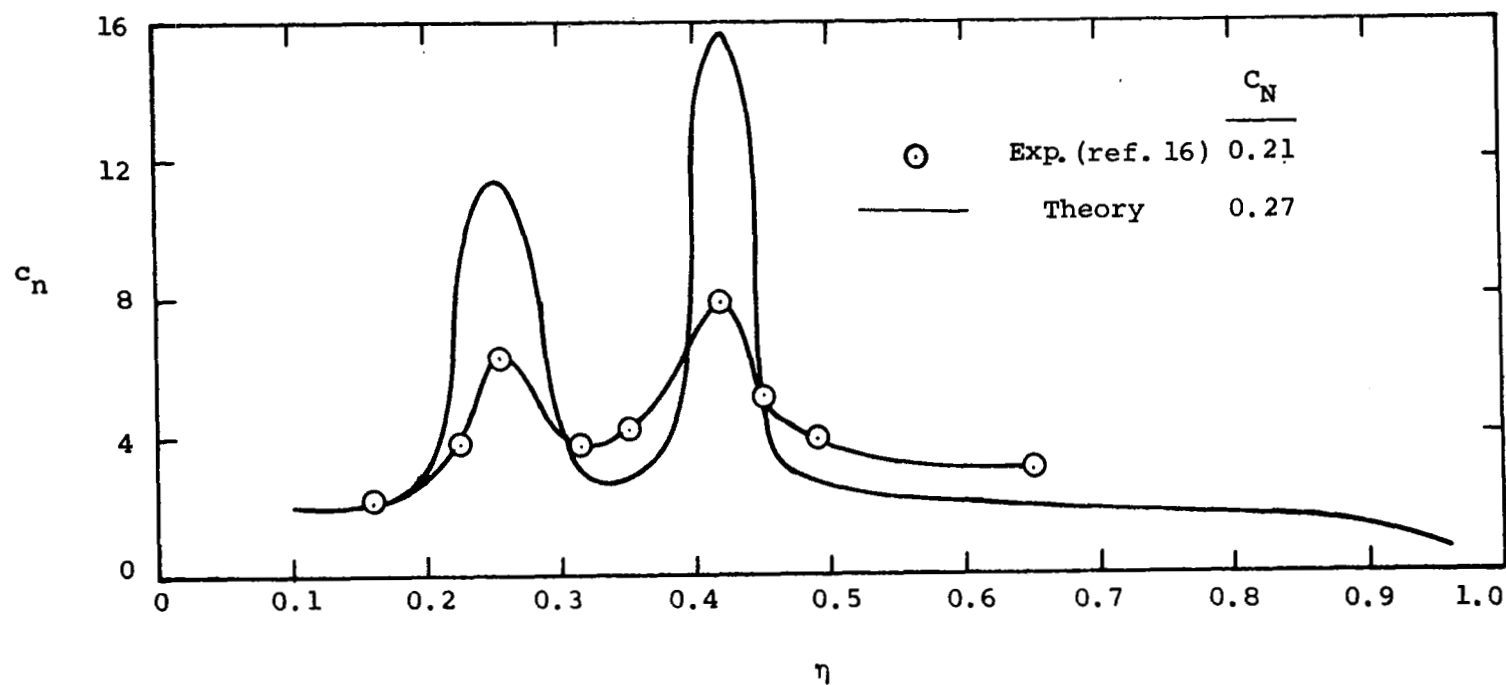
(a)   Flap 1.

Figure 27.– Measured and predicted section normal-force coefficients on the lifting surfaces of a four-engine EBF model, $\delta_f = 0^\circ/20^\circ/40^\circ$, $C_\mu = 4.0$, $\alpha = 18.5^\circ$.
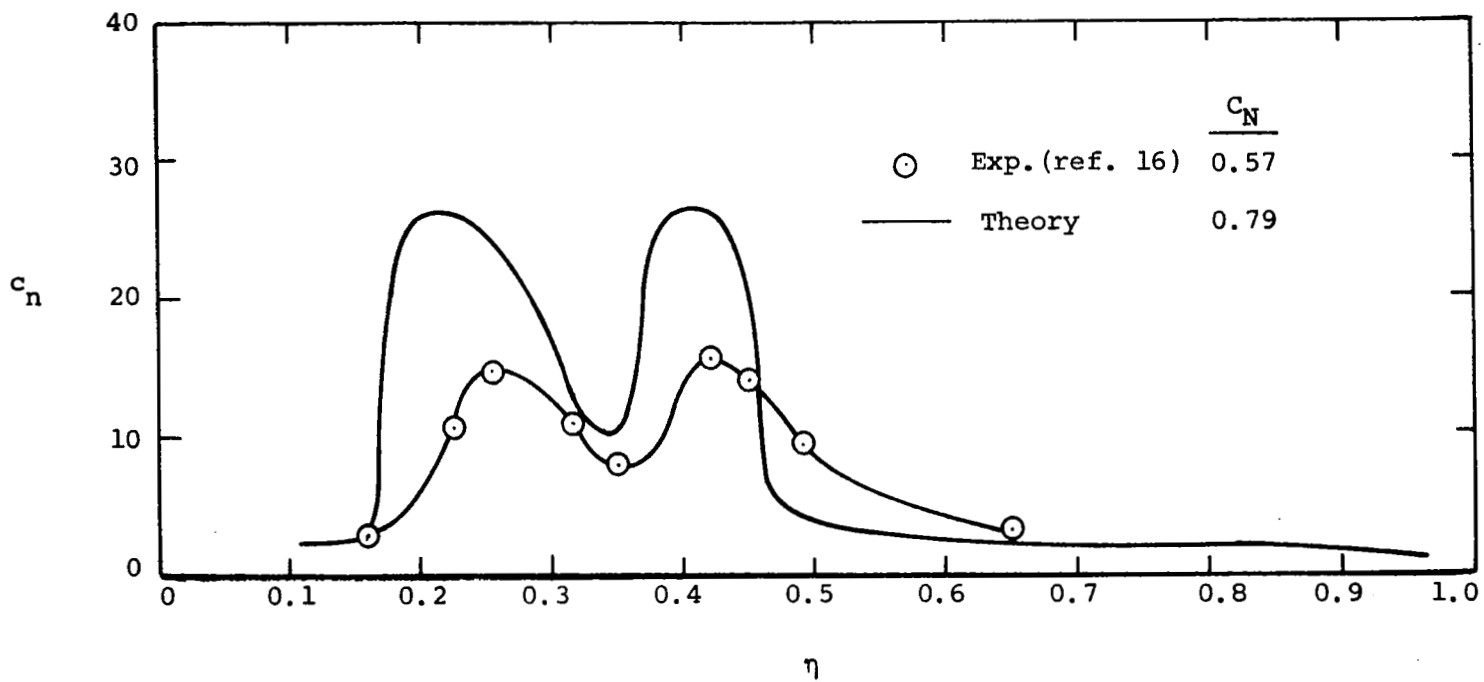
(b) Flap 2.

Figure 27.- Continued.
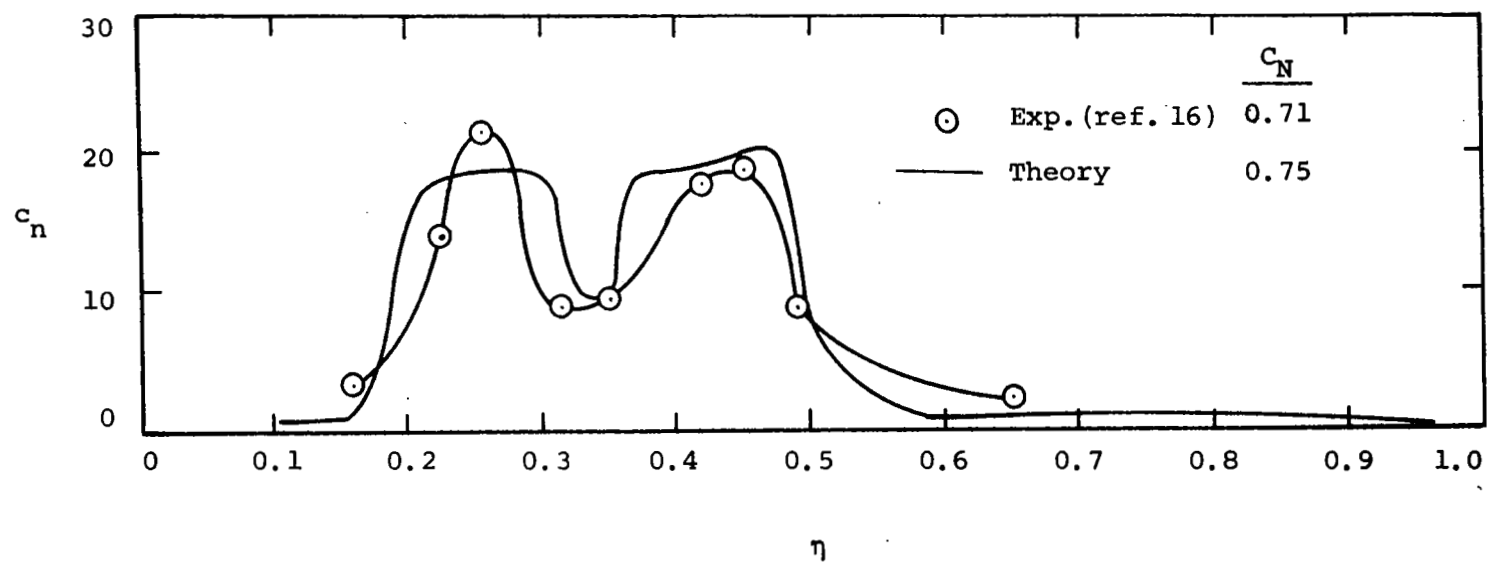
(c) Flap 3.

Figure 27.- Concluded.
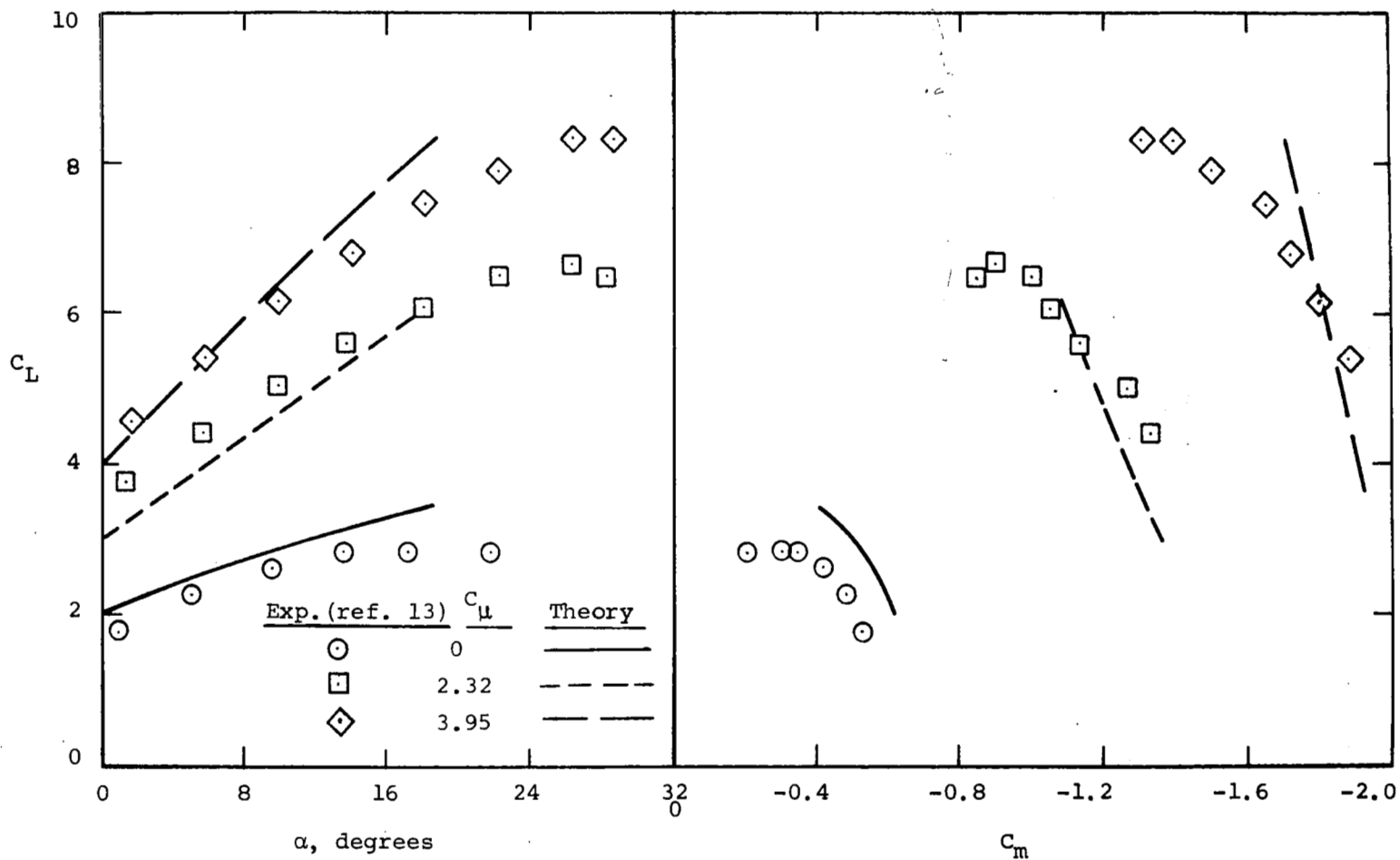
(a) Lift and pitching-moment coefficients.

Figure 28.- Measured and predicted longitudinal aerodynamic characteristics
of a four-engine EBF configuration, $\delta_f = 0°/20°/40°$.
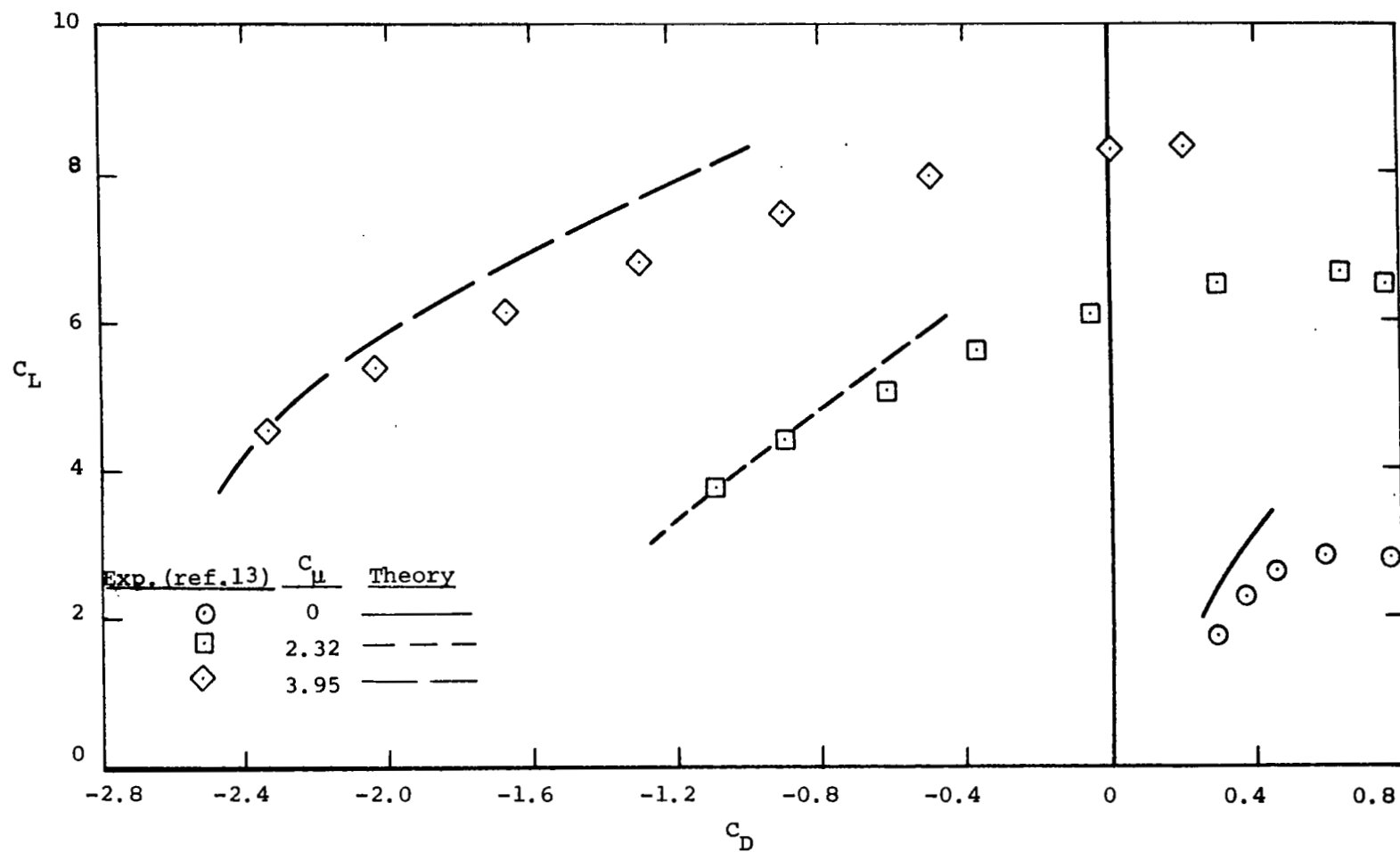
(b) Drag coefficient.

Figure 28.- Concluded.
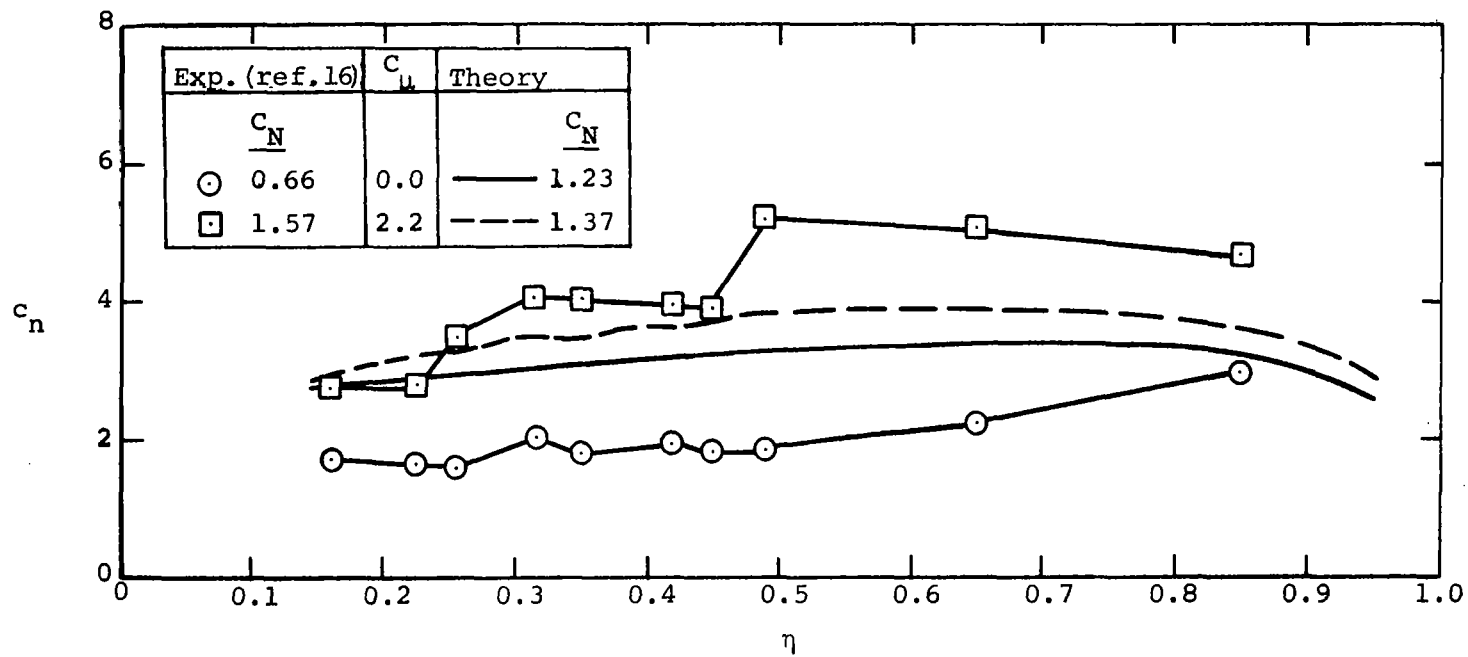
(a) Wing.

Figure 29.- Measured and predicted section normal force coefficients on the lifting surfaces of a four-engine EBF configuration, $\delta_f = 15\%35\%55^\circ$, $\alpha = 18.5^\circ$.
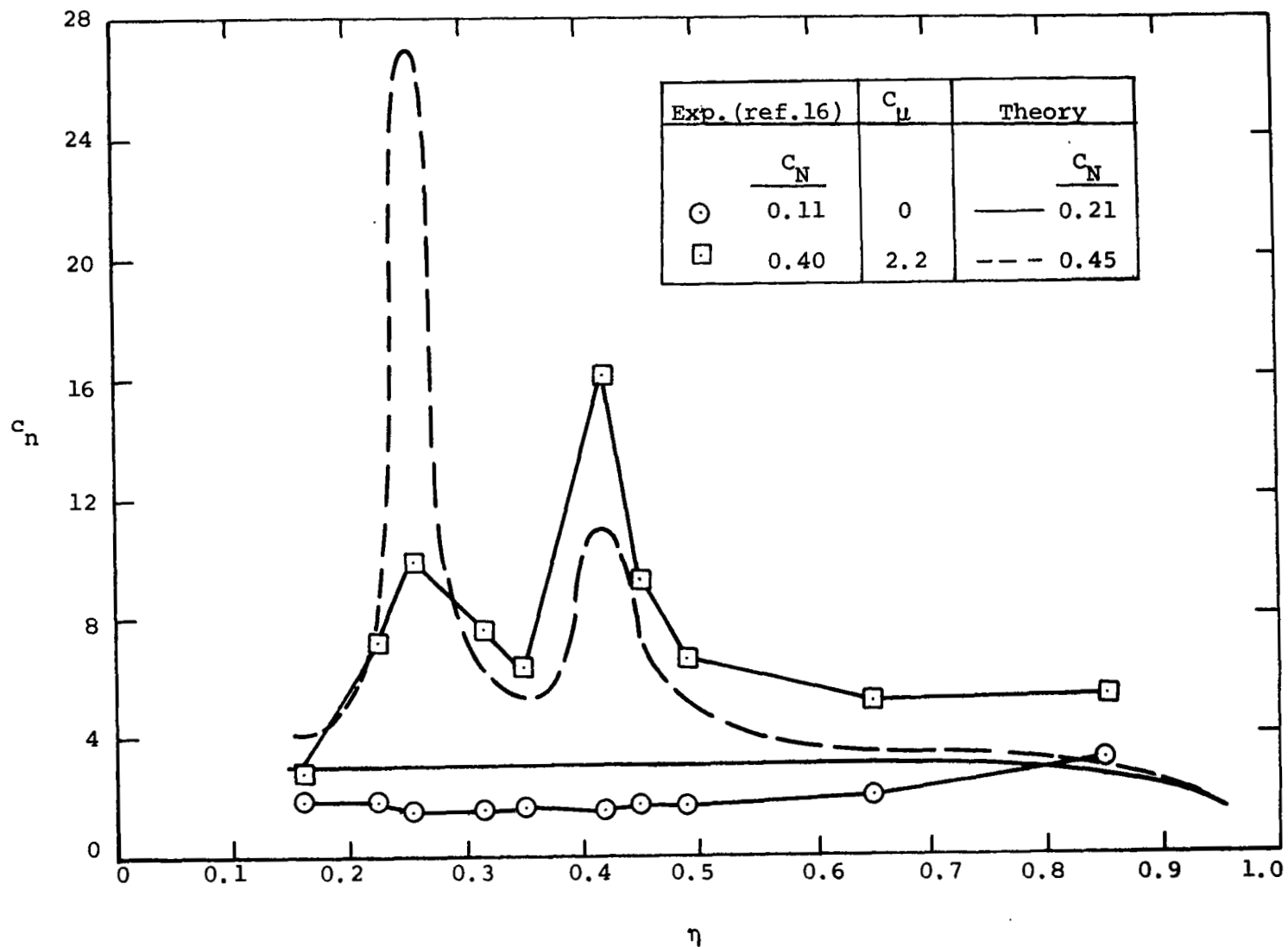
(b)   Flap 1.

Figure 29.- Continued.

40

30

c_n

20

10

0

Exp.(ref.16)	C_μ	Theory
C_N		C_N
⊙ 0.14	0.0	—— 0.21
⊡ 0.74	2.2	— — 0.67

0   0.1   0.2   0.3   0.4   0.5   0.6   0.7   0.8   0.9   1.0

η
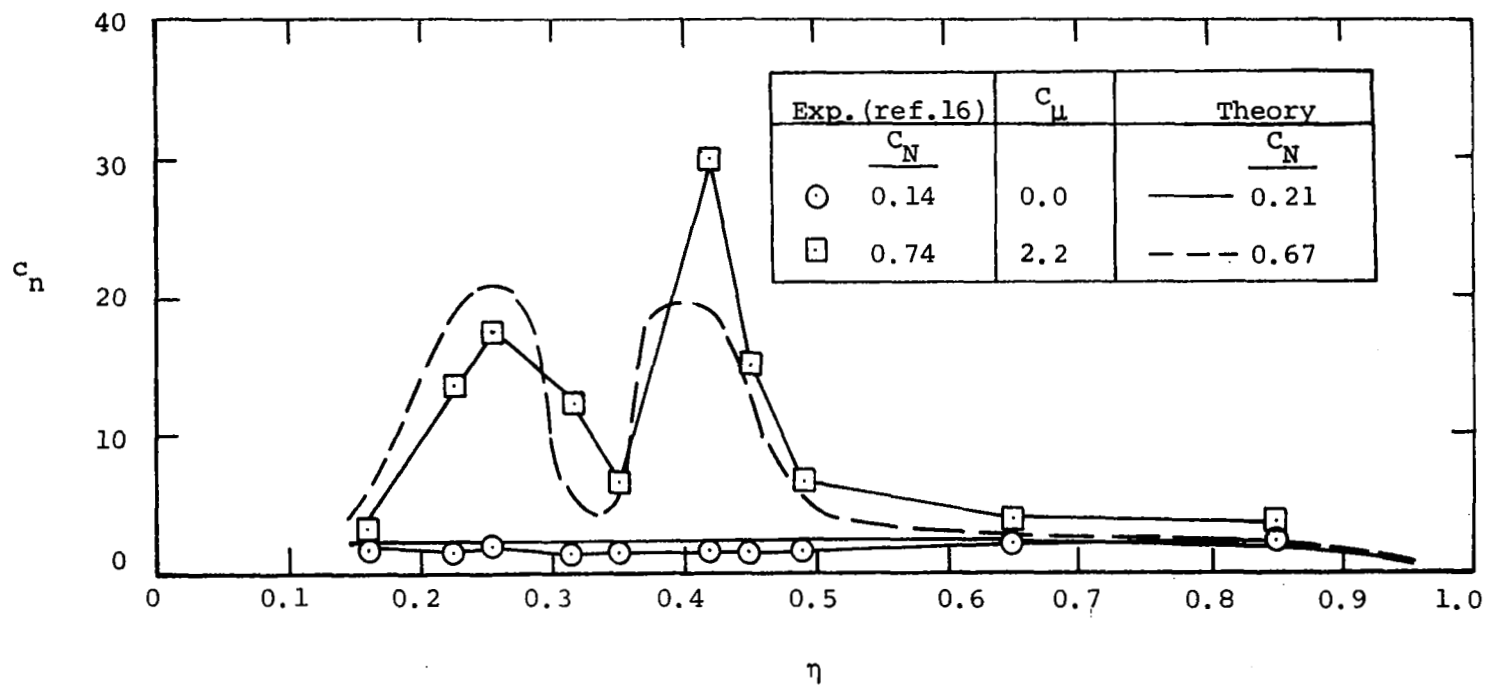
(c) Flap 2.

Figure 29.- Continued.
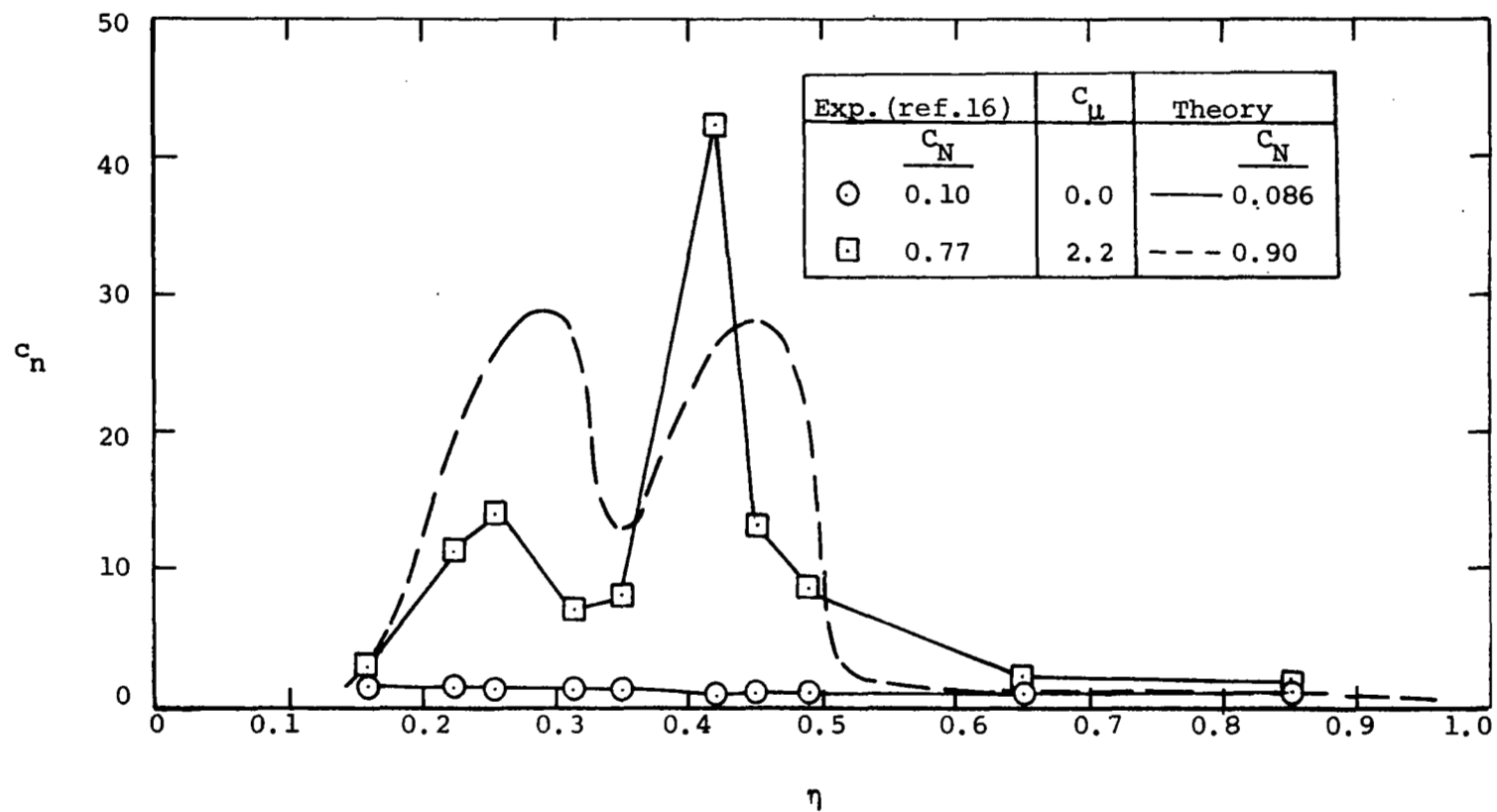
(d) Flap 3.

Figure 29.- Concluded.
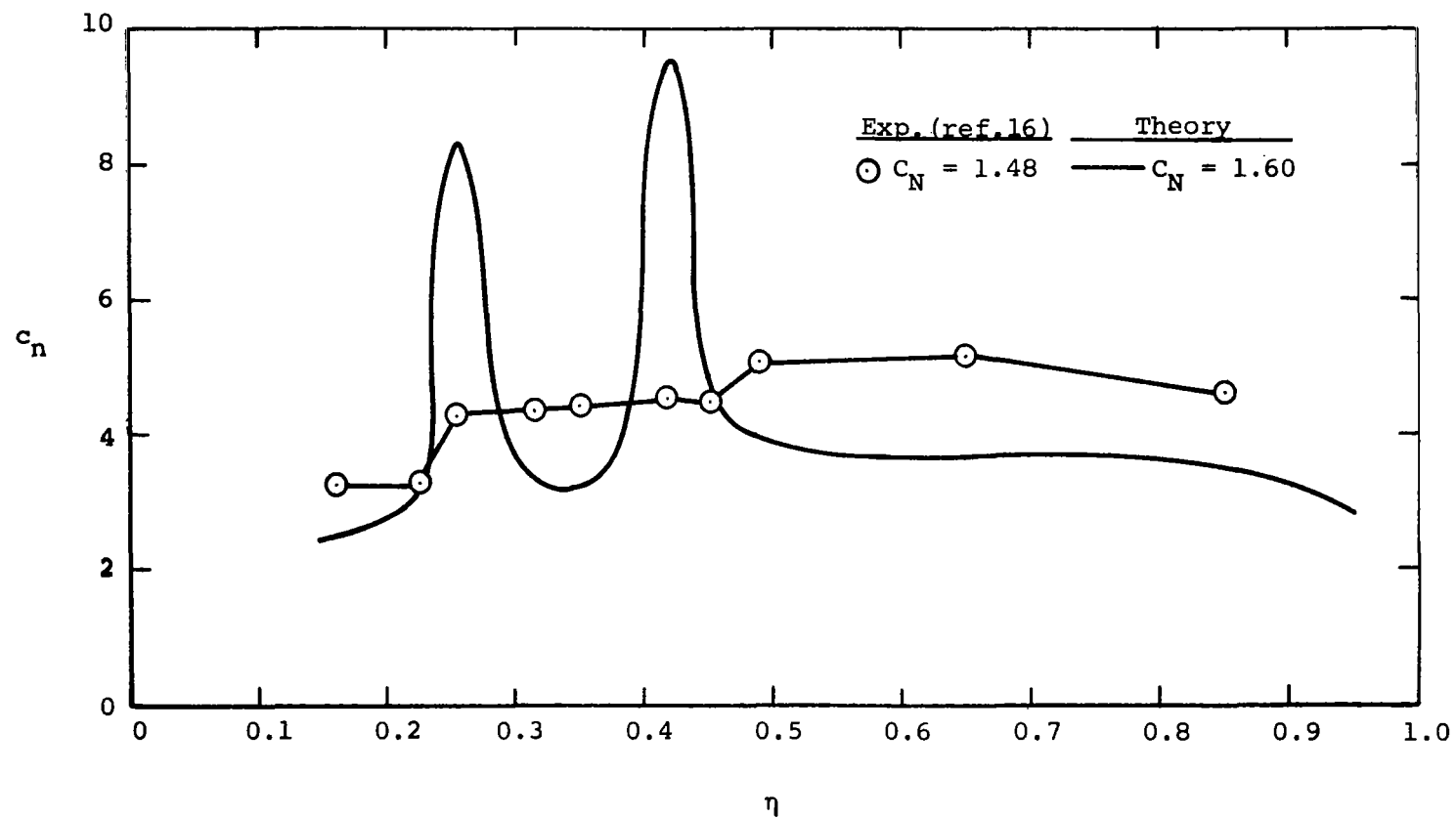
(a) Wing.

Figure 30.- Measured and predicted section normal force coefficients on the lifting surfaces of a four-engine EBF configuration, $\delta_f = 15°/35°/55°$, $C_\mu = 4.0$, $\alpha = 18.5°$.
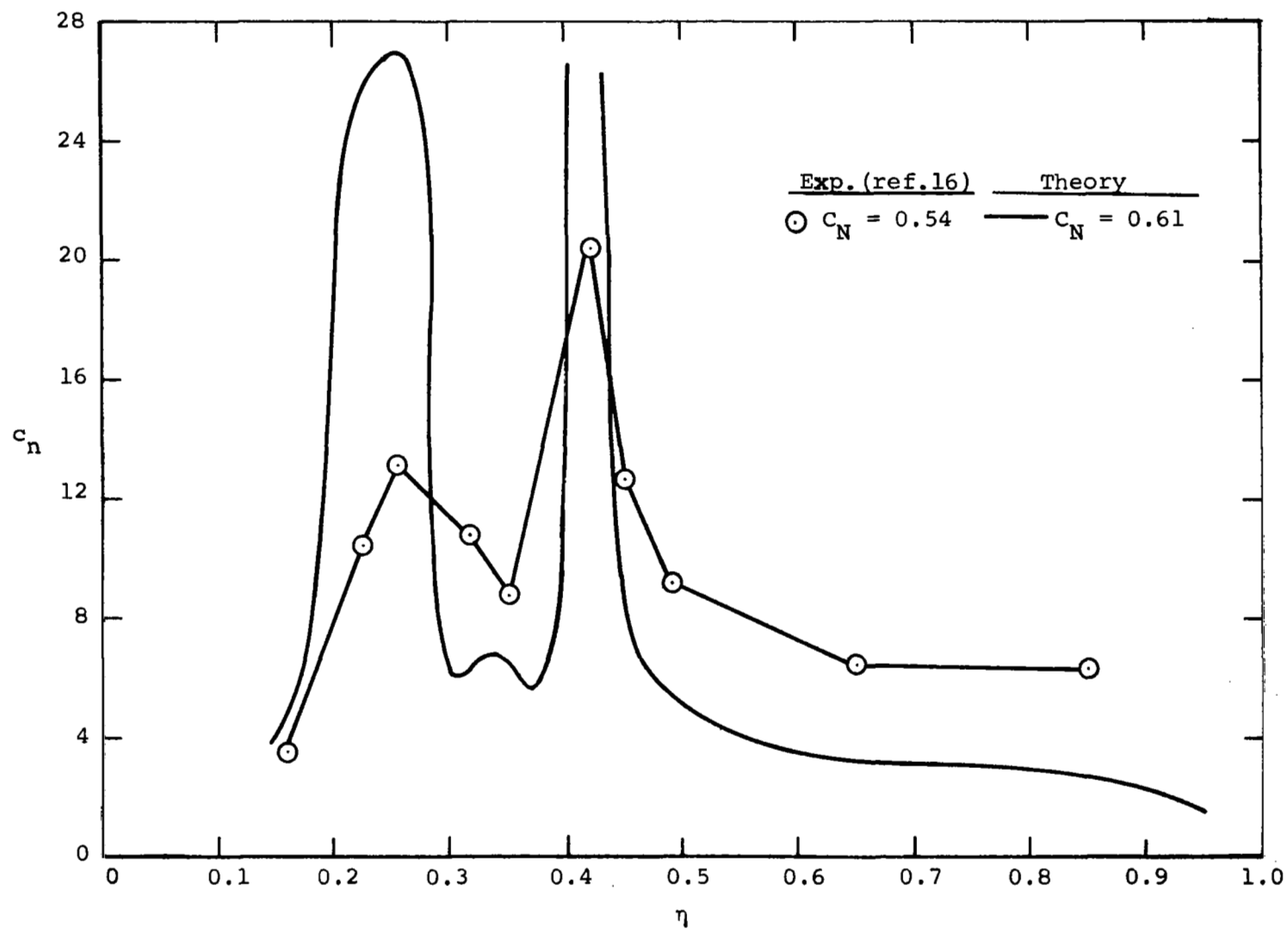
(b) Flap 1.

Figure 30.- Continued.
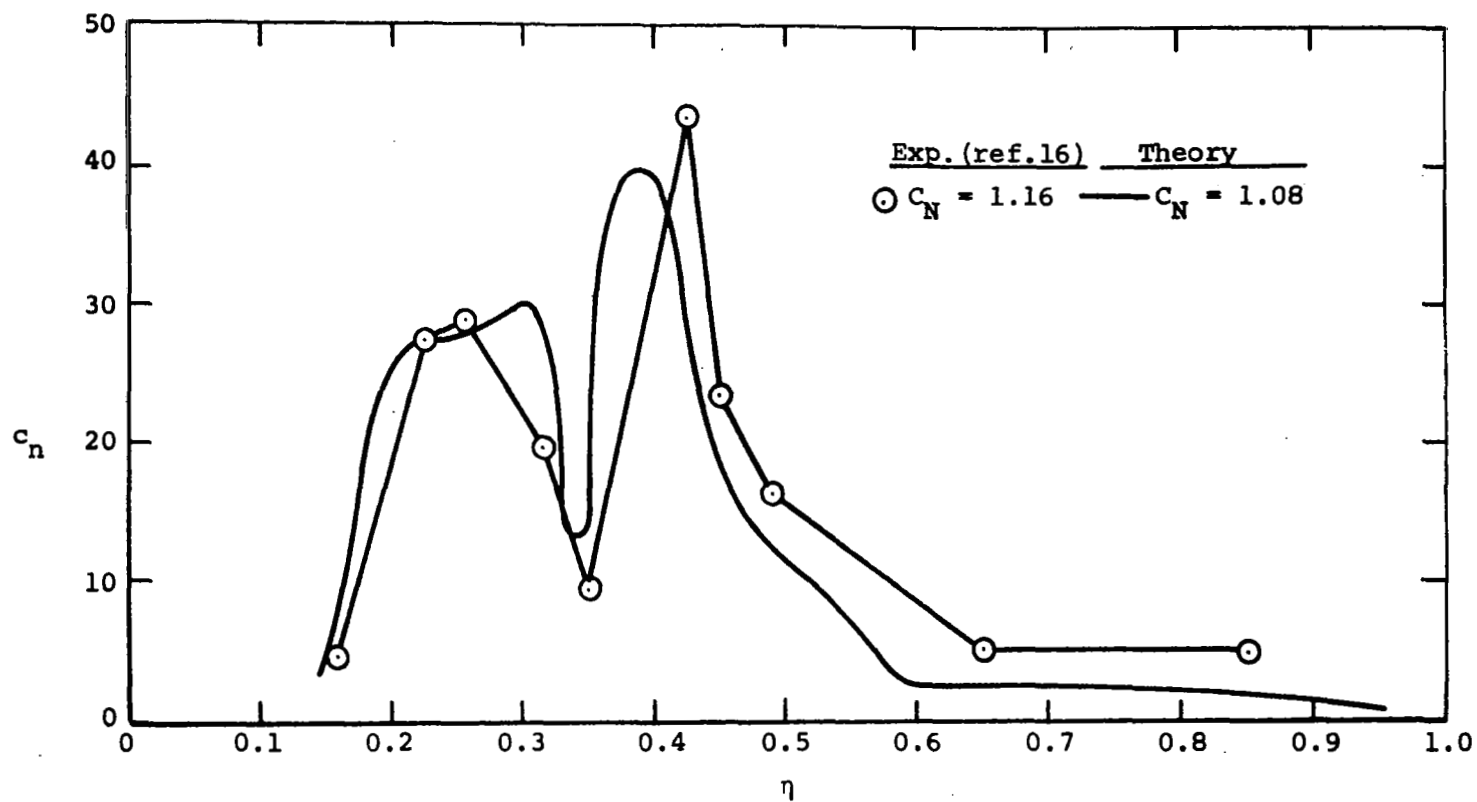
(c) Flap 2.

Figure 30.- Continued.
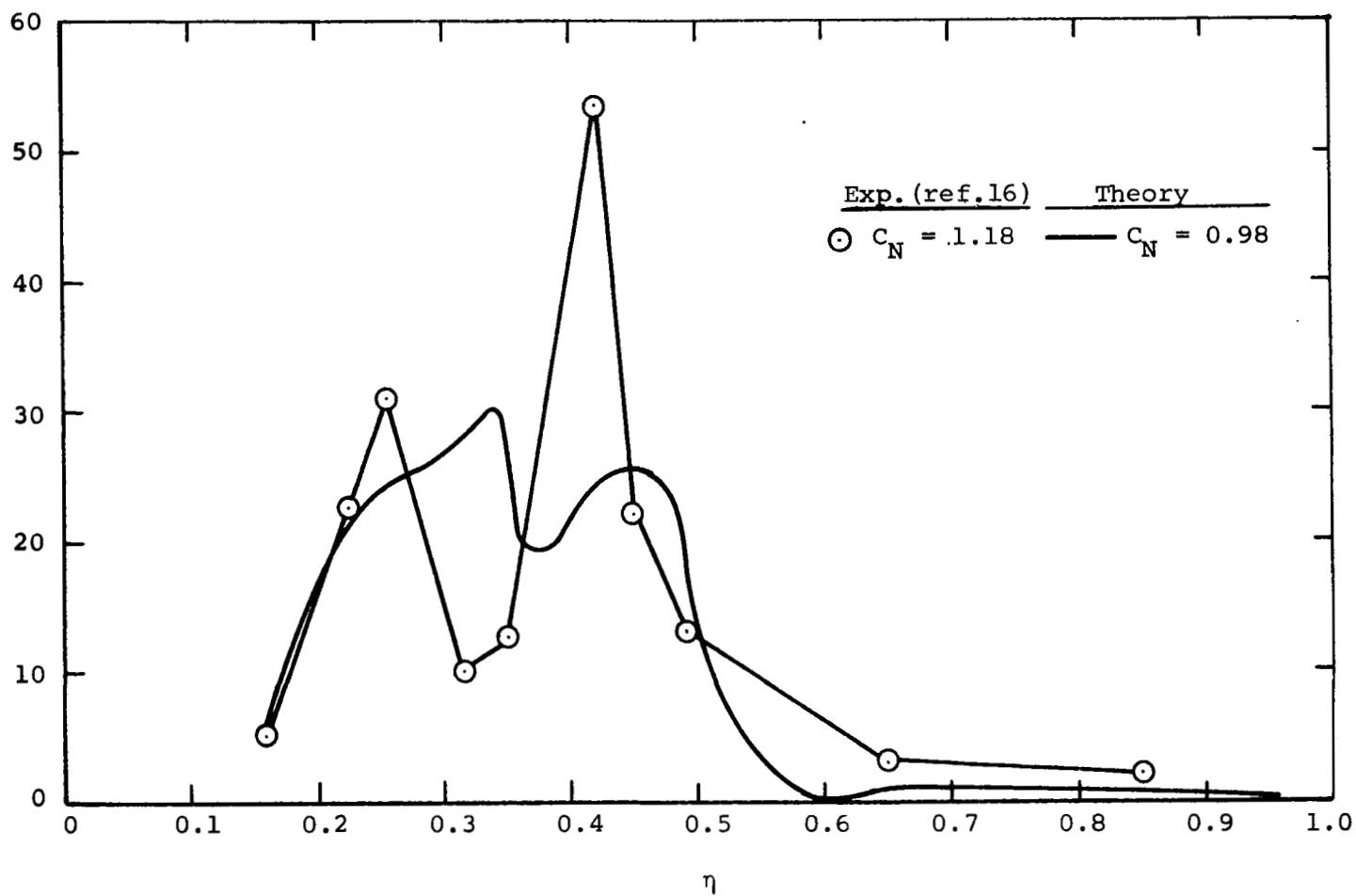
(d) Flap 3.

Figure 30.- Concluded.
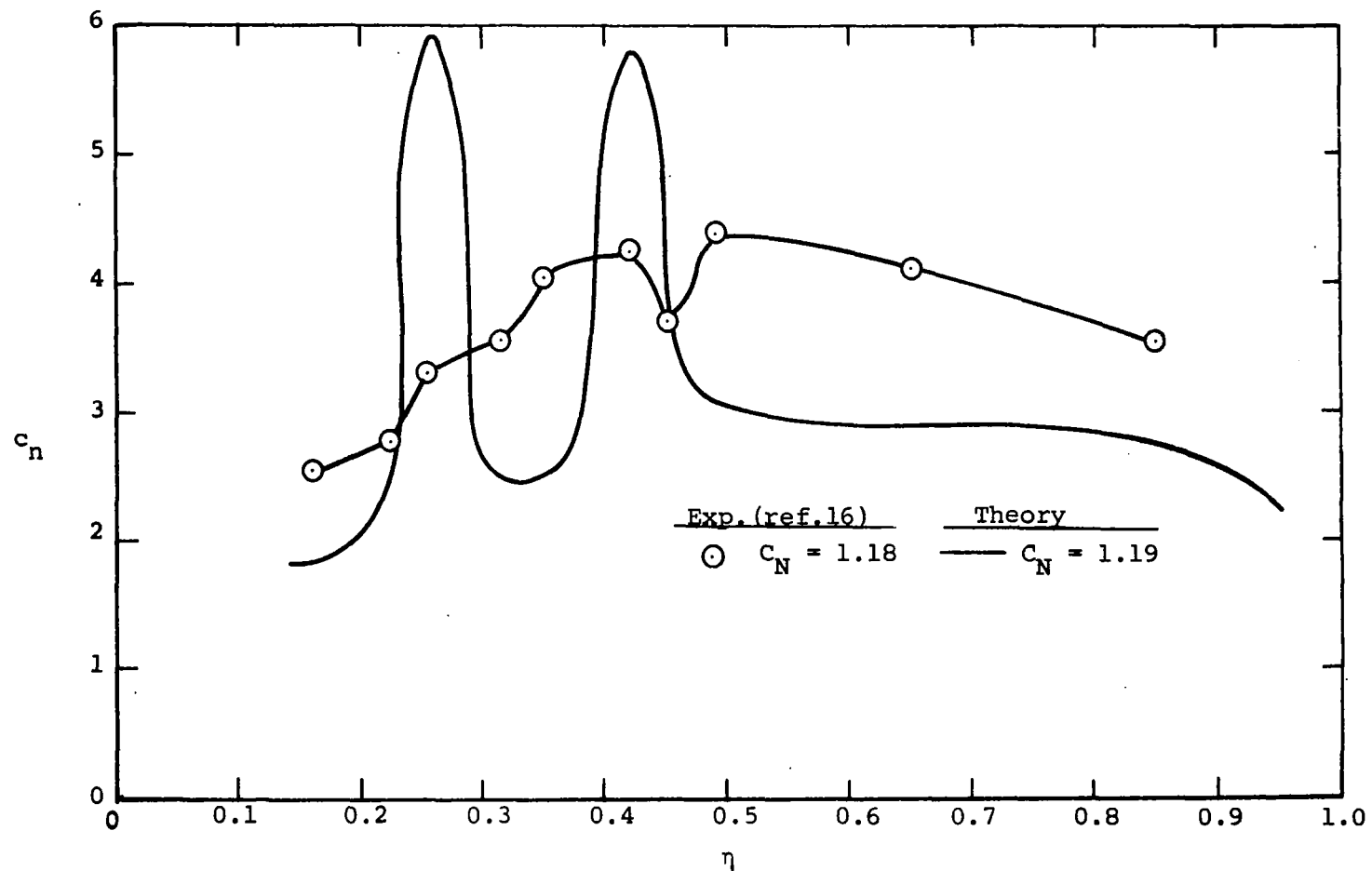
(a) Wing.

Figure 31.- Measured and predicted section normal force coefficients on the lifting surfaces of a four-engine EBF configuration, $\delta_f = 15°/35°/55°$, $C_\mu = 4.0$, $\alpha = 6.5°$.
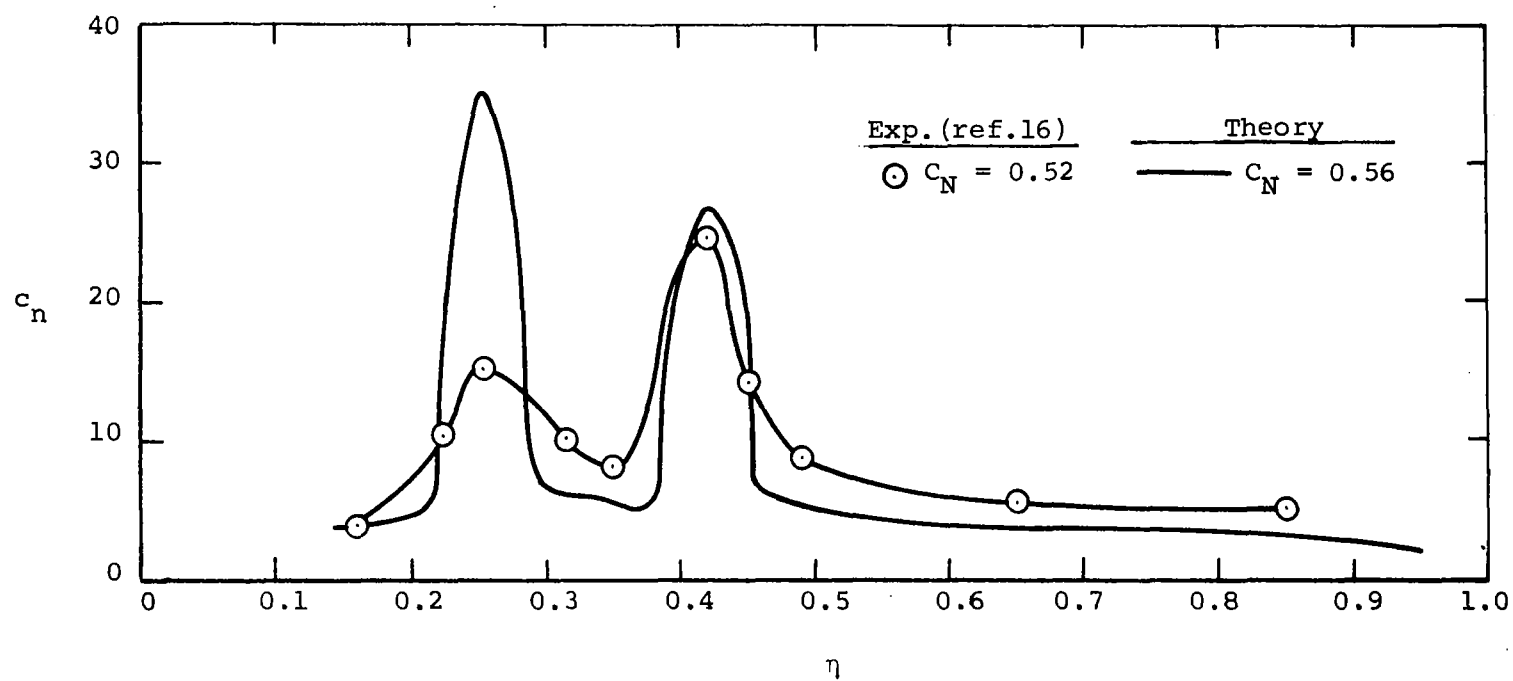
(b) Flap 1.

Figure 31.- Continued.
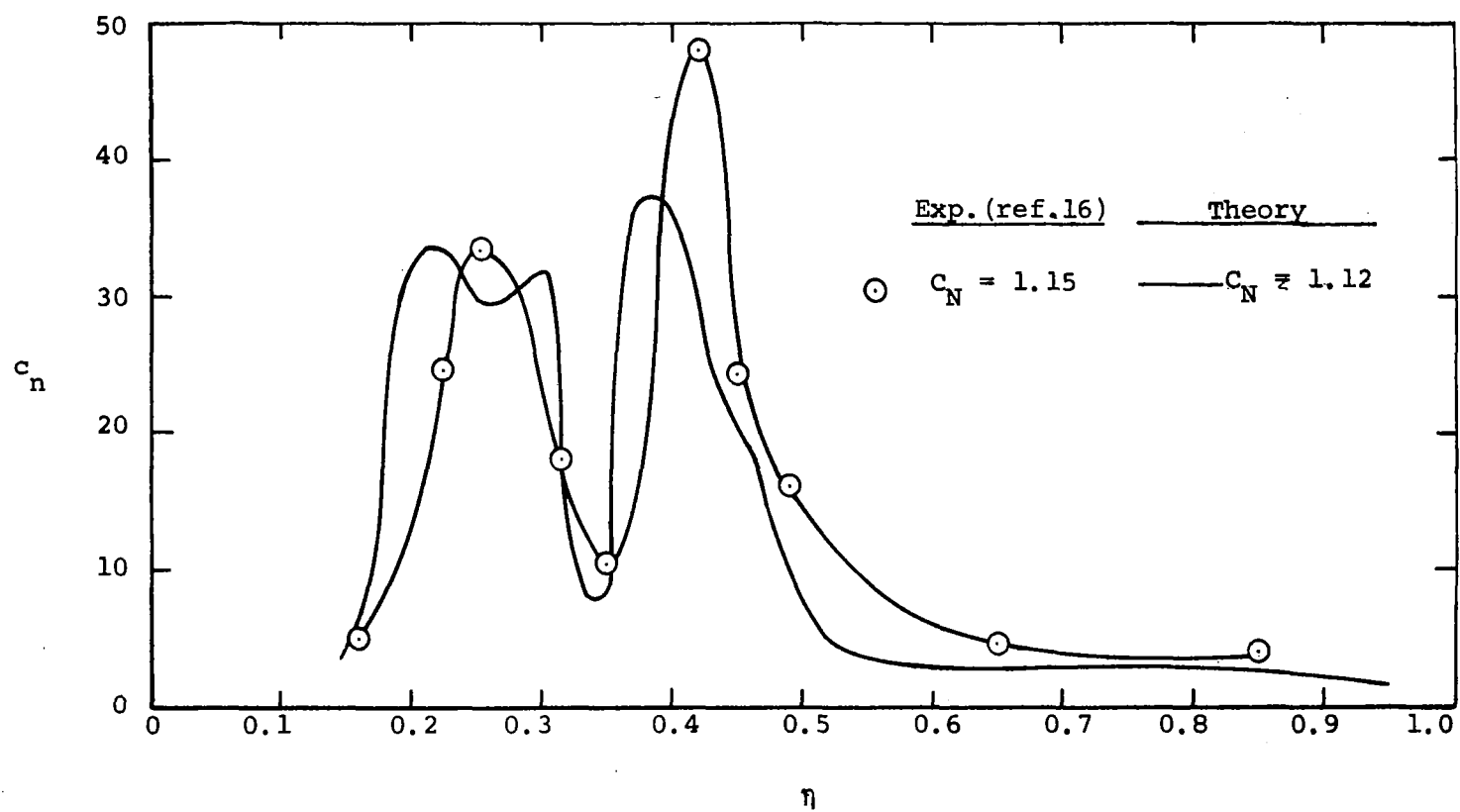
(c) Flap 2.

Figure 31.- Continued.
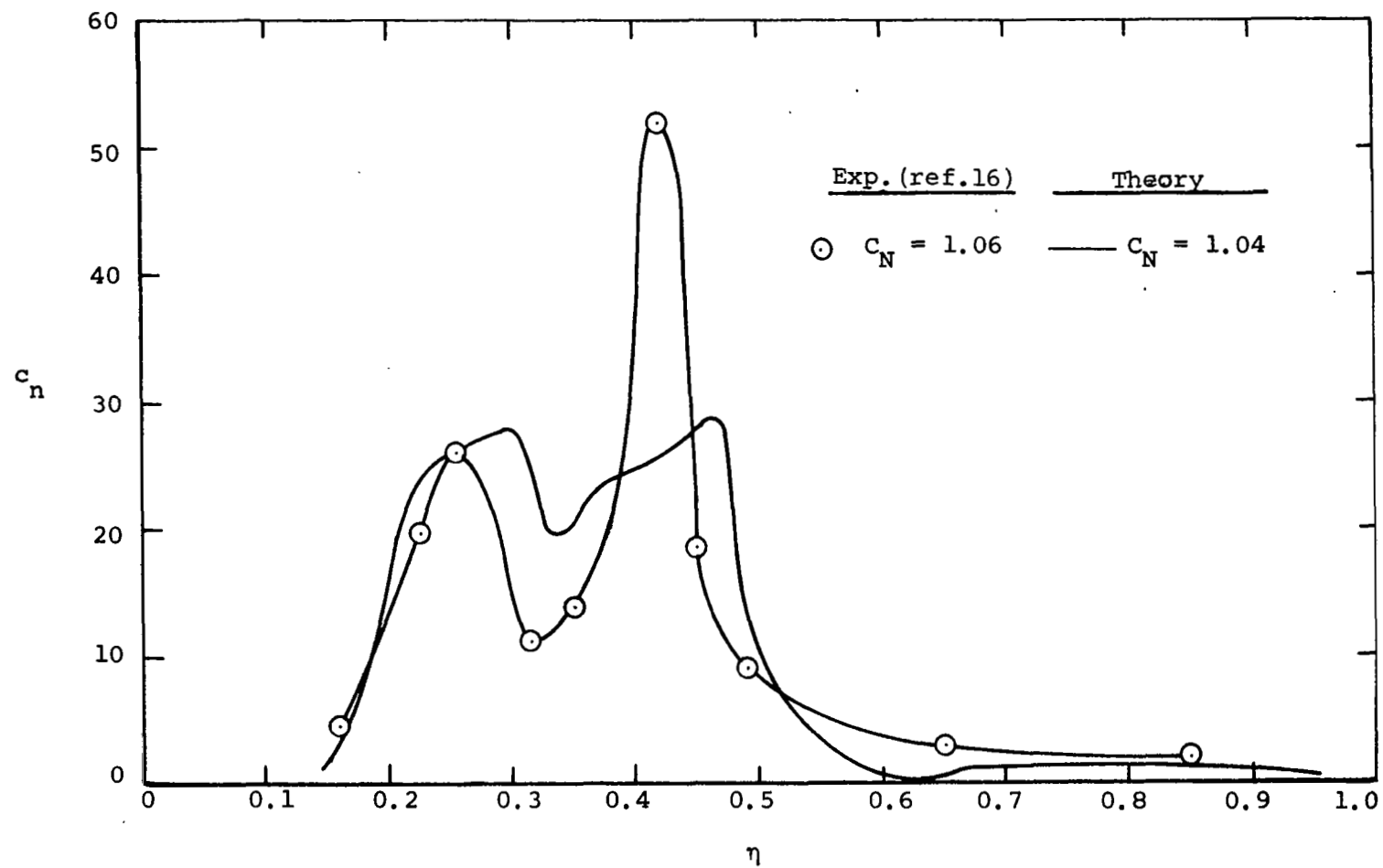
(d) Flap 3.

Figure 31.- Concluded.
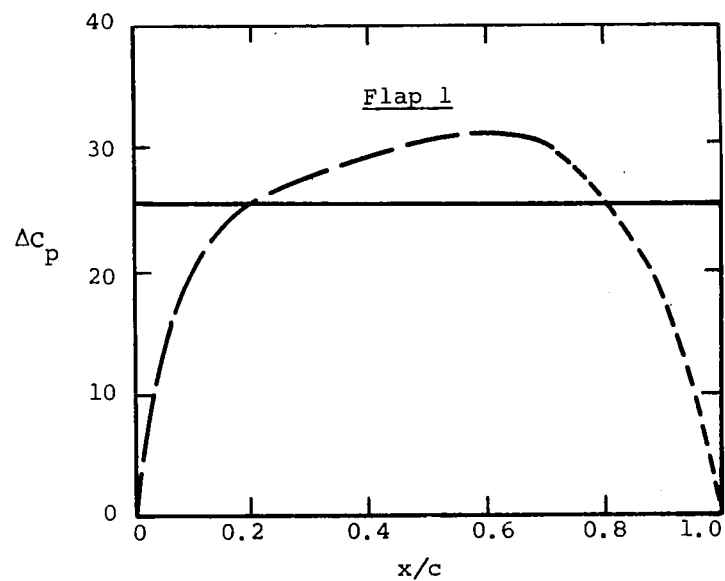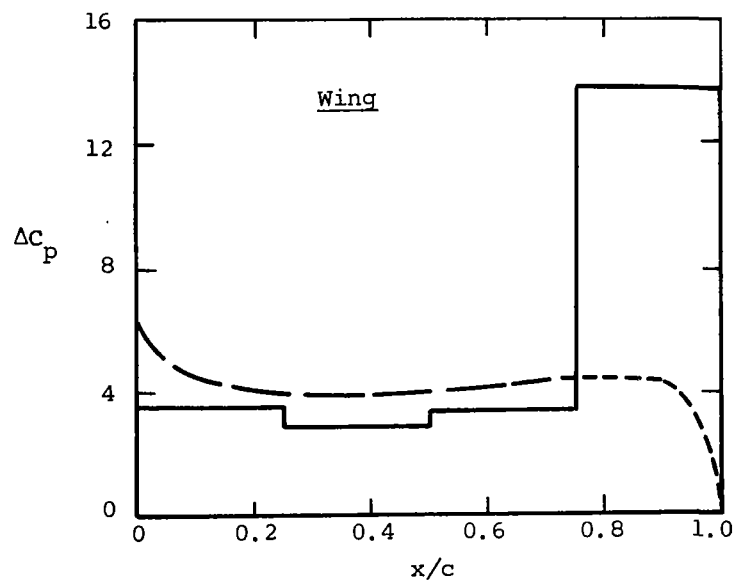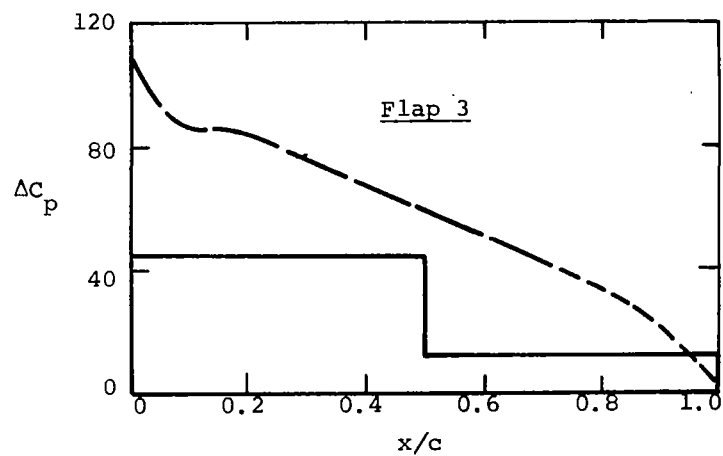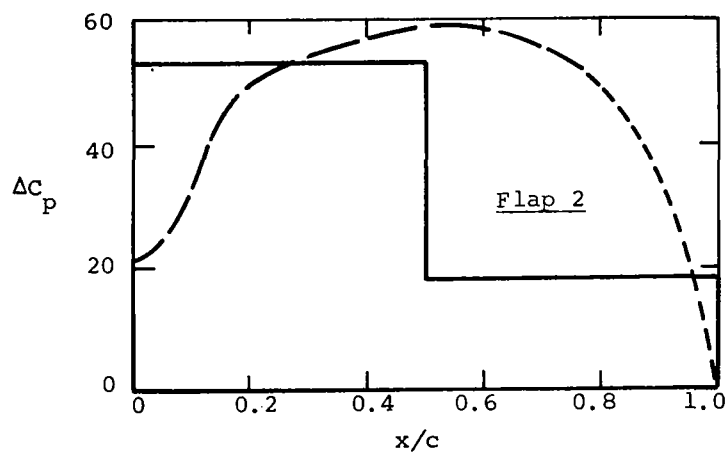
Figure 32.- Comparison of measured and predicted pressure coefficients on a four-engine EBF configuration at $\eta = 0.42$, $\delta_f = 15°/35°/55°/$, $C_\mu = 4.0°$, $\alpha = 6.5°$.

Exp.(ref.13)	C_μ	Theory
⊙	0.0	———————
▣	2.3	— — — —
◇	4.0	—— —— ——
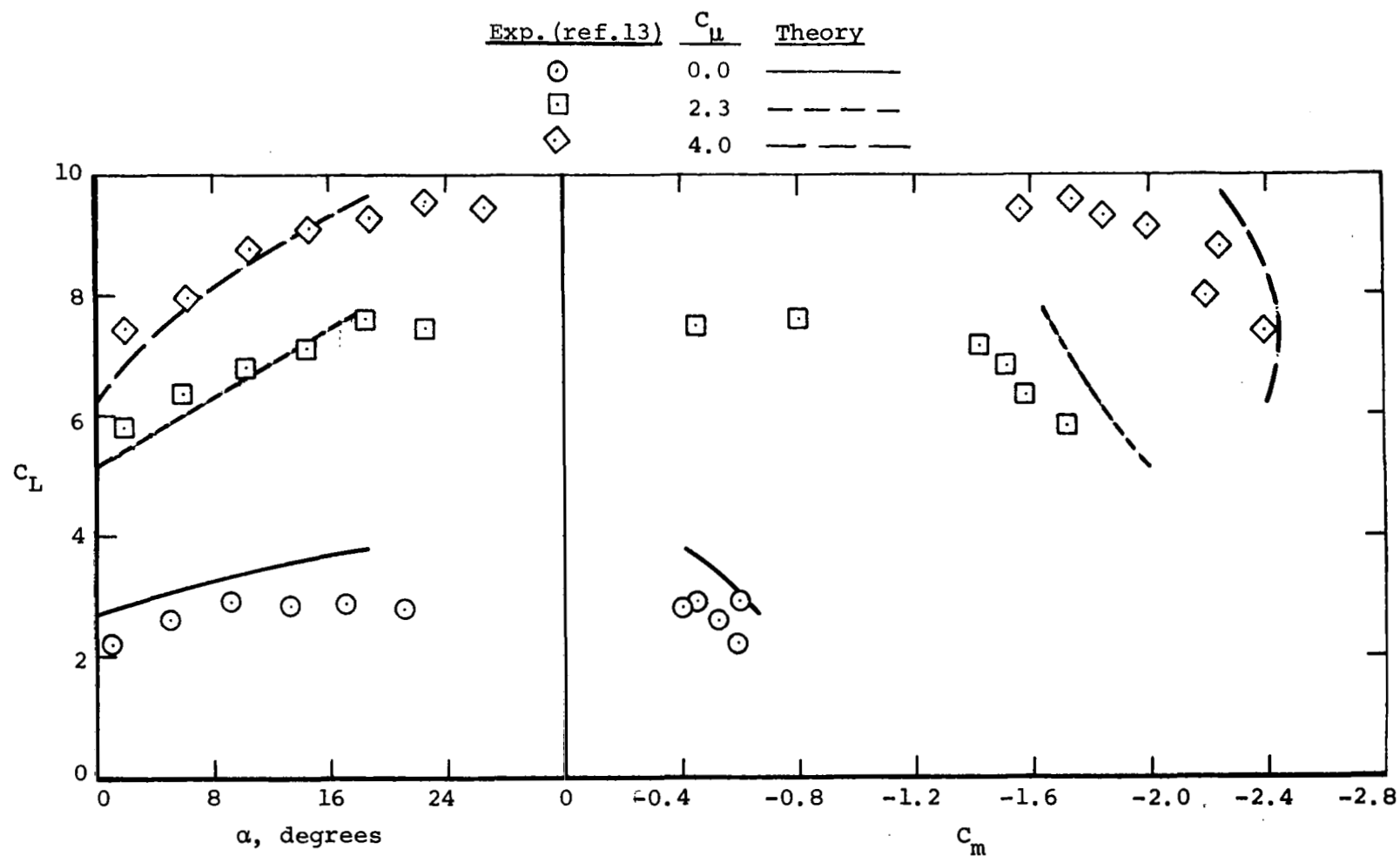
(a)   Lift and pitching moment coefficient.

Figure 33.- Measured and predicted longitudinal aerodynamic characteristics of a four-engine EBF configuration, $\delta_f = 15°/35°/55°$.
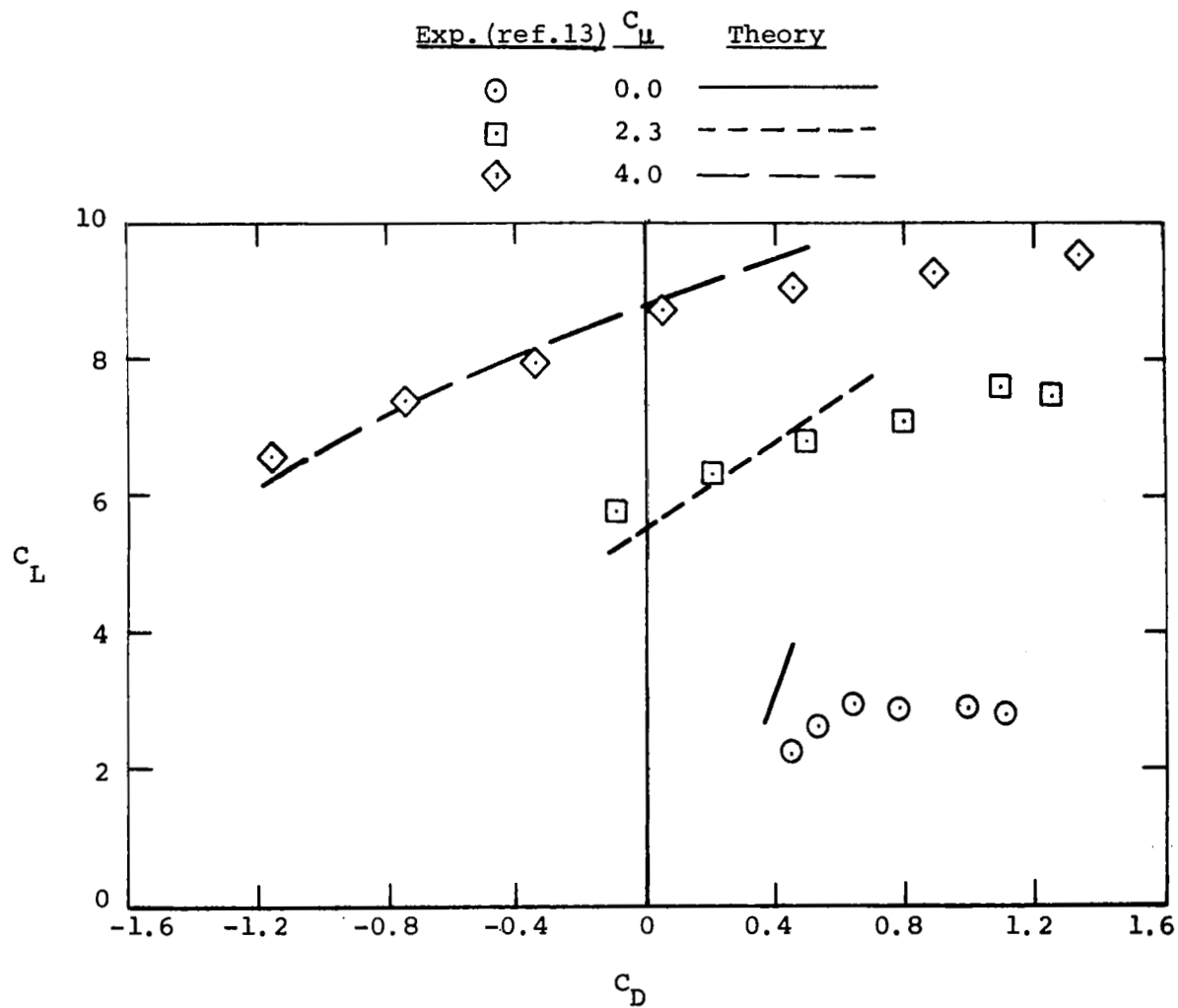
(b) Drag coefficient.

Figure 33.- Concluded.

(a) $\alpha = 6.5°$, $C_\mu = 4.0$
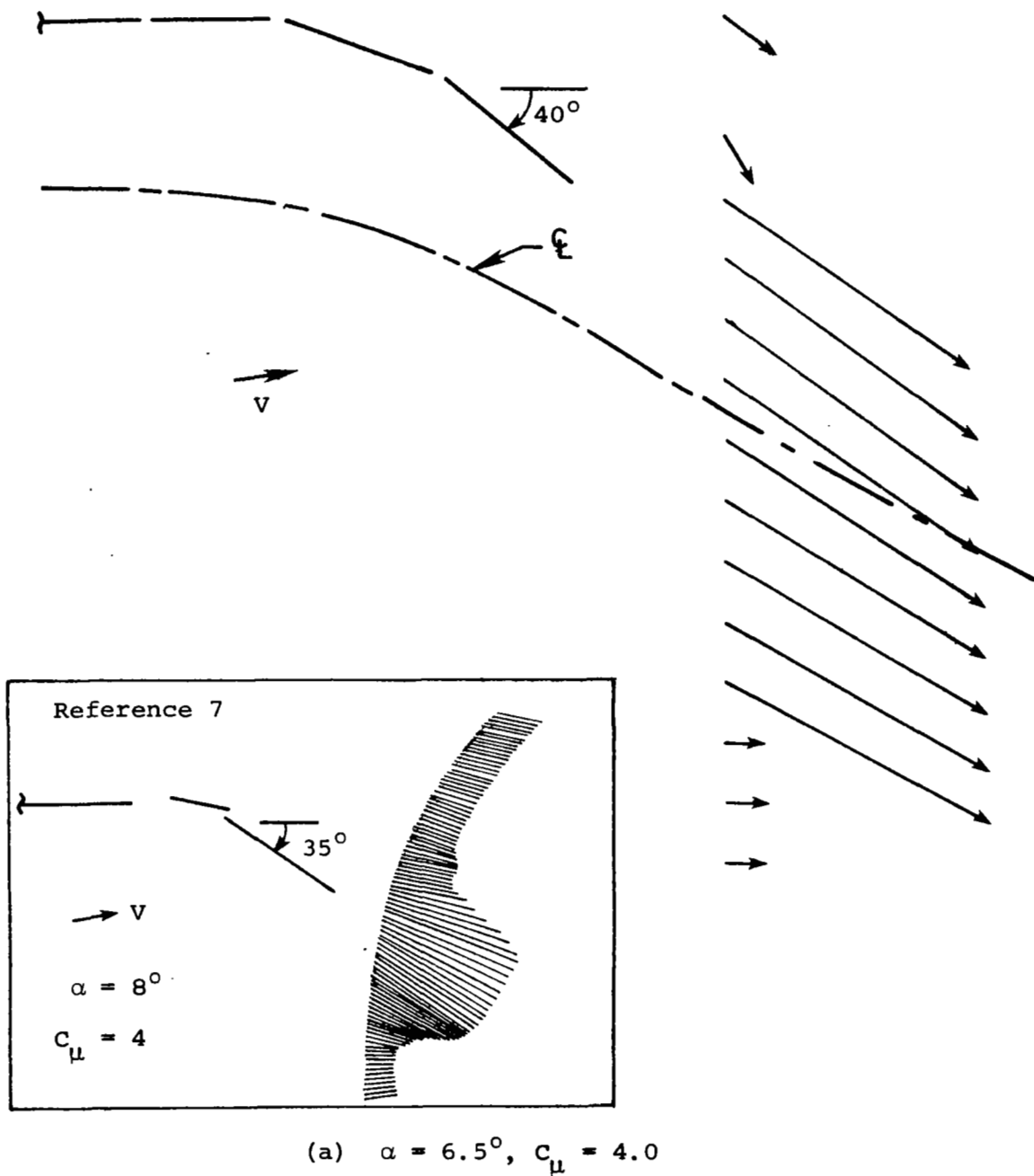
Figure 34.- Measured and predicted velocity profiles
aft of EBF configurations, $\eta = 0.25$.

Reference 7

$\alpha = 16^{\circ}$

$C_{\mu} = 2$
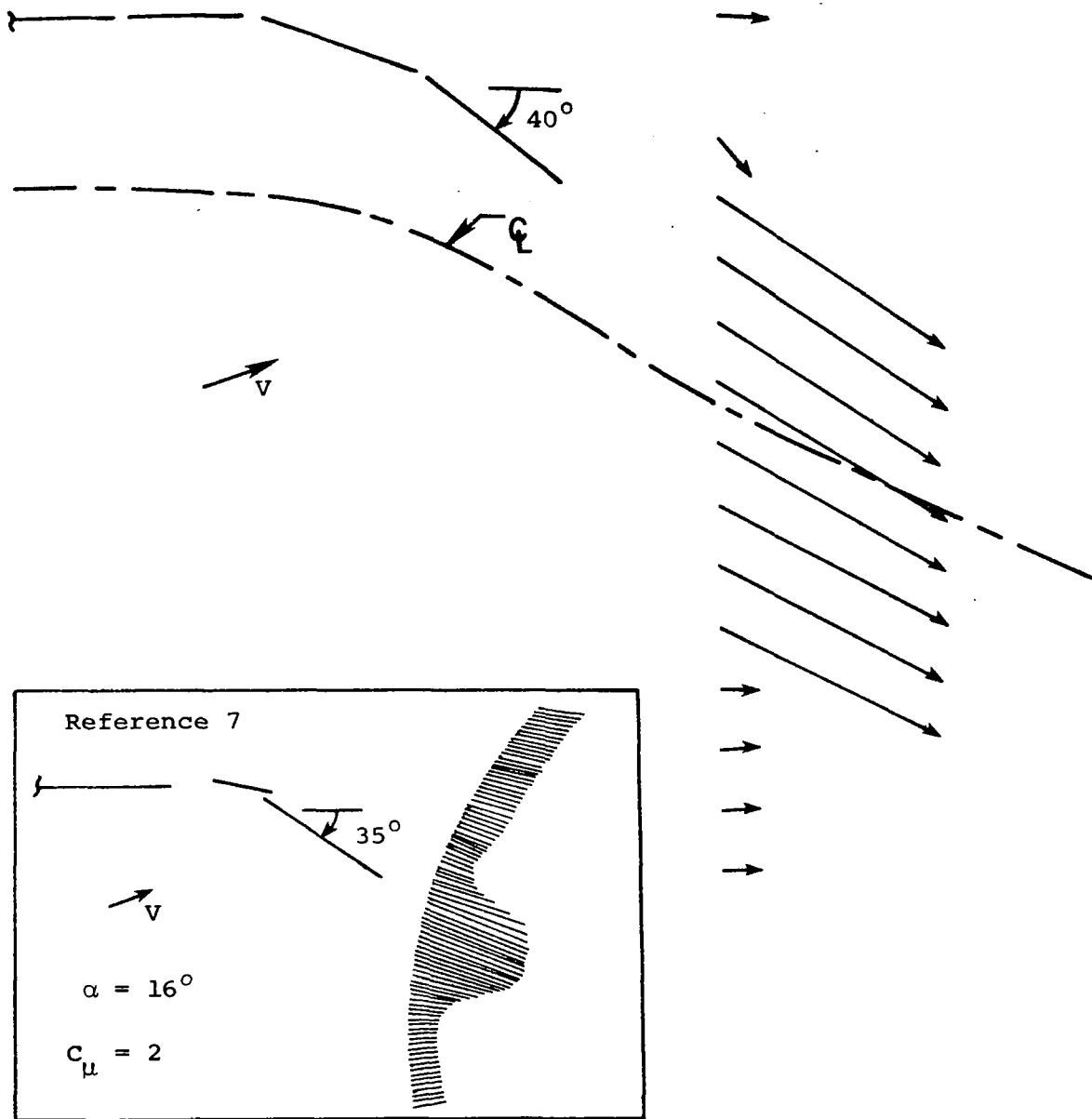
(b) $\alpha \approx 18.5^{\circ}$, $C_{\mu} \approx 2.3$

Figure 34.- Concluded.
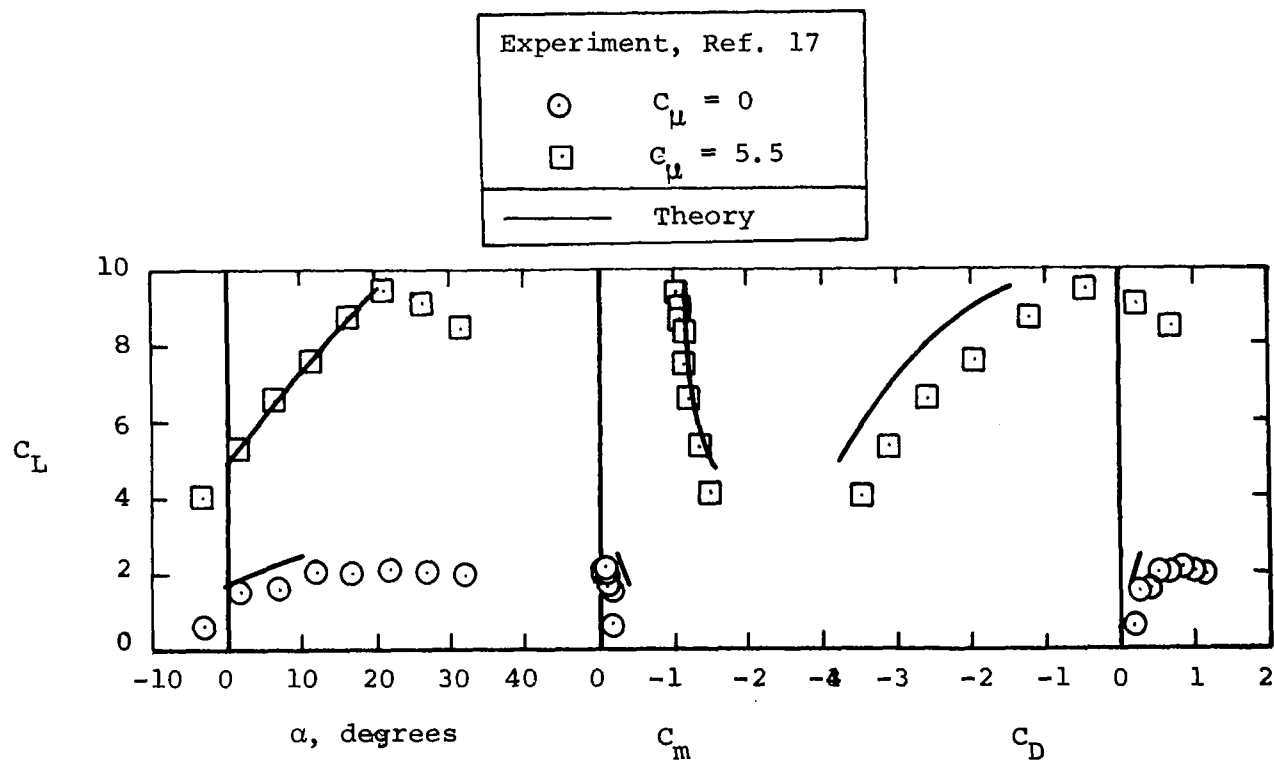
(a) $\delta_f = 17.5°/35°$.

Figure 35.- Measured and predicted longitudinal aerodynamic characteristics of a four-engine EBF configuration with an unswept wing and double-slotted trailing edge flaps.
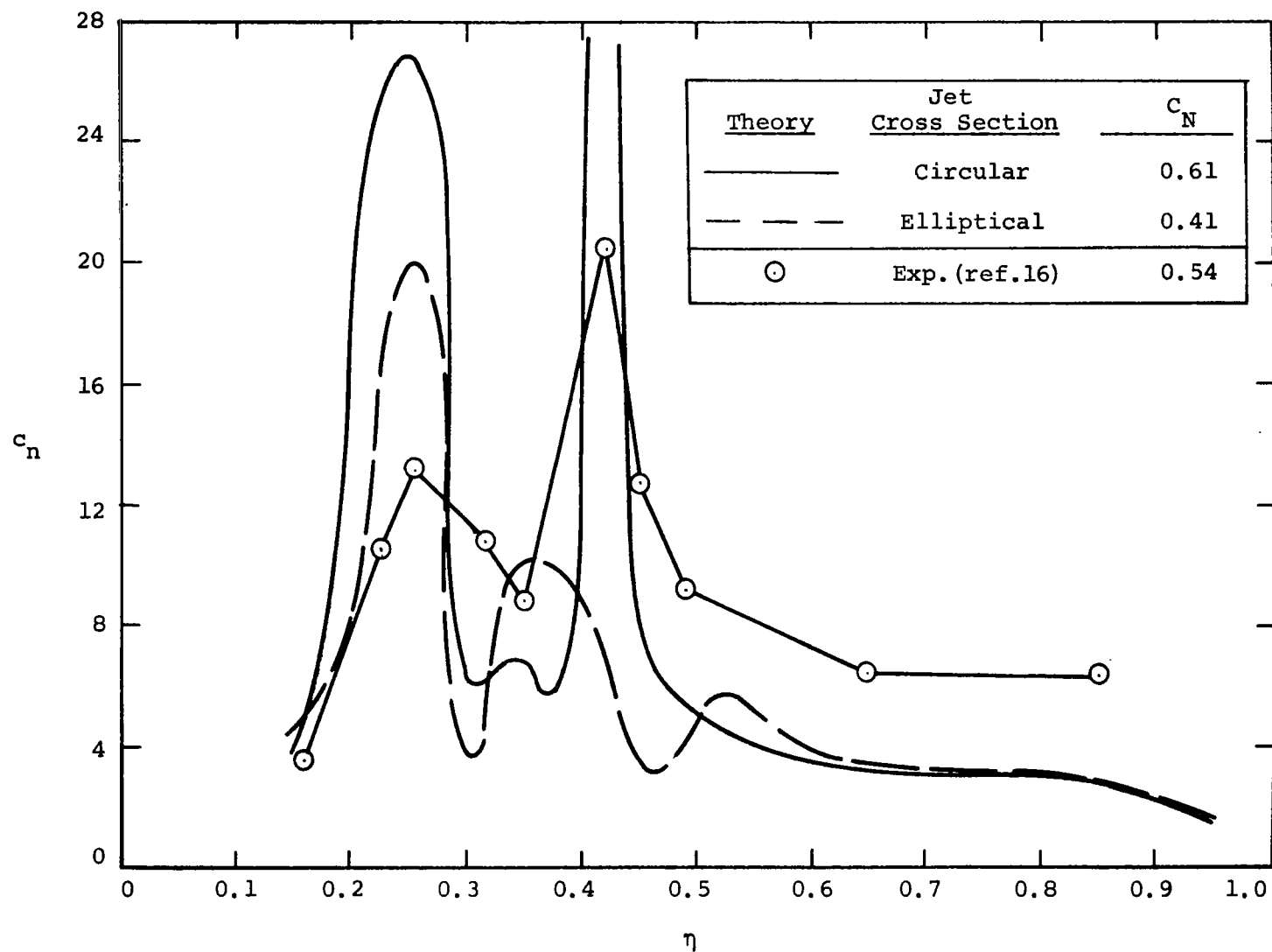
Experiment, Ref. 17

⊙ $C_\mu = 0$

☐ $C_\mu = 5.5$

——   Theory
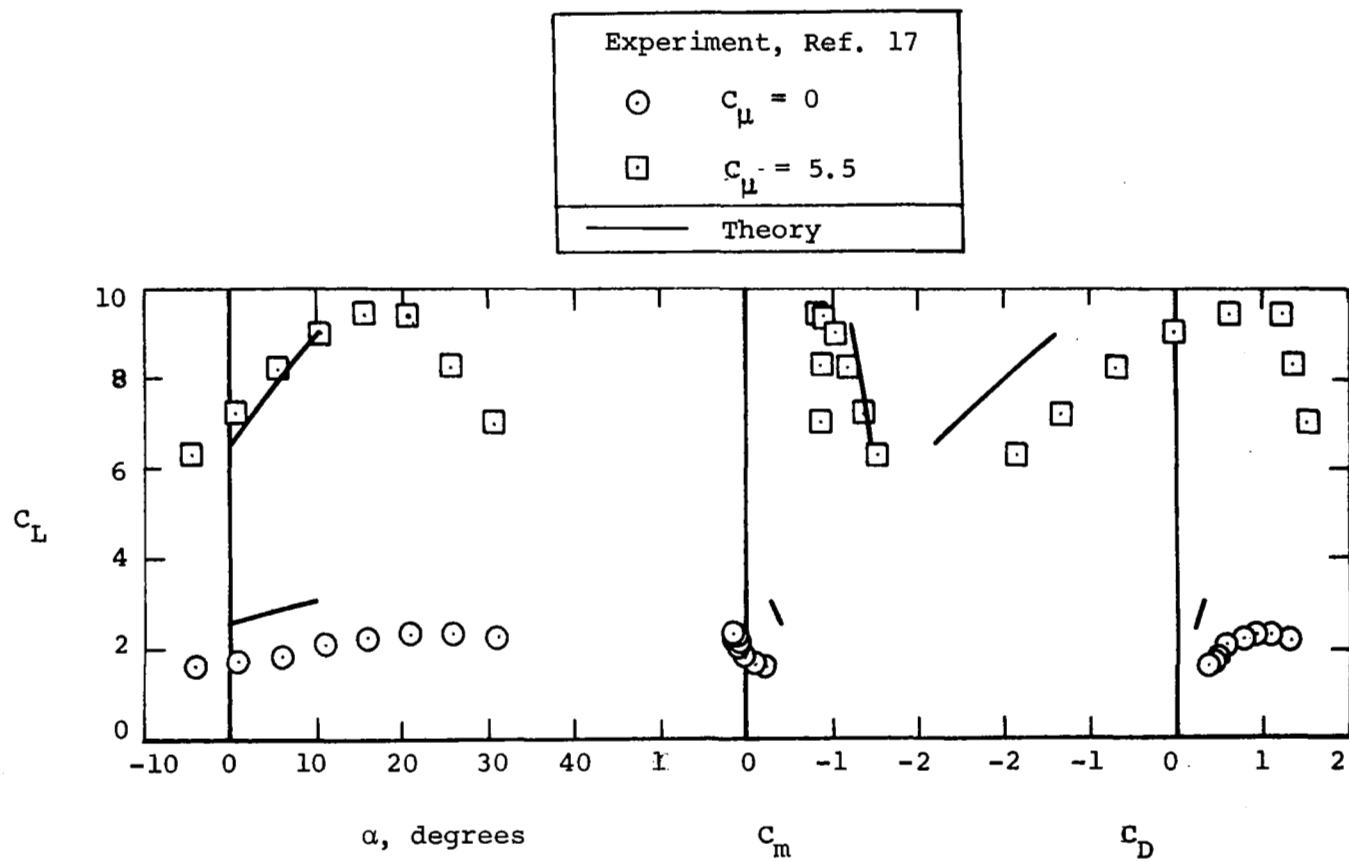
(b) $\delta_f = 27.5°/55°$.
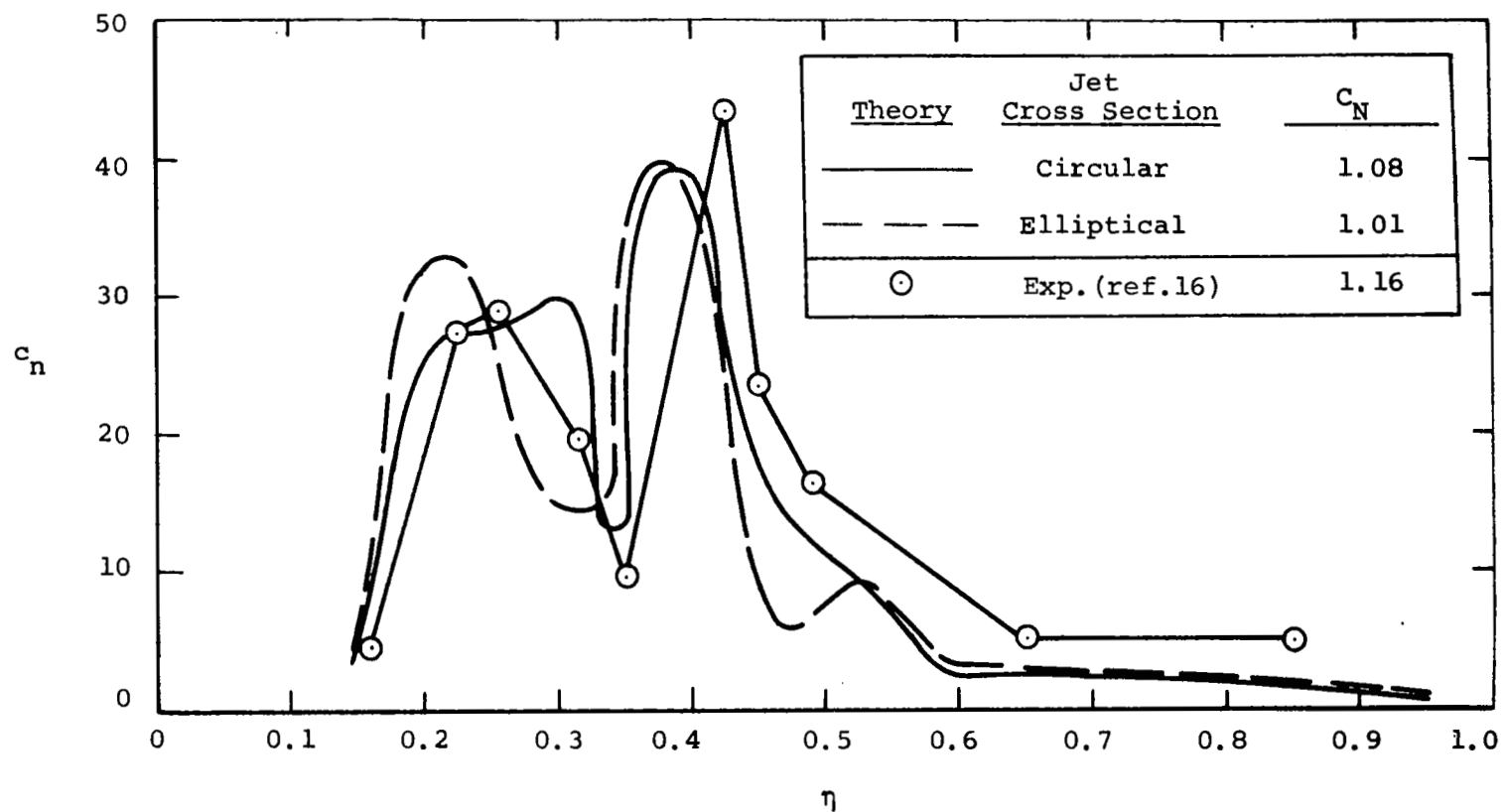
Figure 35.- Concluded.
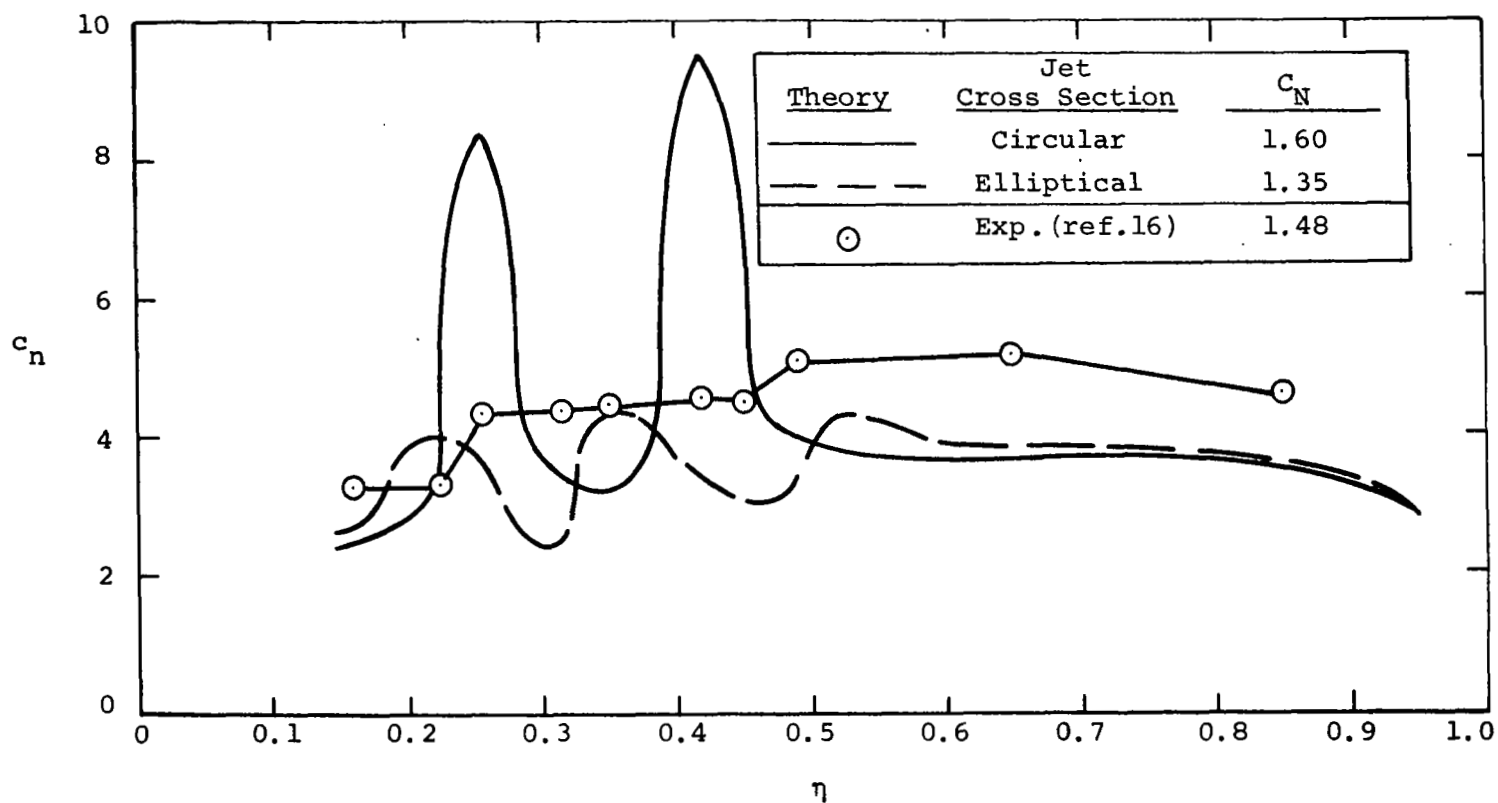
(a) Wing.

Figure 36.- Effect of jet cross section shape on predicted spanwise distribution
of section normal-force coefficients on the lifting surfaces of a four-engine
EBF configuration, $\delta_f = 15^\circ/35^\circ/55^\circ$, $C_\mu = 4.0$, $\alpha = 18.5^\circ$.
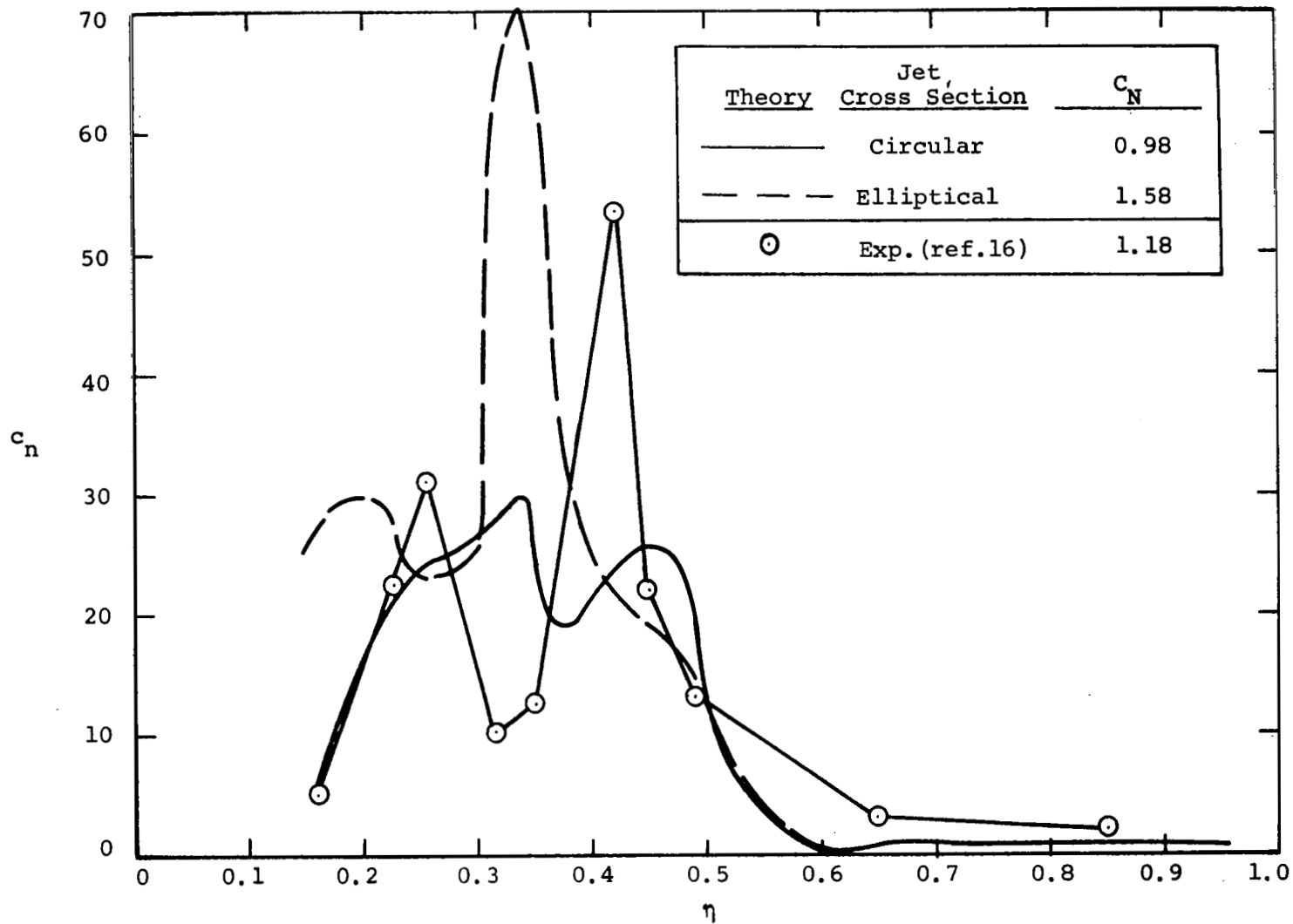
(b) Flap 1.

Figure 36.- Continued.

(c) Flap 2.

Figure 36.- Continued.

(d) Flap 3.

Figure 36.- Concluded.